DEPARTMENT OF TRANSPORTATION

Effect of Increased Precipitation (Heavy Rain Events) on Minnesota Pavement Foundations

Halil Ceylan, Principal Investigator
Institute for Transportation
Iowa State University

April 2024

Research Project
Final Report 2024-08

Technical Report Documentation Page

1. Report No. 2024-08	2.	3. Recipients Accession No.
4. Title and Subtitle Effect of Increased Precipitation (Heavy Rain Events) on Minnesota Pavement Foundations		5. Report Date April 2024 6.
7. Author(s) Md Jibon, Md Abdullah All Sourav, Masrur Mahedi, Sunghwan Kim, Halil Ceylan		8. Performing Organization Report No.
9. Performing Organization Name and Address Institute for Transportation Iowa State University 2711 S. Loop Drive, Suite 4700 Ames, IA 50010		10. Project/Task/Work Unit No. 11. Contract (C) or Grant (G) No. (c) 1036334 (wo) 7
12. Sponsoring Organization Name and Address Minnesota Department of Transportation Office of Research & Innovation 395 John Ireland Boulevard, MS 330 St. Paul, Minnesota 55155-1899		13. Type of Report and Period Covered Final Report 14. Sponsoring Agency Code
15. Supplementary Notes http://mdl.mndot.gov/		

16. Abstract (Limit: 250 words)

The Midwest region of the United States, including Minnesota, has been experiencing an increase in the number of heavy precipitation events. Historical precipitation data confirmed an increasing trend of heavy precipitation in Minnesota in the 21st century. This study focused on assessing the impact of heavy-precipitation events on moisture levels and stiffness of pavement foundation layers at the MnROAD facility. A two-step approach was adopted for predicting changes in saturation and for estimating corresponding resilient modulus values using the resilient modulus prediction equation employed in AASHTOWare Pavement Mechanistic-Empirical (ME) design. PLAXIS 3D, a finite element analysis tool, was used to simulate the movement of moisture within the pavement layer under varying heavy rainfall scenarios. Multiple linear regression models were developed from rainfall simulation data of the PLAXIS 3D model to predict base layer saturation based on rainfall characteristics and hydraulic conductivity of the material. ArcGIS Pro was then used to develop a framework to generate a preliminary vulnerability map showing changes in the resilient modulus of the pavement base layer from rain events. Four regression models were developed and used in ArcGIS Pro to predict changes in resilient modulus for distinct aggregate types under heavy rainfall events, revealing significant reductions in the base layer's resilient modulus. Recycled aggregate (a mix of recycled concrete aggregate and recycled asphalt pavement) emerged as more susceptible, with initial reductions in modulus values higher under heavy rainfall.

17. Document Analysis/Descriptors Climate change, Precipitation (Meteorology), Rainfall, Moisture content, Percent saturation, Finite element method, Permeability coefficient, Modulus of resilience, Geographic information systems		18. Availability Statement No restrictions. Document available from: National Technical Information Services, Alexandria, Virginia 22312	
19. Security Class (this report) Unclassified	20. Security Class (this page) Unclassified	21. No. of Pages 115	22. Price

Effect of Increased Precipitation (Heavy Rain Events) on Minnesota Pavement Foundations

Final Report

Prepared by:

Md Jibon
Md Abdullah All Sourav
Sunghwan Kim
Halil Ceylan
Department of Civil, Construction, and Environmental Engineering
Iowa State University

Masrur Mahedi
Soil Design Bureau,
Iowa Department of Transportation

April 2024

Published by:

Minnesota Department of Transportation
Office of Research & Innovation
395 John Ireland Boulevard, MS 330
St. Paul, Minnesota 55155-1899

This report represents the results of research conducted by the authors and does not necessarily represent the views or policies of the Minnesota Department of Transportation, Iowa Department of Transportation, or Iowa State University. This report does not contain a standard or specified technique.

The authors, the Minnesota Department of Transportation, Iowa Department of Transportation, and Iowa State University do not endorse products or manufacturers. Trade or manufacturers' names appear herein solely because they are considered essential to this report.

Acknowledgments

The authors gratefully acknowledge sponsorship for this project from the Minnesota Department of Transportation (MnDOT).

The project's Technical Advisory Panel (TAP) members Raul Velasquez (Office of Materials and Road Research), Barbara Fraley (Office of Research and Innovation), Leif Halverson (Office of Research and Innovation), Jeffrey Meek (formerly at Office of Sustainability and Public Health), Steven Henrichs (Office of Materials and Road Research), Benjamin Worel (Office of Materials and Road Research), Bernard Izevbekhai (Office of Materials and Road Research), Joseph Podolsky (Office of Materials and Road Research) are gratefully acknowledged for their guidance, support, and direction throughout the research.

The authors also thank the faculty and staff of Civil, Construction, and Environmental Engineering at Iowa State University (ISU). The authors would also like to acknowledge the invaluable support of colleagues and students in Iowa State University's Program for Sustainable Pavement Engineering and Research (PROSPER) at the Institute for Transportation (InTrans).

Table Of Contents

Chapter 1: Introduction 1

1.1 Research Methodology 1

1.2 Research Objectives 2

1.3 Organization of the Report 2

Chapter 2: MNROAD Instrumentation Data Analysis Related To Heavy Precipitation Events 3

2.1 Introduction 3

2.2 Historical Precipitation Data Analysis 3

2.3 Cell Selection And Moisture Data Analysis 10

2.3.1 Cell 16 11

2.3.2 Cell 18 14

2.3.3 Cell 20 and Cell 22 16

2.3.4 Cell 78 21

2.3.5 Cell 127 23

2.3.6 Cell 188 25

2.3.7 Cell 189 27

2.4 Summary 29

Chapter 3: Soil Thermal and Hydraulic Properties 31

3.1 Introduction 31

3.2 Available Material Properties 31

3.2.1 Cell 127, Cell 188, and Cell 189 32

3.2.2 Index Properties of Soil and Aggregates 34

3.2.3 Hydraulic Properties of Soil and Aggregates 36

3.2.4 Thermal Properties of Soil and Aggregates 41

3.3 Summary 44

Chapter 4: Plaxis 3D Hydraulic Modeling..45

4.1 Introduction...45

4.2 Cell 188 47

4.3 Cell 189 51

4.4 Cell 127 55

4.5 Summary...58

Chapter 5: Developing A Saturation Prediction Model And GIS Map of the MNROAD Facility 59

5.1 Introduction...59

5.2 Developing Saturation Prediction Model 59

5.2.1 Available Statewide Aggregate Information 59

5.2.2 Representative Pavement Models...60

5.2.3 Saturation of Pavement Base Layer 65

5.3 Developing A Vulnerability Map For MNROAD 71

5.3.1 User input..72

5.3.2 Saturation Calculation 73

5.3.3 Resilient Modulus Calculation..73

5.3.4 Shapefile Generation..74

5.4 Summary...75

Chapter 6: Recommendation For Asset Management Practices 77

Chapter 7: Summary and Conclusions...78

Chapter 8: Future Work and Recommendations..79

References...80

Appendix A: Analysis of Moisture Data

Appendix B: Python Script

List of Figures

Figure 1. Historical monthly total precipitation in Wright County for (a) January (b) February (c) March (d) April (e) May (f) June (g) July (h) August (i) September (j) October (k) November, and (l) December ... 6

Figure 2. MnROAD onsite weather stations monthly precipitation at MnROAD facility for the year of (a) 2009, (b) 2010, (c) 2011, (d) 2012, and (e) 2013 9

Figure 3. MnROAD onsite weather stations collected precipitation intensity data at the MnROAD facility for the year of (a) 2009, (b) 2010, (c) 2011, (d) 2012 and (e) 2013 10

Figure 4. Layer thickness and material information for the MnROAD Cell 16 (MnROAD-LTPP InfoPave system) 12

Figure 5. Volumetric moisture content trend of Cell 16 in 2009 for (a) RCA base, (b) Class 3 aggregate base, (c) SG subbase, and (d) clay subgrade layer along with (e) precipitation data 14

Figure 6. Layer thickness and material information for MnROAD Cell 18 (MnROAD-LTPP InfoPave system) 14

Figure 7. Volumetric moisture content trend of Cell 18 in 2009 for (a) RAP base, (b) Class 3 aggregate base, (c) SG subbase, and (d) clay subgrade layer along with (e) precipitation data 16

Figure 8. Layer thickness and material information for MnROAD Cell 20 (MnROAD-LTPP InfoPave system) 17

Figure 9. Layer thickness and material information for MnROAD Cell 22 (MnROAD-LTPP InfoPave system) 18

Figure 10. Volumetric moisture content trend of Cell 20 in 2009 for (a) Class 5 aggregate base, (b) Class 3 aggregate base, (c) SG subbase, and (d) clay subgrade layer along with (e) precipitation data 19

Figure 11. Volumetric moisture content trend of Cell 22 in 2009 for (a) Class 5 aggregate base, (b) Class 3 aggregate base, (c) SG subbase, and (d) clay subgrade layer along with (e) precipitation data 20

Figure 12. Layer thickness and material information for MnROAD low volume road Cell 78 (MnROAD-LTPP InfoPave system) 21

Figure 13. Volumetric moisture content trend of Cell 78 in 2009 for (a) Class 6 aggregate base along with (b) precipitation data 23

Figure 14. Layer thickness and material information for MnROAD low volume road Cell 127 (MnROAD-LTPP InfoPave system) 24

Figure 15. Volumetric moisture content trend of Cell 127 in 2020 for Class 6 aggregate base along with precipitation data (collected from Technical Advisory Panel [TAP] member)........ 25

Figure 16. Layer thickness and material information for MnROAD low volume road Cell 188 (MnROAD-LTPP InfoPave system) 26

Figure 17. Volumetric moisture content trend of Cell 188 in 2020 for Class 6 limestone along with precipitation data (collected from TAP member) 27

Figure 18. Layer thickness and material information for MnROAD low volume road Cell 189 (MnROAD-LTPP InfoPave system) 28

Figure 19. Volumetric moisture content trend of Cell 189 in 2020 for Recycled aggregate base along with precipitation data (collected from TAP member) 29

Figure 20. Plan view and layered structure of Cell 127, including the location of the thermocouple and moisture probe (Cetin et al. 2021) 32

Figure 21. Plan view and layered structure of Cell 188, including the location of the thermocouple and moisture probe (Cetin et al. 2021) 33

Figure 22. Plan view and layered structure of Cell 189, including the location of the thermocouple and moisture probe (Cetin et al. 2021) 33

Figure 23. Illustration of typical soil water characteristics with drying, wetting curve and hysteretic behavior of soil (Likos et al. 2013) 37

Figure 24. Soil water characteristics curve for Class 6 aggregate at optimum compaction condition by hanging column test (Cetin et al. 2021) 38

Figure 25. Soil water characteristics curve for limestone at optimum compaction condition by activity meter and pressure plate tests (Cetin et al. 2021) 38

Figure 26. Soil water characteristics curve for RCA + RAP at optimum compaction condition by activity meter and pressure plate tests (Cetin et al. 2021) 39

Figure 27. Soil water characteristics curve for clay loam at optimum compaction condition by activity meter and pressure plate tests (Cetin et al. 2021) 39

Figure 28. Thermal diffusivity of limestone in Cell188 estimated by phase equation (Cetin et al. 2021) 43

Figure 29. Thermal diffusivity of RCA + RAP in Cell189 estimated by phase equation (Cetin et al. 2021) 43

Figure 30. Thermal diffusivity of LSSB in Cell127 estimated by phase equation (Cetin et al. 2021) 44

Figure 31. PLAXIS 3D model with the dimensions of each layer for the Cell 188 structure 47

Figure 32. Saturation of limestone aggregate (a) rainfall at MnROAD facility (b) time dependent rainfall scenario in PLAXIS 3D (c) PLAXIS 3D simulation after 31 days (d) variation of saturation from PLAXIS 3D (e) rainfall and saturation data from field sensors 51

Figure 33. PLAXIS 3D model with the dimension of each layer for the Cell 189 structure........................52

Figure 34. Saturation of RCA + RAP aggregate (a) PLAXIS 3D simulation after 31 days (b) variation of saturation from PLAXIS 3D (a) rainfall and saturation data from field sensors..54

Figure 35. PLAXIS 3D model for the Cell 127 structure with dimensions of each layer 55

Figure 36. Saturation of Class 6 aggregate (a) PLAXIS 3D simulation after 31 days (b) variation of saturation from PLAXIS 3D (a) rainfall and saturation data from field sensors..58

Figure 37. A representative PLAXIS 3D model with the dimensions of each layer for MN Class 5, Bryan Redrock Class 5, and Bryan Redrock Ball Diamond aggregates..61

Figure 38. A representative PLAXIS 3D model with the dimensions of each layer for MN Class 5Q aggregates..62

Figure 39. Variation of saturation in (a) pavement structure of Cell 188, (b) middle of limestone aggregate base layer of Cell 188, (c) RCA + RAP aggregate layer of Cell 189, and (d) Class 6 aggregate layer of Cell 127 due to rainfall intensity ranging from 1 in/hr to 6 in/hr and duration of 4 hrs 67

Figure 40. Equality plot between predicted saturation and simulated saturation from PLAXIS 3D 68

Figure 41. Variation of resilient modulus of limestone aggregate with heavy rainfall..............................69

Figure 42. Variation of resilient modulus of Class 6 aggregate with heavy rainfall..................................70

Figure 43. Variation of resilient modulus of Class 6 aggregate with heavy rainfall..................................71

Figure 44. Flowchart for pavement foundation vulnerability assessment 72

Figure 45. ArcGIS generated a vulnerability map for MnROAD low volume road...................................75

List of Tables

Table 1. Calibration coefficients for Decagon 5TE moisture sensor and Proctor parameters 11

Table 2. Arrangement of moisture sensors in Cell 16 and their locations in pavement layers 12

Table 3. Arrangement of moisture sensors in Cell 18 and their locations in pavement layers 15

Table 4. Arrangement of moisture sensors in Cell 20 and their locations in pavement layers 17

Table 5. Arrangement of moisture sensors in Cell 22 and their locations in pavement layers 18

Table 6. Arrangement of moisture sensors in Cell 78 and their locations in pavement layers 22

Table 7. Arrangement of moisture sensors in Cell 127 and their locations in pavement layers (Cetin et al., 2021) 24

Table 8. Arrangement of moisture sensors in Cell 188 and their locations in pavement layers (Cetin et al., 2021) 26

Table 9. Arrangement of moisture sensors in Cell 189 and their locations in pavement layers (Cetin et al., 2021) 28

Table 10. List of index properties and soil classification (Cetin et al. 2021) 34

Table 11. Results of proctor compaction and specific gravity of materials (Cetin et al. 2021) 35

Table 12. Asphalt binder and residual cement mortar content of materials (Cetin et al. 2021) 36

Table 13. Saturated volumetric water content, pressures at the air-entry level, and van Genuchten Model Parameters (Cetin et al. 2021).. 40

Table 14. Saturated hydraulic conductivity of materials by both constant head and falling head permeability tests (Cetin et al. 2021).. 41

Table 15. List of material properties for Cell 188 (Cetin et al. 2021 and Pease 2010) 48

Table 16. List of material properties for Cell 189 (Cetin et al. 2021 and Pease 2010) 53

Table 17. List of material properties for Cell 127 (Cetin et al. 2021 and Pease 2010)................. 56

Table 18. List of base aggregates and their classification (Cetin et al. 2021 and Oh et al. 2021) 60

Table 19. Lists of materials and their representative Cells for PLAXIS 3D models 61

Table 20. List of material properties for representative pavement model (Cetin et al. 2021 and Pease 2010) 63

Table 21. List of material properties for Cell 328 (Cetin et al. 2021 and Pease 2010) 64

Table 22. Sample input values for the vulnerability map 73

Table 23. Calculated MR and saturation values based on the example input values and extracted rainfall information 74

List of Abreviations

AASHTO	American Association of State Highway and Transportation Officials
FHWA	Federal Highway Administration
LVR	Low Volume Road
MnDOT	Minnesota Department of Transportation
MnROAD	Minnesota Road Test Facility
M_R	Resilient Modulus
GIS	Geographic Information System
RWIS	Minnesota Road Weather Information System
RCA	Recycled Concrete Aggregate
RAP	Recycled Asphalt Pavement
SWCC	Soil Water Characteristics Curve
FWD	Falling Weight Deflectometer
COOP	Cooperative Observer Network
DNR	Department of Natural Resources
MEPDG	Mechanistic Empirical Pavement Design Guide
NRRA	National Road Research Alliance
MDD	Maximum Dry Density
OMC	Optimum Moisture Content
SG	Select Granular
LSSB	Large Stone Subbase
SSD	Saturated Surface Dry
OD	Oven Dry
HC	Hydraulic Conductivity
LTPP	Long-term Pavement Performance

Executive Summary

Climate change-induced shifts in precipitation patterns, particularly the intensification of heavy rainfall events, pose significant challenges to the Midwest region of the United States. The Minnesota Department of Transportation (MnDOT) initiated a research study to recognize the potential implications of increased precipitation on infrastructure, especially pavement foundations. This study investigated the impact of heavy precipitation on the resilience of Minnesota's pavement foundations, focusing on the MnROAD facility. In the first step, historical weather data and moisture sensor data of the MnROAD facility were analyzed. The analysis confirmed an increasing precipitation trend during the months of heavy precipitation, June to August, in Minnesota in the 21st century. Five selected pavement test sections in MnROAD were examined to seek a better understanding of the relationship between heavy rainfall and changes in moisture levels within pavement foundation layers. Test cells exhibited no consistent trend in volumetric content, and there was a sudden, significant change in moisture levels that could not be solely attributed to the precipitation trend of the same year. After examining the pavement temperature at the specific cell locations, it was deduced that the early peak volumetric moisture content was linked to thawing events in those locations.

A comprehensive literature review was conducted to find the material properties of test cells located in the MnROAD facility. Material properties such as saturated hydraulic conductivity and soil-water characteristic curves for Class 6 aggregate, limestone aggregate, recycled aggregates (Recycled Concrete Aggregate [RCA]+ Recycled Asphalt Pavement [RAP]), and clay loam were used for modeling and moisture flux simulation in pavement foundations. PLAXIS 3D, a geotechnical finite element analysis tool, was used to generate three-dimensional pavement models and simulate moisture fluxes in pavement systems by using the material properties.

Calibration and validation of these models were performed by using saturation data collected from field sensors installed at the MnROAD facility. The validation process employed field sensor-collected saturation values, emphasizing rainfall sensitivity to pavement materials. Rainfall scenarios with varying intensities and durations were simulated in the PLAXIS 3D model after calibration. A multiple linear regression model was developed to predict saturation in the middle of a base layer based on rainfall parameters. The reduced stiffness of the pavement foundation was quantified by reduction of the resilient modulus (M_R) of the corresponding layers. The M_R is a key parameter used to characterize elastic behavior of unbound materials, including soil and aggregates. The Pavement ME design guidelines, developed by the American Association of State Highway and Transportation Officials (AASHTO), use the M_R to model and predict the behavior of pavement materials and structures in response to various environmental and loading conditions. Regression models for base layer stiffness were developed after incorporating those saturation values into the Mechanistic Empirical Pavement Design Guide (MEPDG) equation, and prediction models provided the M_R of base-layer values by incorporating hydraulic conductivity, rainfall intensity, and duration parameters of base aggregates.

A preliminary pavement foundation vulnerability map was generated using ArcGIS Pro and developed prediction models. A script was developed to take weather data and load as input to calculate saturation and M_R value. It also automatically generated a GIS map showing the location of pavement and their resilient modulus. The GIS map can show changes in pavement foundation M_R due to moisture variations caused by heavy precipitation, offering insight into moisture dynamics. The current study showed the vulnerability map for only the selected site at the MnROAD facility, but there is a potential to expand the study scope to accommodate the state of Minnesota. This study provided a comprehensive understanding of the impact of heavy precipitation on pavement foundations. Through meticulous data analysis, advanced modeling techniques, and GIS-based visualization, the research contributed valuable insight for infrastructure planning and maintenance.

Chapter 1: Introduction

Managing and maintaining transportation infrastructure, especially road pavements, in the face of dynamic climate conditions has been and will continue to be a significant challenge. Heavy rainfall exacerbated by climate change poses a substantial threat to pavement foundations in Minnesota. To address the effect of heavy rainfall, this study employs mechanistic-based regression models, advanced Geographic Information Systems (GIS) technology, and automated data processing to predict and map the stiffness of pavement base layers. The Midwest region of the United States has been experiencing more frequent heavy precipitation over the last several decades because of the adverse impact of climate change. According to the U.S. Global Change Research Program (2021), in Minnesota, the heaviest 1% of precipitation events increased 42% between 1986 and 2016, and such precipitation changes could significantly impact subsurface flow conditions and moisture content of pavement foundations. Intense rainfall resulting in higher moisture in pavement foundations could adversely impact a foundation layer's stiffness, strength, and durability.

The resilient modulus (M_R) is a key parameter used to characterize the elastic behavior of unbound materials that include soil and aggregates. M_R is defined as the ratio of peak deviatoric stress to the recoverable strain (strain that is reversed when the load is removed) in a material subjected to cyclic or repeated loading (Mishra et al. 2019). The Pavement ME design guidelines, developed by the American Association of State Highway and Transportation Officials (AASHTO), use the M_R to model and predict the behavior of pavement materials and structures in response to various environmental and loading conditions (Jibon and Mishra 2021). This study focuses on changes in resilient modulus values due to heavy rainfall-induced moisture fluxes in pavement foundation layers.

1.1 Research Methodology

To help achieve the goals of this study, a comprehensive literature review was conducted to collect historical precipitation data for the region, emphasizing trends in heavy precipitation during the 21st century. Historical precipitation trends in the region were analyzed, confirming increasing precipitation trends in the 21st century during periods of heavy precipitation. This study employed a comprehensive methodology to investigate the impact of heavy precipitation on pavement foundation layers at the MnROAD facility in Minnesota. The study's design centers on specific objectives focused on understanding the relationship between heavy precipitation events and the moisture levels in pavement foundation layers. To achieve this, a meticulous selection process was undertaken, resulting in identification of particular test cells from the MnROAD low-volume road. Data collection involved obtaining moisture data, material properties and historical weather station data. Challenges with missing data records and sensor limitations were addressed, with a particular focus on selected cells with high-quality moisture data. The finite-element method was adopted for developing a hydraulic model, incorporating assumed material properties and subsequent calibration and validation using long-term performance data. PLAXIS 3D modeling simulated moisture flux due to heavy rainfall, validated by comparison with field instrumentation data. The study also developed a vulnerability map by using Esri's GIS software ArcGIS Pro and Python programming language with its data manipulation library Pandas and GeoPandas to perform automation and scripting. The developed automation program took weather information from the test sites and user inputs of some fixed parameters to generate an output GIS map that showed the M_R of the pavement foundation soil resulting from moisture variation caused by heavy rainfall.

1.2 Research Objectives

These research objectives were chosen to contribute valuable insights into the effects of heavy precipitation on pavement foundation layers, ultimately enhancing the resilience and sustainability of Minnesota's road infrastructure. The objectives of this study were to:

(i) Examine historical precipitation events in the Minnesota region, with a focus on heavy precipitation trends during the 21st century
(ii) Analyze the correlation between these precipitation trends and the moisture levels in pavement foundation layers at the MnROAD facility
(iii) Create a robust finite-element model using PLAXIS 3D to simulate moisture flux in pavement foundation layers due to heavy rainfall
(iv) Predict changes in saturation level at base layer and associated stiffness reduction due to heavy rainfall
(v) Develop a GIS-based framework to generate a vulnerability map for pavement foundation by integrating the developed foundation susceptibility prediction models

1.3 Organization of the Report

This report includes eight chapters. Chapter 1 describes the background, objectives, and research methodology of this study. Chapter 2 provides a comprehensive analysis of MnROAD instrumentation data analysis of heavy precipitation events. Chapter 3 discusses the available soil and aggregate thermal and hydraulic properties, detailing the selected cells of the MnROAD facility used in the later part of this research for rainfall simulation. The process of using the selected cells for simulation and model development are discussed in Chapter 4. Chapter 5 provides the comprehensive description of modeling and GIS map generation, followed by recommendations for asset management practices in Chapter 6, summary and conclusions in Chapter 7, and future work and recommendations in Chapter 8.

Chapter 2: MNROAD Instrumentation Data Analysis Related To Heavy Precipitation Events

2.1 Introduction

The MnROAD facility has an onsite weather station for recording and monitoring weather conditions, including precipitation, temperature, wind, and radiation data, and northwestern weather stations at Minnesota Road Weather Information System (RWIS) sites have been recording weather data since March 21, 1997; the Southeast weather station has also been operating since April 30, 1998 (MnDOT, 2014). The MnROAD facility has more than 50 test cells equipped with various types of sensors embedded in different pavement layers. For example, thermocouple and moisture sensors were installed to study environmental effects on pavement foundation layers, hosting moisture sensors in base, subbase, and subgrade layers for monitoring moisture changes in those layers. This study focuses on test cells associated with conventional aggregate bases: Class 3 and Class 5 aggregate and recycled aggregate bases [e.g., recycled concrete aggregate (RCA) and Recycled asphalt pavement (RAP)]. For collecting weather data, the MnROAD facility also routinely performs falling-weight deflectometer (FWD) tests to track pavement performance changes over time. FWD tests apply dynamic plate loads to a pavement surface to measure its structural response corresponding to dynamic loading. A FWD device also locates multiple geophones at different offsets from the loading plate to capture a deflection basin that could be utilized to estimate the back-calculated layer moduli of the pavement layers. FWD data of the different seasons over a year could be utilized to capture the impact of heavy precipitation-related moisture on a pavement foundation system. This chapter includes evaluation of historical data from the MnROAD facility, seeking to find potential precipitation changes due to the impact of climate change.

2.2 Historical Precipitation Data Analysis

This section describes precipitation trends in Wright County in Minnesota where the MnROAD facility is located. Decadal monthly total precipitation trends from the Cooperative Observer Network (COOP) in Wright County, Minnesota, were determined using a Minnesota Department of Natural Resources (DNR) climate trend tool that could generally calculate climate trends across different spatial regions and climate divisions throughout Minnesota (https://arcgis.dnr.state.mn.us/ewr/climatetrends/). Climate data available through the DNR climate tool include average temperature, maximum temperature, minimum temperature, precipitation, and drought severity index. **Figure 1** shows the decadal monthly precipitation trend in Wright County, MN, in terms of mean monthly precipitation for the 20th and 21st centuries. The mean monthly precipitation for February, March, April, May, June, August, September, October, and December increased over the last twenty years compared to the entire 20th century, although there was a slight decrease to no change in precipitation observed for November and July over the last twenty years. **Figure 1** shows the significant precipitation increment trend for the current 21st century.

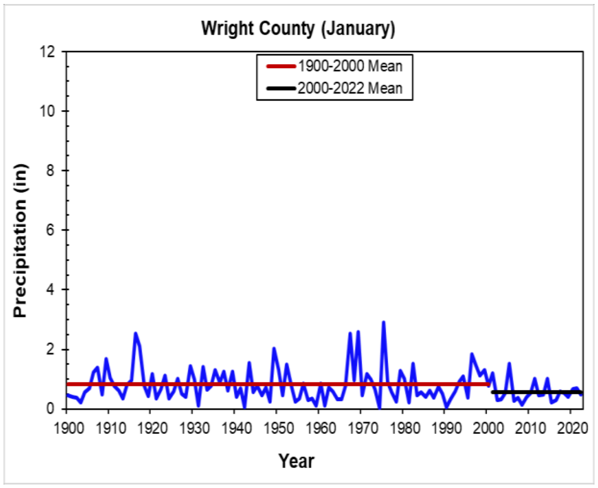

(a)

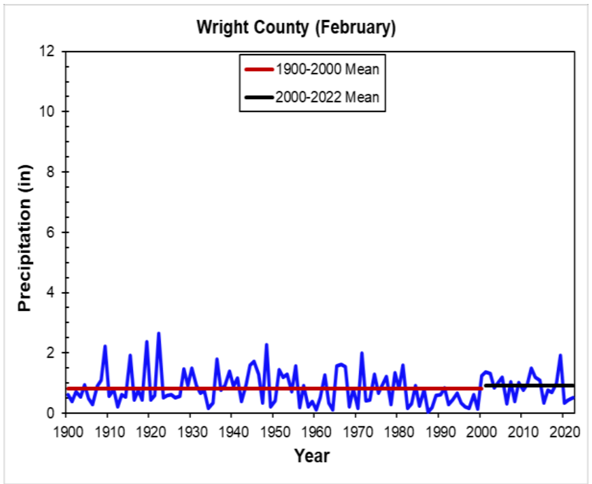

(b)

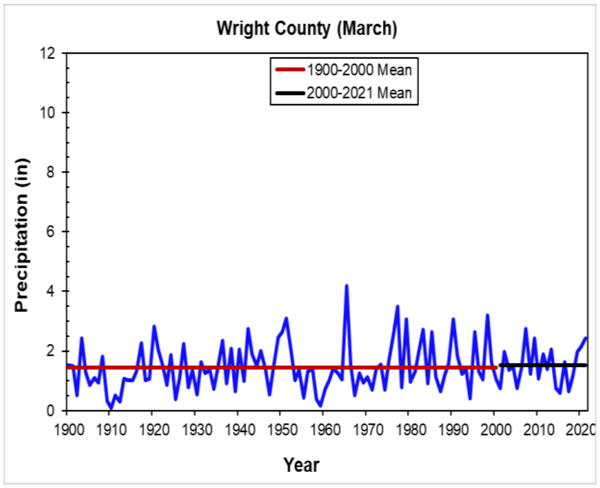

(c)

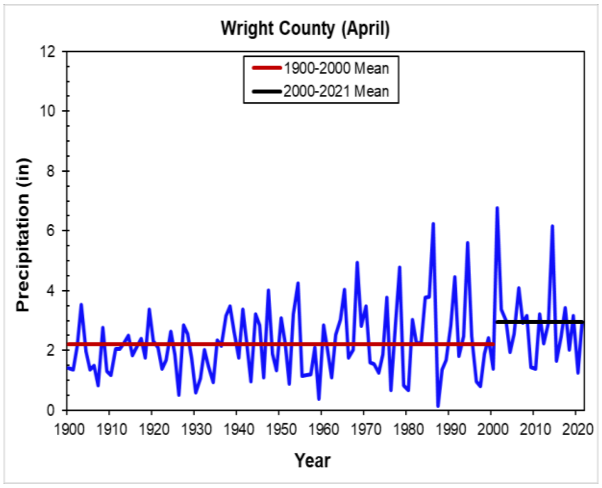

(d)

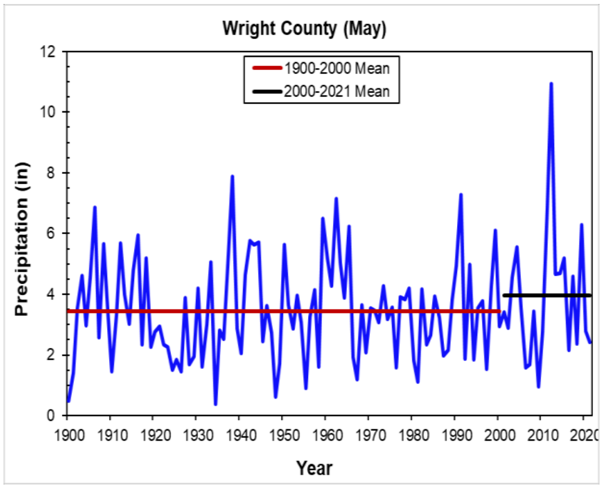
Wright County (May)
1900-2000 Mean
2000-2021 Mean
Precipitation (in)
0
2
4
6
8
10
12
1900
1910
1920
1930
1940
1950
1960
1970
1980
1990
2000
2010
2020
Year

(e)

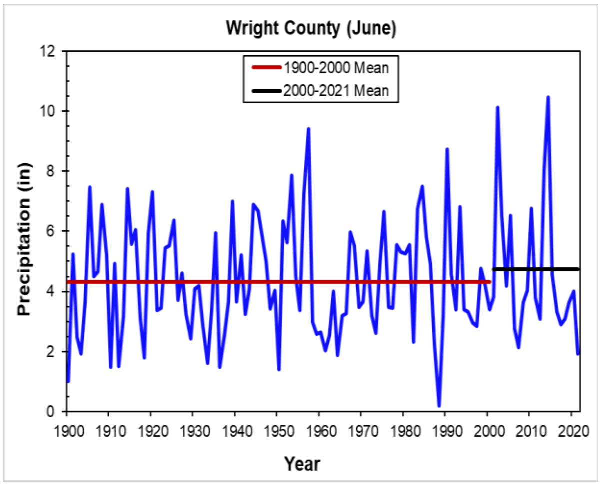
Wright County (June)
1900-2000 Mean
2000-2021 Mean
Precipitation (in)
0
2
4
6
8
10
12
1900
1910
1920
1930
1940
1950
1960
1970
1980
1990
2000
2010
2020
Year

(f)

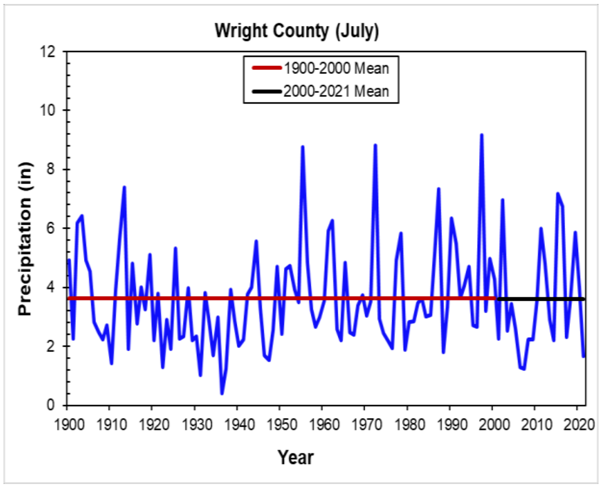
Wright County (July)
1900-2000 Mean
2000-2021 Mean
Precipitation (in)
0
2
4
6
8
10
12
1900
1910
1920
1930
1940
1950
1960
1970
1980
1990
2000
2010
2020
Year

(g)

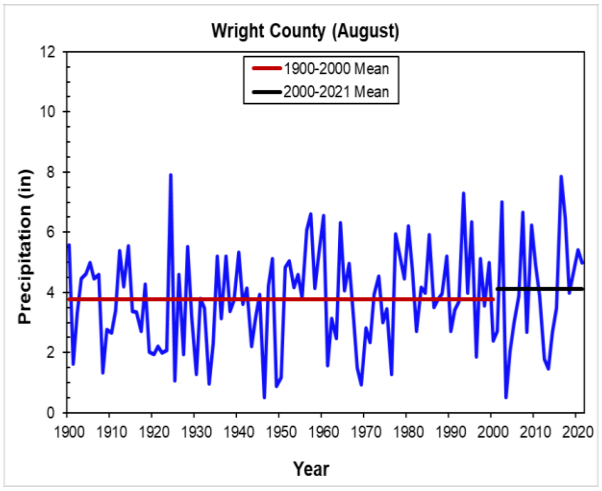
Wright County (August)
1900-2000 Mean
2000-2021 Mean
Precipitation (in)
0
2
4
6
8
10
12
1900
1910
1920
1930
1940
1950
1960
1970
1980
1990
2000
2010
2020
Year

(h)

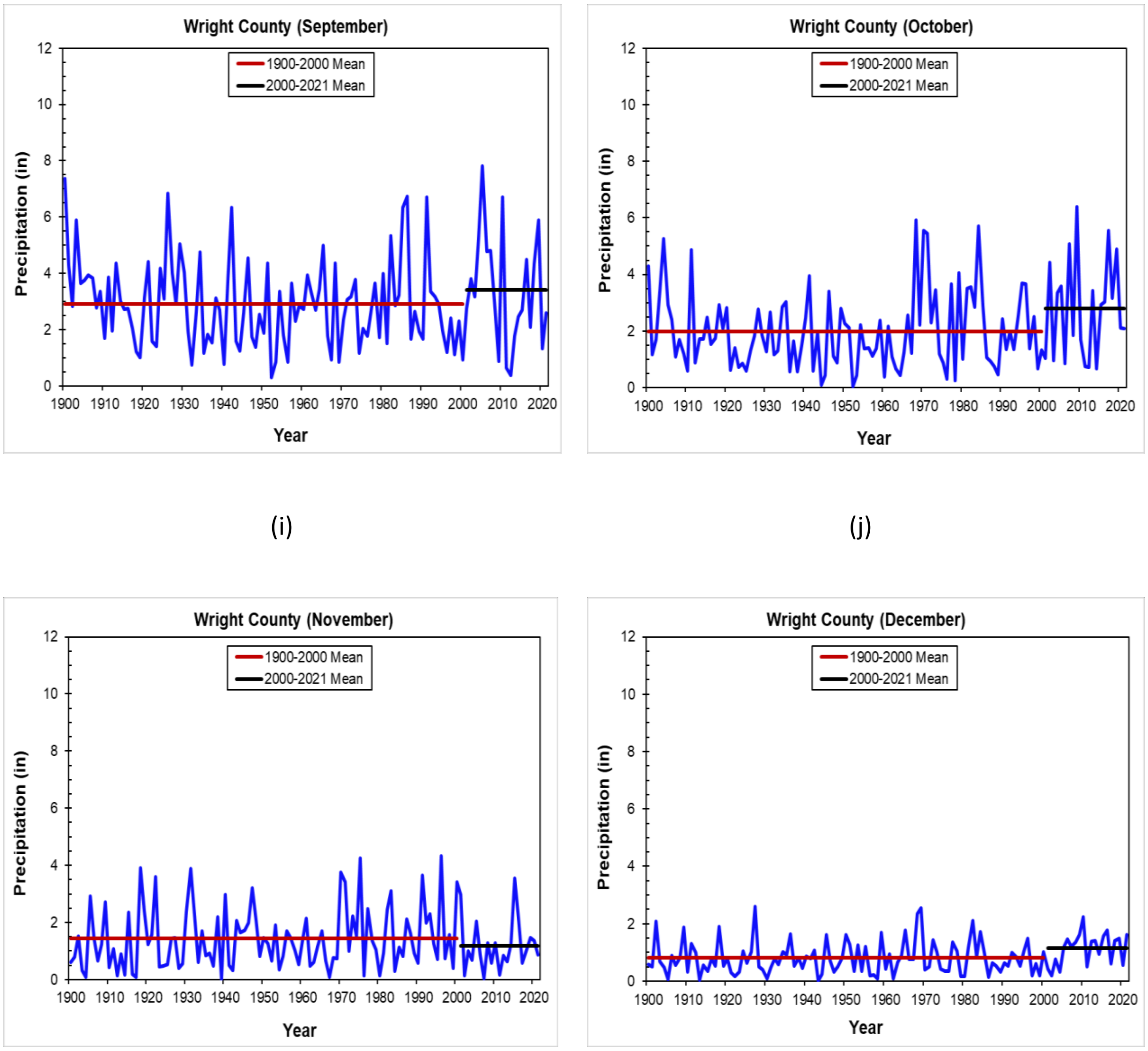

(i)

(j)

(k)

(l)

Figure 1. Historical monthly total precipitation in Wright County for (a) January (b) February (c) March (d) April (e) May (f) June (g) July (h) August (i) September (j) October (k) November, and (l) December

In addition to providing historical weather data, the MnROAD facility has an onsite weather station for accurately capturing weather conditions at MnROAD test sections, including air temperature, atmospheric pressure, precipitation, relative humidity, solar radiation, and wind speed, and it can be easily accessed via the long-term pavement performance (LTPP) info pave system (https://infopave.fhwa.dot.gov/MnRoad/SelectSections). The Federal Highway Administration's (FHWA) LTPP program was initiated in 1987 and it worked with state DOTs to gather research-quality pavement performance and weather data (FHWA, 2022). As part of this program, MnDOT makes weather data and pavement performance data available to the public via the MnROAD-LTPP info pave system. Weather data from MnROAD onsite weather station were downloaded and analyzed to determine the monthly precipitation at the MnROAD facility from 2009 to 2013. The choice of selecting five years of precipitation data was to check changes in moisture trends in MnROAD test cells for those years. **Figure 2** depicts monthly precipitation at the MnROAD facility from 2009 to 2013, along with the mean precipitation line for each year. The mean monthly precipitation in the MnROAD facility was 2.21-inch, 2.54-inch, 2.43-inch, 2.38-inch, and 2.21-inch during 2009, 2010, 2011, 2022, and 2013 respectively, compared to the national average monthly precipitation of 2.69-inch, 2.61-inch, 2.51-inch, 2.29-inch, and 2.59-inch during 2009, 2010, 2011, 2022 and 2013 respectively (https://www.statista.com/statistics/504400/volume-of-precipitation-in-the-us/). The months of June, July, August, and October in 2009 experienced precipitation above the mean precipitation of that year. The minimum precipitation for 2009, 0.17 inches, was recorded in January, and the maximum precipitation value for the year 2009 was 6.29 inches in August. The maximum precipitation for the year 2010 occurred in June (6.83 inches), and the minimum 2010 precipitation was 0.24 inches in February. Precipitation above the mean precipitation for 2010 occurred between May and September, and the maximum precipitation of 6.91 inches and the minimum precipitation of 0.15 inches were recorded during July and November, respectively, for the year 2011. The above-mean precipitation events in 2011 occurred from April to August. In 2012, the maximum precipitation, 12.6 inches, was recorded in May, and the minimum precipitation, 0.17 inches, occurred in January. The only 3-month interval of this year experiencing above-mean precipitation extended from May through June, while above-mean precipitation occurred over a long time during 2013, extending from April to October, excluding August. The highest 2013 precipitation, 5.81 inches, was recorded in June, while the month of December experienced the lowest precipitation, 0.09 inches, in that year. The overall rainfall summary events between 2009 and 2013 were: (i) January, February, March, November, and December that were the driest months of the year experiencing less precipitation (ii) maximum precipitation of 12.6 inches in May 2012, and minimum precipitation of 0.09 inches in December 2013, and (iii) generally, April through October that experienced above-average precipitation.

Figure 3 is a precipitation intensity plot for the MnROAD facility for the years 2009, 2010, 2011, 2012, and 2013, along with a cutoff line to distinguish the heavy precipitation event of that year. The precipitation intensity is defined by per-hour precipitation in inches, and the heavy precipitation event is the highest 1% precipitation for that particular year. Precipitation intensities above 0.80 inch/hr in 2009, 0.88 inch/hr in 2010, 1.1 inch/hr in 2011, 1.05 inch/hr in 2012 and 0.38 inch/hr in 2013 are considered as heavy precipitation in this analysis. There were 13 heavy precipitation events in 2009, 14 heavy precipitation events in 2010, 14 heavy precipitation events in 2011, 13 heavy precipitation events in 2012, and 14 heavy precipitation events in 2013.

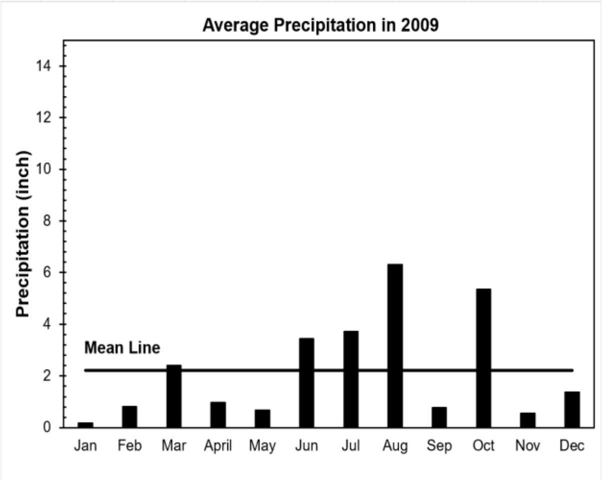
Average Precipitation in 2009
Precipitation (inch)
0
2
4
6
8
10
12
14
Mean Line
Jan
Feb
Mar
April
May
Jun
Jul
Aug
Sep
Oct
Nov
Dec

(a)

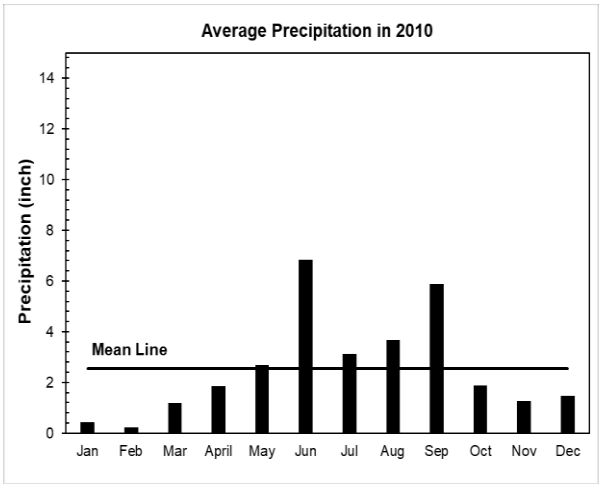
Average Precipitation in 2010
Precipitation (inch)
0
2
4
6
8
10
12
14
Mean Line
Jan
Feb
Mar
April
May
Jun
Jul
Aug
Sep
Oct
Nov
Dec

(b)

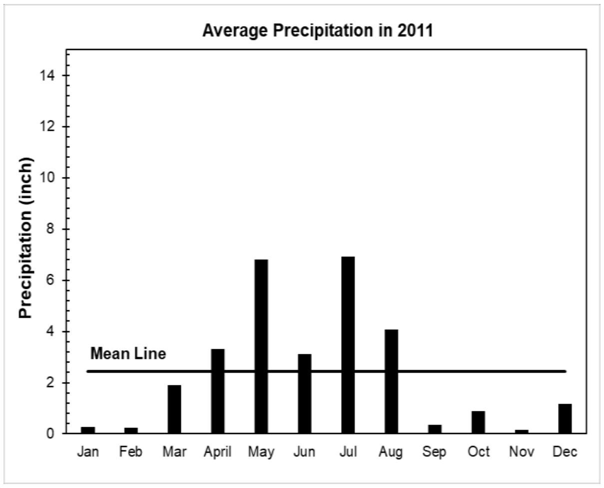
Average Precipitation in 2011
Precipitation (inch)
0
2
4
6
8
10
12
14
Mean Line
Jan
Feb
Mar
April
May
Jun
Jul
Aug
Sep
Oct
Nov
Dec

(c)

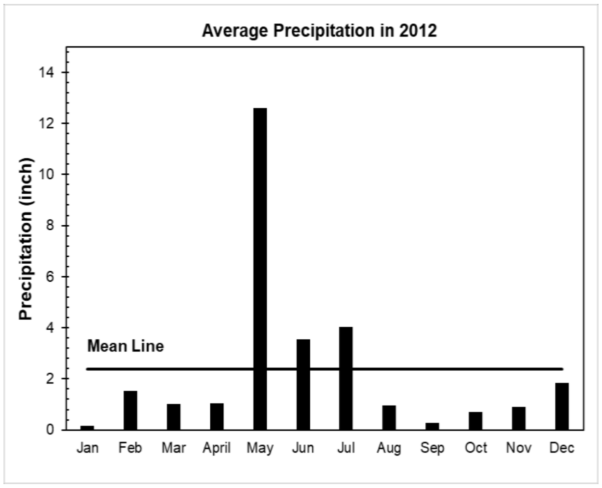
Average Precipitation in 2012
Precipitation (inch)
0
2
4
6
8
10
12
14
Mean Line
Jan
Feb
Mar
April
May
Jun
Jul
Aug
Sep
Oct
Nov
Dec

(d)

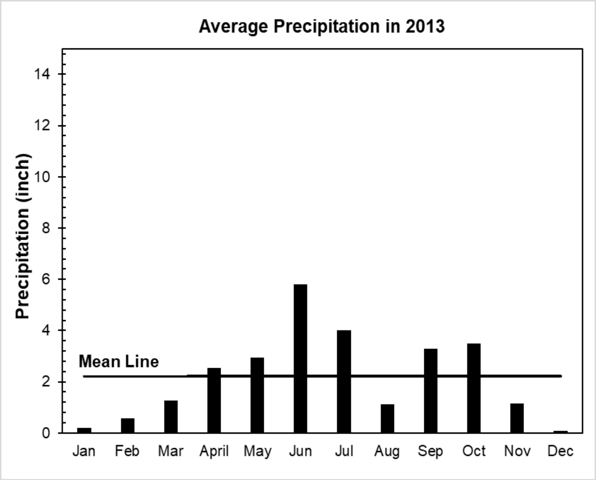

(e)

Figure 2. MnROAD onsite weather stations monthly precipitation at MnROAD facility for the year of (a) 2009, (b) 2010, (c) 2011, (d) 2012, and (e) 2013

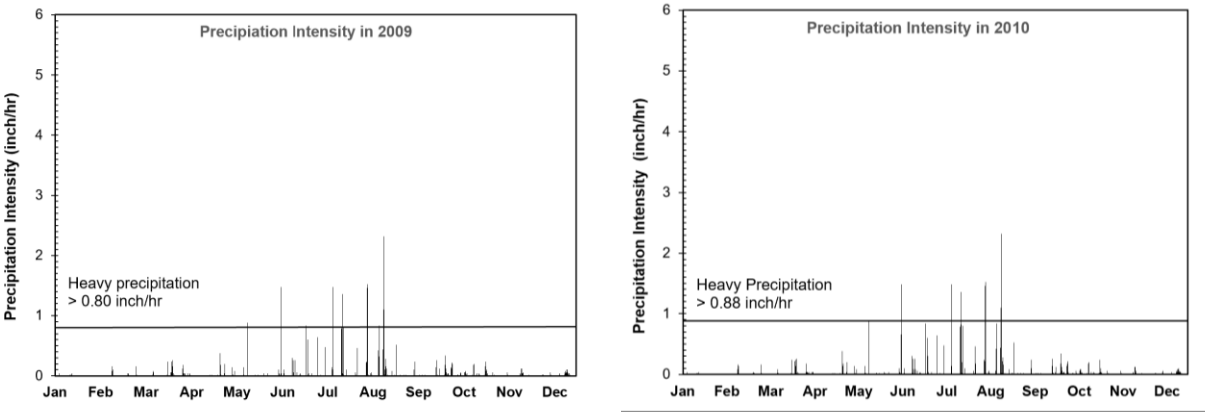

(a)

(b)

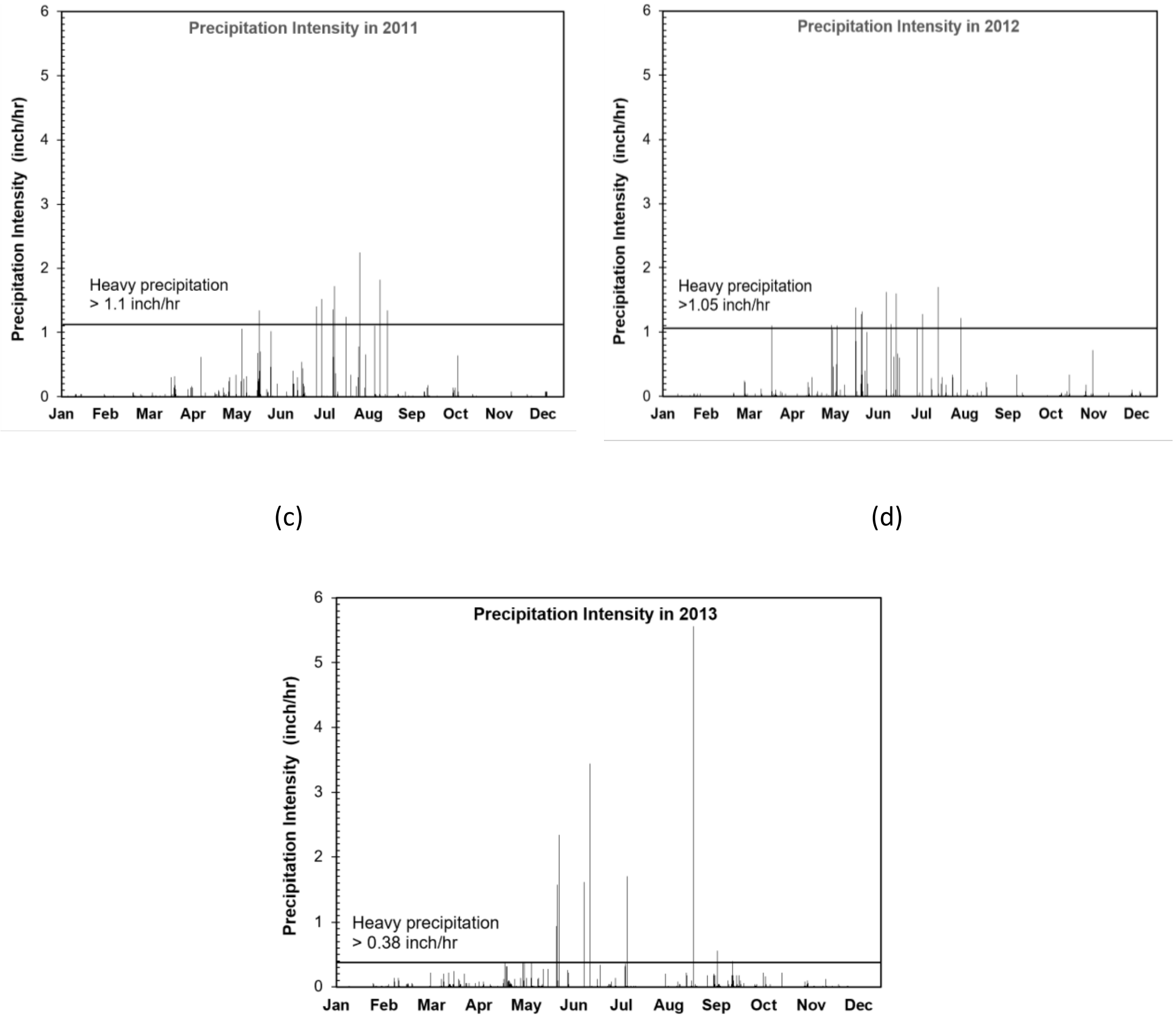

(c) (d)

(e)

Figure 3. MnROAD onsite weather stations collected precipitation intensity data at the MnROAD facility for the year of (a) 2009, (b) 2010, (c) 2011, (d) 2012 and (e) 2013

2.3 Cell Selection And Moisture Data Analysis

This section focuses on information necessary to perform moisture data analysis of selected cells. The MnROAD facility has more than 50 unique test cells built from different types of base, subbase, and surface course materials (MnDOT, 2022a) , and MnDOT operates this facility and collects detailed pavement performance data over time. The test cells are located on several roadway segments: a 3.5-mile long I-94 original westbound, a 3.5-mile I-94 Mainline, and a 2.5-mile low-volume road. Sensors for collecting both environmental data and dynamic load-response data are located in different pavement layers. Environmental sensors measure moisture content, temperature, soil pressure, pore water pressure, strain, electrical resistivity, and humidity, and dynamic sensors collect real-time load response data, including stress, strain, pore water pressure, and accelerometer data (MnDOT, 2022b) using MnROAD test vehicles. For this study, four test cells were selected from the I-94 mainline and one test cell was selected from the low-volume road. These cell locations included both conventional base aggregate and recycled base aggregate. One of the primary criteria for cell selection was to check that there was at least one moisture sensor available in the base, subbase, and subgrade layers. Also, missing data from any moisture sensor should be less than 20% of the total data count if it is to be considered as a potential cell for analysis. EW-Decagon moisture-sensor data were accessed through the MnROAD Oracle database. The cells selected for moisture data analysis included Cell 16, Cell 18, Cell 20, and Cell 22 from MnROAD Mainline and Cell 78 from MnROAD low-volume road. MnROAD Decagon 5TE sensors use dielectric permittivity to measure the moisture content of base and subbase materials. The Meter Group (formerly Decagon) provides generic calibration coefficients to convert raw data into volumetric moisture content in mineral soils. Since these calibration coefficients are material-specific, this requires developing calibration functions for local materials. The MnROAD staff initiated a calibration approach for determining calibration functions for base and subbase materials at locations where those sensors were installed (MnROAD 2013). **Table 1** lists Decagon 5TE moisture sensor coefficients for a linear calibration function for calculating volumetric moisture content.

Table 1. Calibration coefficients for Decagon 5TE moisture sensor and Proctor parameters

			Calibration Coefficients	
Material	MDD (lb/ft^3)	OMC (%)	Slope, a	Intercept, b
CLS6	128.7	6.8	0.0006	-0.1438
CLS5	132	7.3	0.0003	-0.0239
CLS3	128	9.4	0.0004	-0.0481
SG	132	7.8	0.0005	-0.0908
Clay	117	13.2	0.0003	-0.0021

Note: MDD = Maximum dry density, OMC = Optimum moisture content, CLS6 = Class 6 aggregates, CLS5 = Class 5 aggregates, CLS3 = Class 3 aggregates, SG = Select granular

2.3.1 Cell 16

Figure 4 shows the structural layout of Cell 16 from the MnROAD mainline, comprised of recycled concrete aggregate and Class 3 aggregate base layer. This Cell was reconstructed in 2008, and its layer configuration consists of a 5-inch warm-mix asphalt surface course, a 12-inch recycled-concrete aggregate base, a 12-inch Class 3 aggregate base, a 7-inch granular subbase, and a clay subgrade. The recycled concrete aggregate base layer hosts 2 EW-Decagon moisture sensors at 7-inch and 12-inch depths, while the Class 3 aggregate base has two EW-Decagon moisture sensors at 18-inch and 24-inch depths, one EW-Decagon moisture sensor at the subbase layer, and three EW-Decagon moisture sensors in the subgrade layer at different depths. Sensor arrangement and locations are documented in

Table 2.

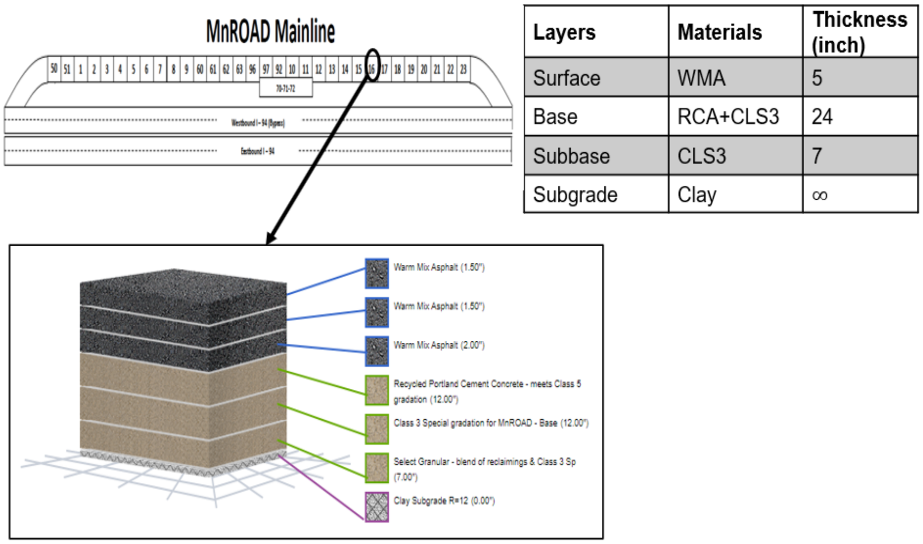

Layers	Materials	Thickness (inch)
Surface	WMA	5
Base	RCA+CLS3	24
Subbase	CLS3	7
Subgrade	Clay	∞

Figure 4. Layer thickness and material information for the MnROAD Cell 16 (MnROAD-LTPP InfoPave system)

Table 2. Arrangement of moisture sensors in Cell 16 and their locations in pavement layers

	EW – Decagon Moisture Sensor							
Sensors:	S101	S102	S103	S104	S105	S106	S107	S108
Depths (in)	7	12	18	24	36	48	60	72
Materials	RCA	RCA	CLS3	CLS3	SG	Clay	Clay	Clay
Layer	Base	Base	Base	Base	subbase	Subgrade	Subgrade	Subgrade
Offset (ft)	6.44	6.44	6.44	6.44	6.44	6.44	6.44	6.44

Note: RCA = Recycled concrete aggregates, CLS3 = Class 3 aggregates, SG = Select granular

Moisture distribution trends of the base, subbase, and subgrade layers along with precipitation data for Cell 16 during 2009 are illustrated in **Figure 5**. The volumetric moisture content of both RCA base and Class 3 aggregate base layers was consistently higher from April to November and fluctuated around 20% for RCA base and 25% for Class 3 aggregate base. Inconsistency was observed between heavy precipitation events and at the onset of the moisture peak that started earlier than the higher precipitation events. At the same time, the volumetric moisture content was consistently higher during high-precipitation events. The earlier peak volumetric moisture content in March results from the foundation system's free water movement due to the thawing event at that location. The subbase and subgrade layers of Cell 16 exhibited similar trends of volumetric moisture distribution, except for outlier data found during March and December when the sensor recorded a volumetric moisture content value above 50%. The trend of volumetric moisture content of Cell 16 during 2010, 2011, 2012, and 2013 is illustrated in Appendix A1-A4.

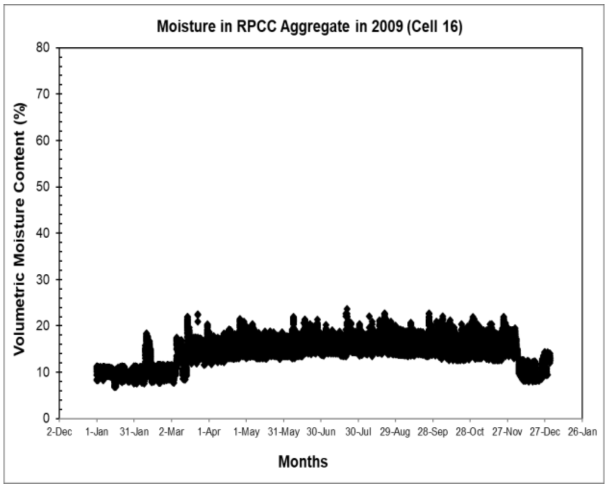

(a)

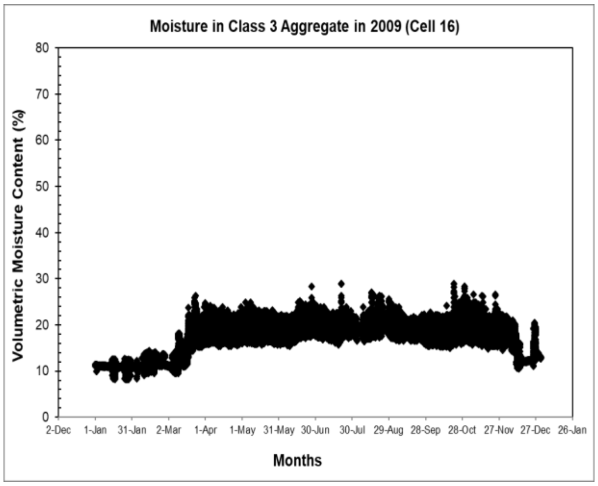

(b)

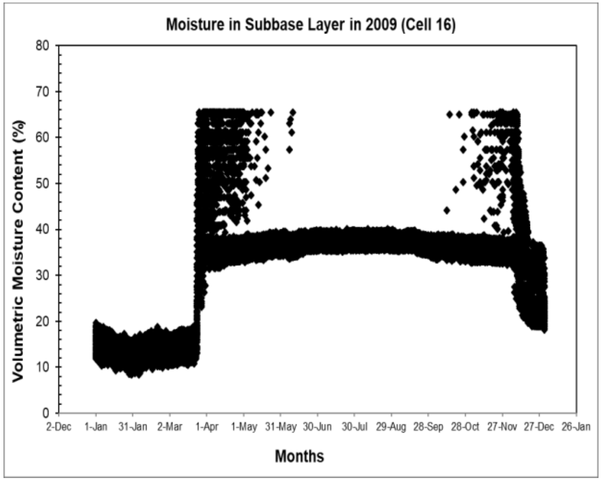

(c)

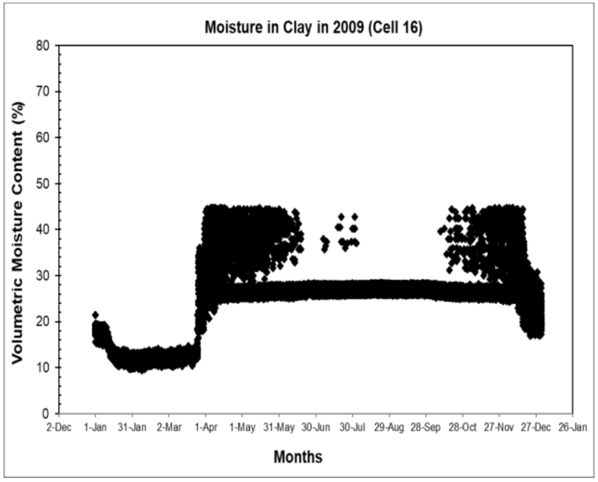

(d)

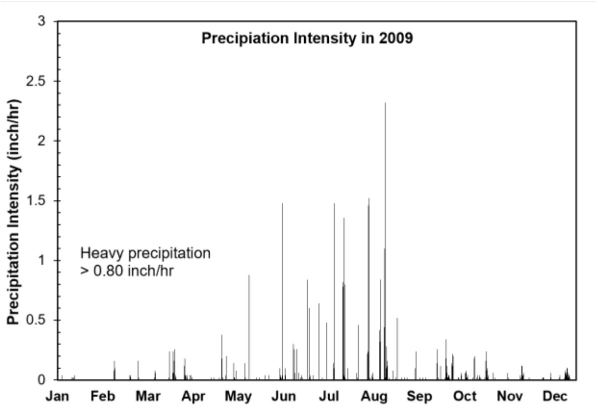

(e)

Figure 5. Volumetric moisture content trend of Cell 16 in 2009 for (a) RCA base, (b) Class 3 aggregate base, (c) SG subbase, and (d) clay subgrade layer along with (e) precipitation data

2.3.2 Cell 18

The structural layout of Cell 18, including layer thickness and material information, is illustrated in **Figure 6**. The base layer of Cell 18 has both RAP aggregate and a Class 3 aggregate base layer, while the structural layout of Cell 18 was comprised of a 5-inch warm-mix asphalt surface course, a 12-inch RAP aggregate base, a 12-inch Class 3 aggregate base, a 7-inch granular subbase, and a clay subgrade. The EW-Decagon moisture sensor arrangement and their locations in Cell 18 are shown in **Table 3**. A total of 8 EW-Decagon moisture sensors were located in the different layers; three were embedded in the subgrade, two of them in the subbase, with the remaining three sensors in the base layer. These sensors collected moisture data from those layers during 2008 to 2015.

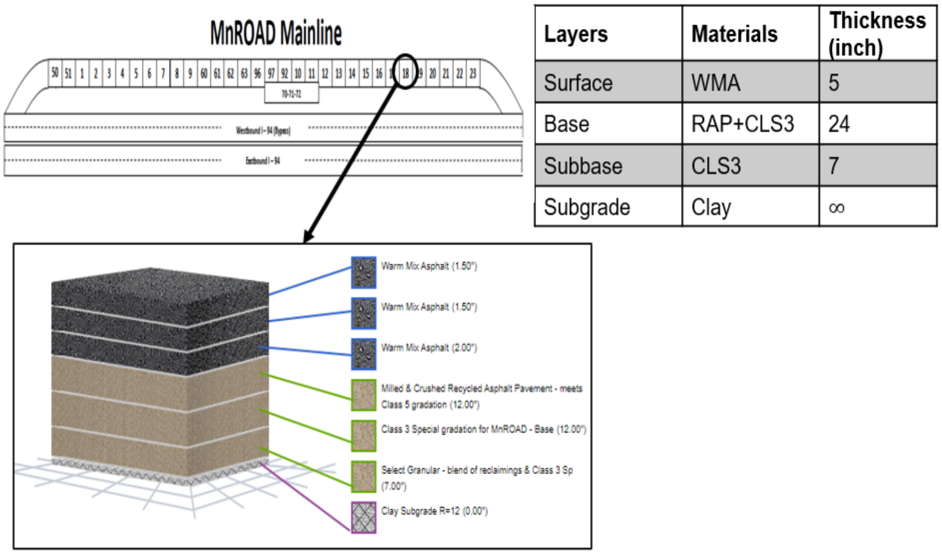

Layers	Materials	Thickness (inch)
Surface	WMA	5
Base	RAP+CLS3	24
Subbase	CLS3	7
Subgrade	Clay	∞

Figure 6. Layer thickness and material information for MnROAD Cell 18 (MnROAD-LTPP InfoPave system)

Table 3. Arrangement of moisture sensors in Cell 18 and their locations in pavement layers

	EW – Decagon Moisture Sensor							
Sensors:	S101	S102	S103	S104	S105	S106	S107	S108
Depths (in)	72	60	48	36	30	18	15	6
Materials	Clay	Clay	Clay	SG	SG	CLS3	RAP	RAP
Layer	Subgrade	Subgrade	Subgrade	Subbase	Subbase	Base	Base	Base
Offset (ft)	5.65	5.65	5.65	5.65	5.65	5.65	5.65	5.65

Note: RAP = Recycled asphalt pavement aggregates, CLS3 = Class 3 aggregates, SG = Select granular

Figure 7 shows the volumetric moisture contents of the different pavement layers of Cell 18, including the moisture distribution trend of the RAP aggregate base, the Class 3 aggregate base, granular subbase, and the clay subgrade layer along with precipitation data. The volumetric moisture trend of the RAP aggregate base also exhibited an earlier peak before the occurrence of heavy precipitation. This earlier peak of the volumetric moisture content is related to the thawing event of that year that happened in April. The higher moisture content of the RAP aggregate base layer could be explained by the heavy precipitation events of that year that began at the end of May. Since the availability of data for the Class 3 aggregate base layer was insufficient for making any comparison, the Class 3 aggregate base layer used the EW-Decagon moisture sensor data from January to May. The volumetric moisture content of the Class 3 aggregate base was the lowest and reached zero, inconsistent with the precipitation events. The volumetric moisture content of both the subbase and subgrade layer exhibited dramatic increases during April and November that could not be explained by the precipitation event; the moisture sensors recorded a volumetric moisture content above 50% during that time. Volumetric moisture content trends for 2010, 2011, and 2012 are shown in Appendices A5-A6.

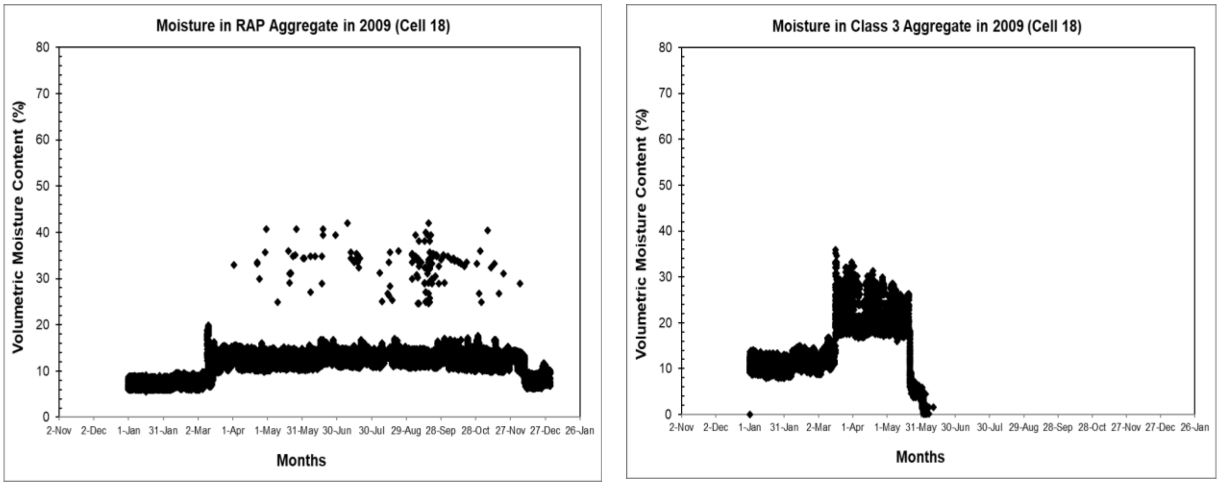

(a) (b)

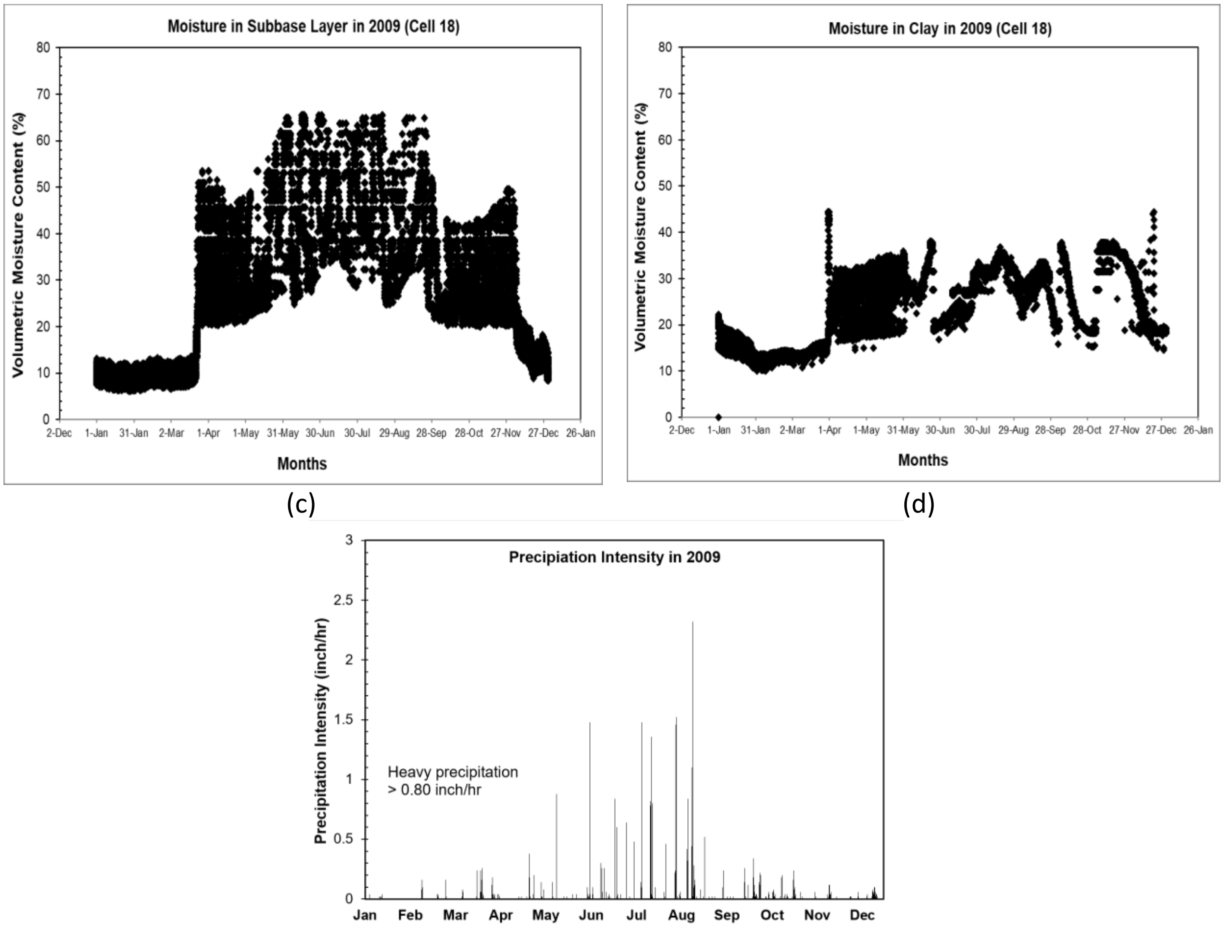

(c)

(d)

(e)

Figure 7. Volumetric moisture content trend of Cell 18 in 2009 for (a) RAP base, (b) Class 3 aggregate base, (c) SG subbase, and (d) clay subgrade layer along with (e) precipitation data

2.3.3 Cell 20 and Cell 22

Cells 20 and 22 were selected for characterizing the conventional Class 5 and Class 3 aggregate base layer response to precipitation events. The structural components of Cell 20 were a 5-inch surface layer combination of hot-mix asphalt (HMA) and standard RAP, a 12-inch Class 5 aggregate and 12-inch Class 3 aggregate base layer, a 7-inch granular reclaimed subbase, and a clay subgrade layer. The structural layout of Cell 20 is illustrated in **Figure 8.** The structural configuration of Cell 22 is the same as that of Cell 20, except that the surface course of Cell 22 has a mix of HMA and fractionated RAP; **Figure 9** shows the layer thickness and material information for Cell 22. Both Cells had eight EW-Decagon moisture sensors installed at various locations on the pavement. The locations and arrangements of sensors for Cell 20 and Cell 22 are listed in **Table 4** and

Table 5, respectively. Both cells hosted four EW-Decagon moisture sensors in the base layer, one sensor in the subbase layer, and three EW-Decagon moisture sensors in the subgrade layer. These two Cells were constructed in 2008, and the EW-Decagon moisture sensors stored moisture data from 2008 to 2015.

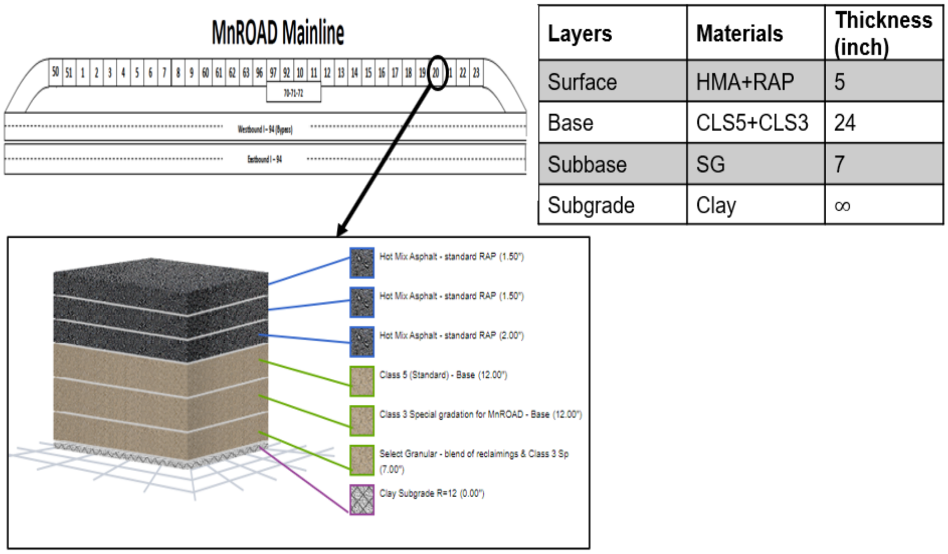

Layers	Materials	Thickness (inch)
Surface	HMA+RAP	5
Base	CLS5+CLS3	24
Subbase	SG	7
Subgrade	Clay	∞

Figure 8. Layer thickness and material information for MnROAD Cell 20 (MnROAD-LTPP InfoPave system)

Table 4. Arrangement of moisture sensors in Cell 20 and their locations in pavement layers

	EW – Decagon Moisture Sensor							
Sensors:	S101	S102	S103	S104	S105	S106	S107	S108
Depths (in)	7	15	17	23	30	36	60	72
Materials	CLS5	CLS5	CLS3	CLS3	SG	Clay	Clay	Clay
Layer	Base	Base	Base	Base	Subbase	Subgrade	Subgrade	Subgrade
Offset (ft)	-5.33	-5.33	-5.33	-5.33	-5.33	-5.33	-5.33	-5.33

Note: CLS5 = Class 5 aggregates, CLS3 = Class 3 aggregates, SG = Select granular

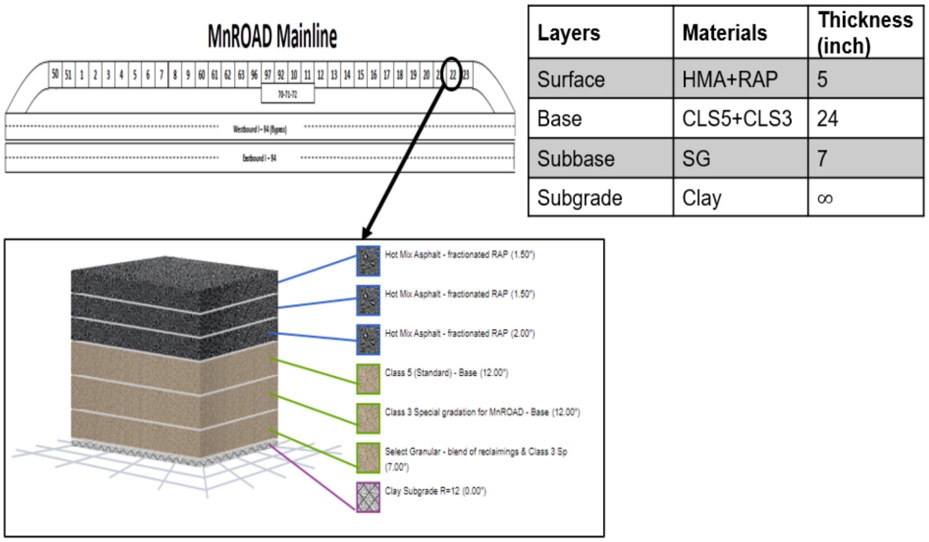

Layers	Materials	Thickness (inch)
Surface	HMA+RAP	5
Base	CLS5+CLS3	24
Subbase	SG	7
Subgrade	Clay	∞

Figure 9. Layer thickness and material information for MnROAD Cell 22 (MnROAD-LTPP InfoPave system)

Table 5. Arrangement of moisture sensors in Cell 22 and their locations in pavement layers

	EW – Decagon Moisture Sensor							
Sensors:	S101	S102	S103	S104	S105	S106	S107	S108
Depths (in)	7	15	17	24	30	36	60	72
Materials	CLS5	CLS5	CLS3	CLS3	SG	Clay	Clay	Clay
Layer	Base	Base	Base	Base	Subbase	Subgrade	Subgrade	Subgrade
Offset (ft)	5.33	5.33	5.33	5.33	5.33	5.33	5.33	5.33

Note: CLS5 = Class 5 aggregates, CLS3 = Class 3 aggregates, SG = Select granular

Figure 10 shows the 2009 volumetric moisture content trend of Cell 20, including the moisture trend of the conventional Class 5 aggregate and Class 3 aggregate base, the granular subbase, the clay subgrade layer, and precipitation data. The volumetric moisture content of Class 5 base aggregate reached a peak level in March and December when the precipitation in that area was at a low level, and the Class 3 aggregate base exhibited consistently higher moisture content throughout the higher-precipitation months. The volumetric moisture content in the subbase and the subgrade layer also increased in response to heavy precipitation events, and the volumetric moisture trend of those two layers reflects the response expected in response to the precipitation of that year. The volumetric moisture content trends of Cell 20 during 2010, 2011, and 2012 are illustrated in Appendix A7-A9.

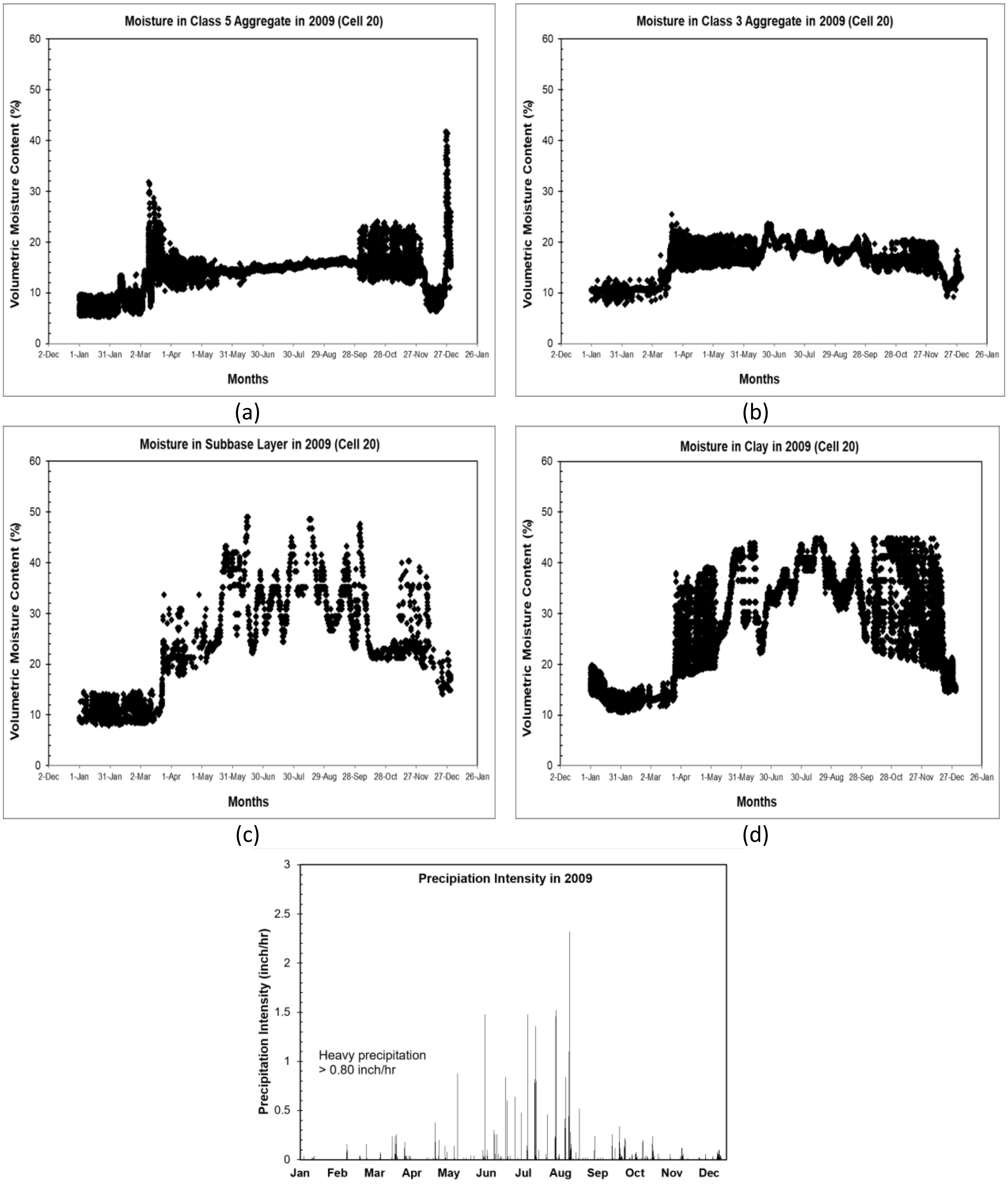

(a)

(b)

(c)

(d)

(e)

Figure 10. Volumetric moisture content trend of Cell 20 in 2009 for (a) Class 5 aggregate base, (b) Class 3 aggregate base, (c) SG subbase, and (d) clay subgrade layer along with (e) precipitation data

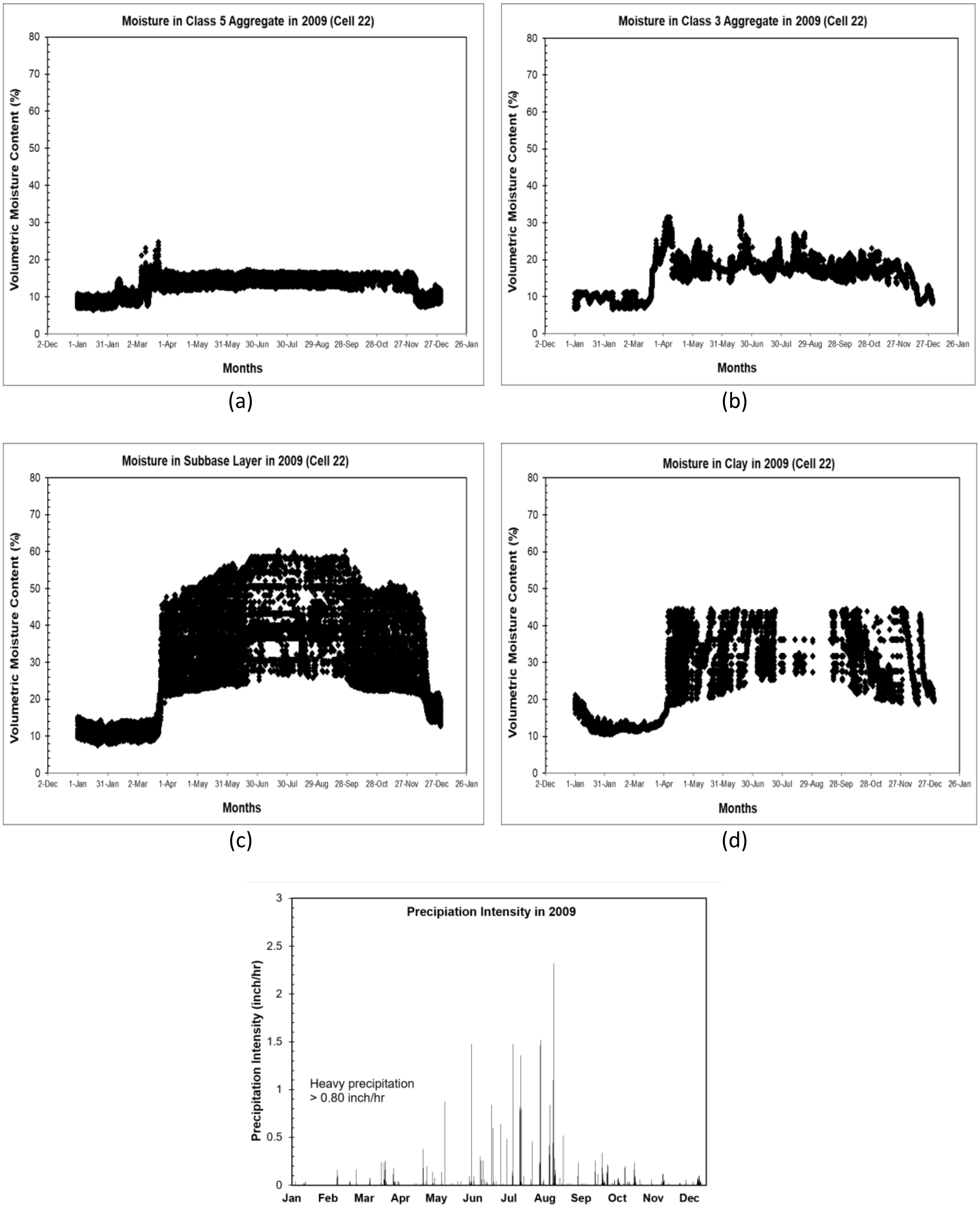

(a) (b)

(c) (d)

(e)

Figure 11. Volumetric moisture content trend of Cell 22 in 2009 for (a) Class 5 aggregate base, (b) Class 3 aggregate base, (c) SG subbase, and (d) clay subgrade layer along with (e) precipitation data

Figure 11 shows the volumetric moisture content of Cell 22, that has a layer structure similar to that of Cell 20, with a Class 5 aggregate and Class 3 aggregate base, a granular subbase, and a clay subgrade layer. Class 5 and Class 6 aggregate bases exhibited similar trends in volumetric moisture change. While the peak of the volumetric moisture content trend occurred earlier than expectations based on that year's precipitation due to thawing, the month of higher precipitation results in consistently higher moisture content during that time period. The earlier peak could be associated with the thawing event at that location that began in March. The volumetric moisture content in the subbase layer climbed to above 50% during the heavy precipitation, and the trend of moisture changes is consistent with the precipitation variation over the year. The subgrade layer exhibited a trend similar to that of the subbase layer, with a higher moisture level at the time of heavy precipitation. Appendix A10-A12 shows the trend of volumetric moisture content of Cell 22 in 2010, 2011, and 2012.

2.3.4 Cell 78

Figure 12. describes Cell 78 selected from a MnROAD low-volume road with a conventional Class 6 aggregate base layer. The 4-inch surface layer of this Cell was built with polymer-modified hot-mix asphalt. The structural layout of this Cell included a 4-inch polymer-modified HMA layer, an 8-inch Class 6 aggregate base layer, and a clay subgrade layer. Three (3) EW-Decagon moisture sensors were embedded in the base layer, and five such sensors were located in the subgrade layer. These sensors collected base and subgrade layer moisture information from 2007 to 2015. **Table 6** documents the EW-Decagon moisture sensor arrangement of Cell 78.

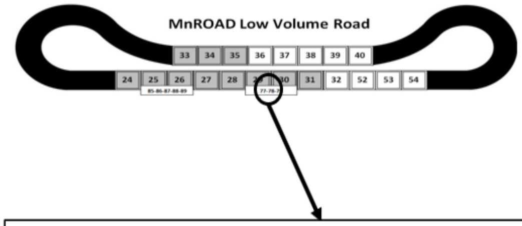

Layers	Materials	Thickness (inch)
Surface	HMA+PPA	4
Base	CLS6	8
Subgrade 1	Clay Borrow	5
Subgrade 2	Clay	∞

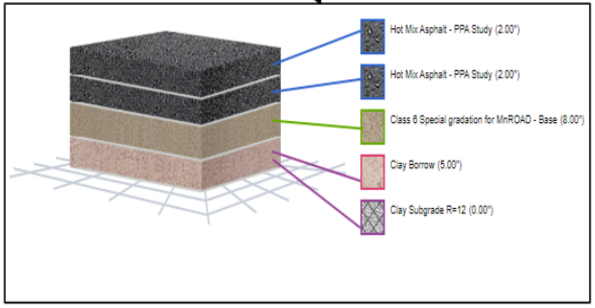

Figure 12. Layer thickness and material information for MnROAD low volume road Cell 78 (MnROAD-LTPP InfoPave system)

Table 6. Arrangement of moisture sensors in Cell 78 and their locations in pavement layers

	EW – Decagon Moisture Sensor							
Sensors:	S101	S102	S103	S104	S105	S106	S107	S108
Depths (in)	6	9	12	24	36	48	60	72
Materials	CLS6	CLS6	CLS6	Clay	Clay	Clay	Clay	Clay
Layer	Base	Base	Base	Subgrade	Subgrade	Subgrade	Subgrade	Subgrade
Offset (ft)	-6	-6	-6	-6	-6	-6	-6	-6

Note: CLS6 = Class 6 aggregates

The volumetric moisture content for the Class 6 aggregate base, along with precipitation data of Cell 78 during the year 2009, is shown in **Figure 13. ,** revealing a trend similar to that of the base layer in Cell 22. The higher moisture in the Class 6 aggregate could be a result of the expected precipitation of that year, and the transition of moisture level from low to high happened earlier than during the heavy precipitation time. The earlier peak is related to the thawing event since the temperature rose above the freezing point in March. The subgrade layer's moisture data was missing in 2009 because the sensors located in the subgrade recorded no moisture data. Moisture trends for the base and subgrade layer for the years 2010 and 2011 are shown in Appendix A13-A14.

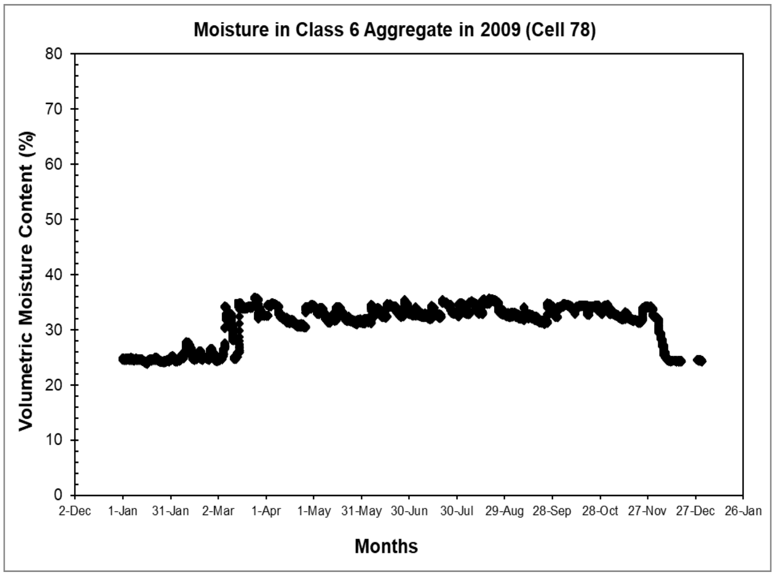

(a)

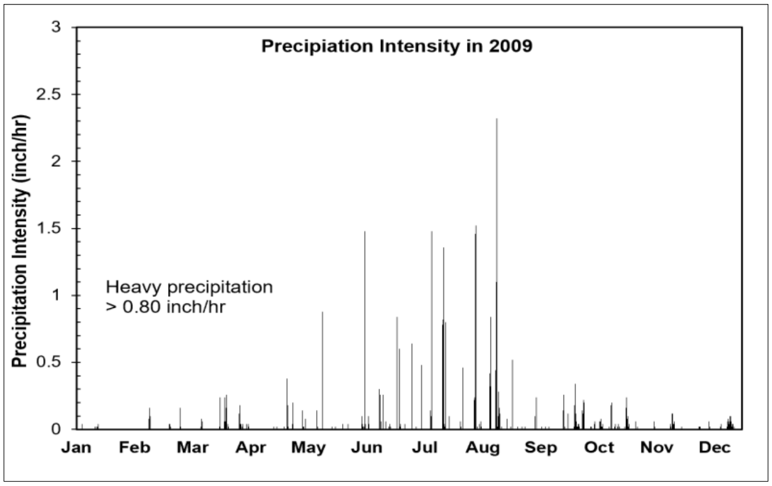

(b)

Figure 13. Volumetric moisture content trend of Cell 78 in 2009 for (a) Class 6 aggregate base along with (b) precipitation data

2.3.5 Cell 127

Cell 127 of low-volume MnROAD was constructed to study the use of large stone aggregate as a subbase layer. The Cell has a 3.5-inch HMA layer, 6-inch Class 6 base aggregate, and 18-inch large stone subbase (LSSB) over the clay subgrade. The structural layout of the Cell 127 is shown in Figure 14. Three EW-Decagon moisture sensors were embedded in this Cell at different depths: one in the base layer, and two in the subgrade layer. These sensors collected base and subgrade layer moisture information between 2017 and the present time. Table 7 documents the EW-Decagon moisture sensor arrangement of Cell 127.

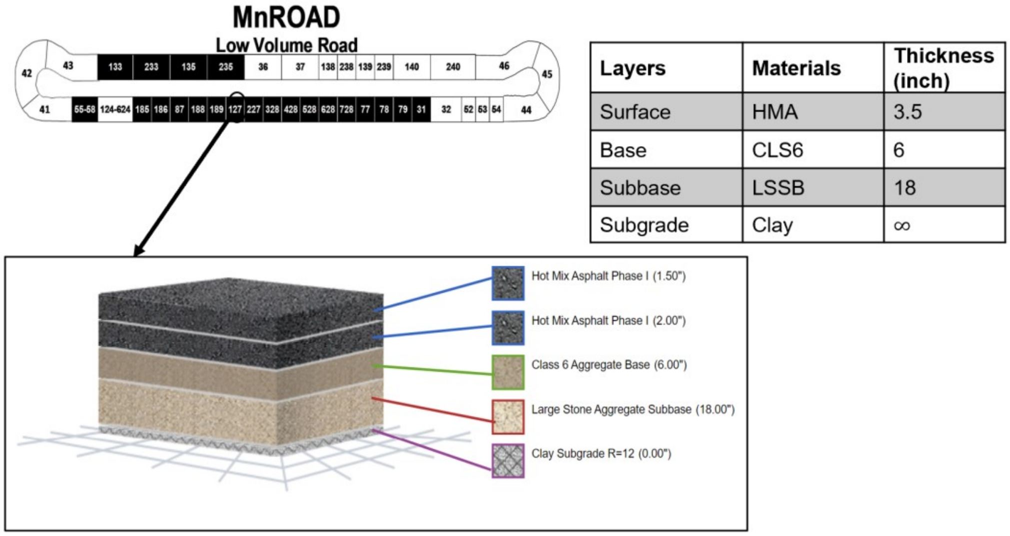

Layers	Materials	Thickness (inch)
Surface	HMA	3.5
Base	CLS6	6
Subbase	LSSB	18
Subgrade	Clay	∞

Figure 14. Layer thickness and material information for MnROAD low volume road Cell 127 (MnROAD-LTPP InfoPave system)

Table 7. Arrangement of moisture sensors in Cell 127 and their locations in pavement layers (Cetin et al., 2021)

EW – Decagon Moisture Sensor			
Sensors:	S101	S102	S103
Depths (in)	6.5	29	36
Materials	CLS6	Clay	Clay
Layer	Base	Subgrade	Subgrade
Offset (ft)	11	11	11

Note: CLS6 = Class 6 aggregates

Figure 15 depicts the volumetric moisture content of the Class 6 base aggregate along with precipitation data of Cell 127 and precipitation at the MnROAD low volume facility during the year 2020. The trend of moisture change for Cell 127 base aggregate is similar to that for the Cell 78 base aggregate, exhibiting an earlier peak compared to the start of the heavy precipitation during the year 2020. The earlier peak in March could be related to the thawing event of that year that allowed frozen water to become free water in the foundation system. During the heavy precipitation event in 2020, the Class 6 aggregate consistently experienced higher moisture, possibly related to the heavy summer precipitation events.

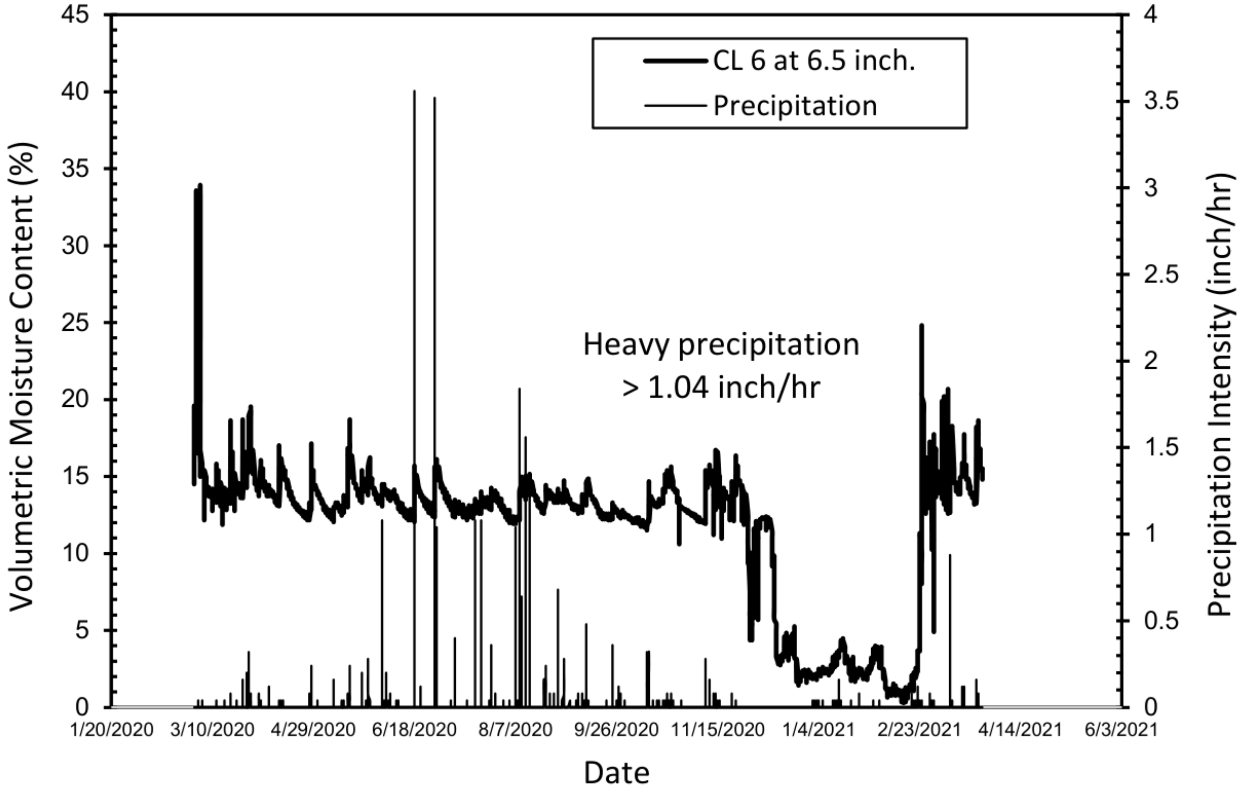

Figure 15. Volumetric moisture content trend of Cell 127 in 2020 for Class 6 aggregate base along with precipitation data (collected from Technical Advisory Panel [TAP] member)

2.3.6 Cell 188

Cell 188 of the MnROAD low volume road was constructed to study the performance of conventional Class 6 limestone aggregate base constructed atop the select granular subbase layer. **Figure 16** shows the layer structure of Cell 188, that has a 3.5-inch HMA layer, 12-inch Class 6 limestone aggregate, 3.5-inch select granular subbase, and clay subgrade soils. The installed moisture sensor information of the Cell 188 is included in **Table 8**. Cell 188 has four moisture sensors embedded at different depths of the layer. The base layer has two moisture sensors at the top and bottom of the layer to check the moisture content of the coating at different depths. Both subbase and subgrade have one sensor for gathering moisture information. **Figure 17** shows the volumetric moisture content of Class 6 base aggregate during 2020 and precipitation at the MnROAD facility at the same time. The volumetric moisture content data collected from both sensors in the base layer are included to check the variation of the moisture content at different depths of the base layer. The early peak volumetric moisture content could be the response to thawing events that release free water into the pavement foundation system. The occurrence of heavy precipitation during the year 2020 leads to the consistently higher moisture content in a base layer that could be confirmed by the data collected by both sensors.

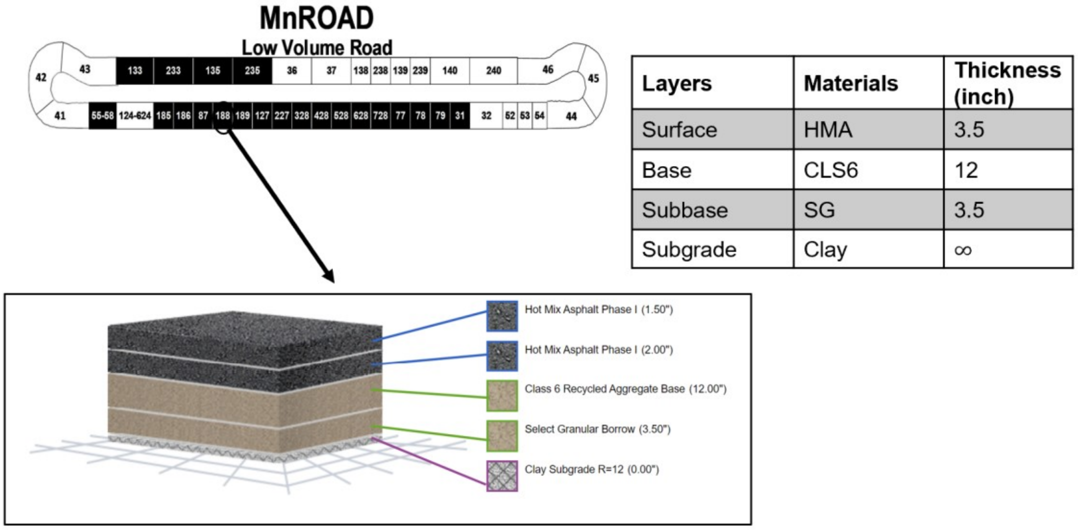

Layers	Materials	Thickness (inch)
Surface	HMA	3.5
Base	CLS6	12
Subbase	SG	3.5
Subgrade	Clay	∞

Figure 16. Layer thickness and material information for MnROAD low volume road Cell 188 (MnROAD-LTPP InfoPave system)

Table 8. Arrangement of moisture sensors in Cell 188 and their locations in pavement layers (Cetin et al., 2021)

EW – Decagon Moisture Sensor				
Sensors:	S101	S102	S103	S104
Depths (in)	5	14	17	20.5
Materials	CLS6	ClS6	SG	Clay
Layer	Base	Base	Subbase	Subgrade
Offset (ft)	-4.8	-4.8	-4.8	-4.8

Note: CLS6 = Class 6 aggregates, SG – Select granular

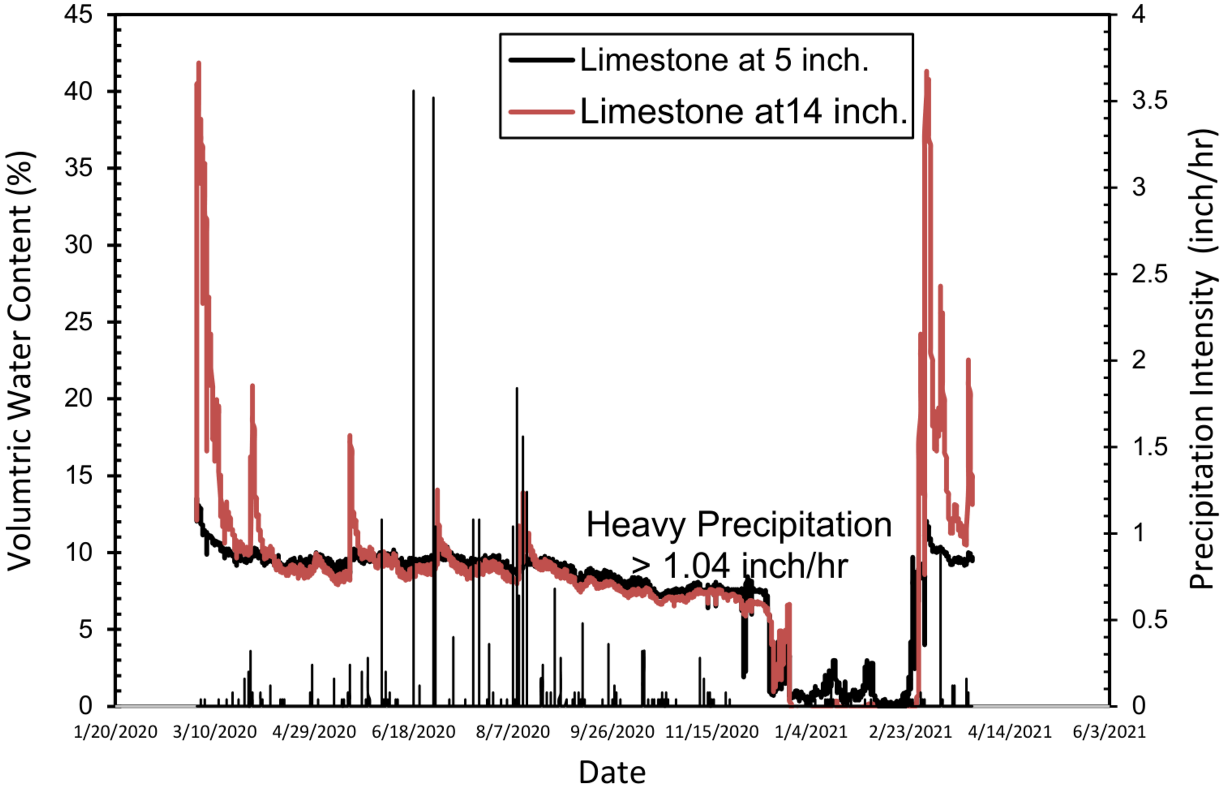

Figure 17. Volumetric moisture content trend of Cell 188 in 2020 for Class 6 limestone along with precipitation data (collected from TAP member)

2.3.7 Cell 189

Cell 189 of the MnROAD low volume road was constructed in 2017 to study the performance of recycled base aggregate (RAB) comprised of both recycled concrete aggregate (RCA) and recycled asphalt pavement (RAP). The layer structure of Cell 189 is presented in **Figure 18;** it has a 3.5-inch HMA layer, a 12-inch Recycled aggregate base (RCA+RAP), a 3.5-inch select granular subbase, and clay subgrade soils. Similarly to Cell 188, four moisture sensors are installed in this cell; two in the recycled base layer; one in the subbase layer, and one in the subgrade layer. Installation depth, offset, and corresponding layer information is included in **Table 9**. The volumetric moisture content of the recycled base layer, including both sensors' data, is presented in **Figure 19**, representing both volumetric moisture content and precipitation data during the year 2020. The response of the recycled base aggregate layer is similar to that of the conventional Class 6 aggregate base layer, except that the sensors at the lower depth measured less volumetric moisture content compared to the sensor at the top of the layer. This could be associated with the lower permeability of the recycled base aggregate material due to higher concentration of fine particles; detailed laboratory tests could explain this phenomenon. Like conventional base aggregate, recycled base aggregate experienced early peak volumetric moisture in

March that could result from thawing events. In summer, the heavy precipitation also caused the peak volumetric moisture content in the base layer.

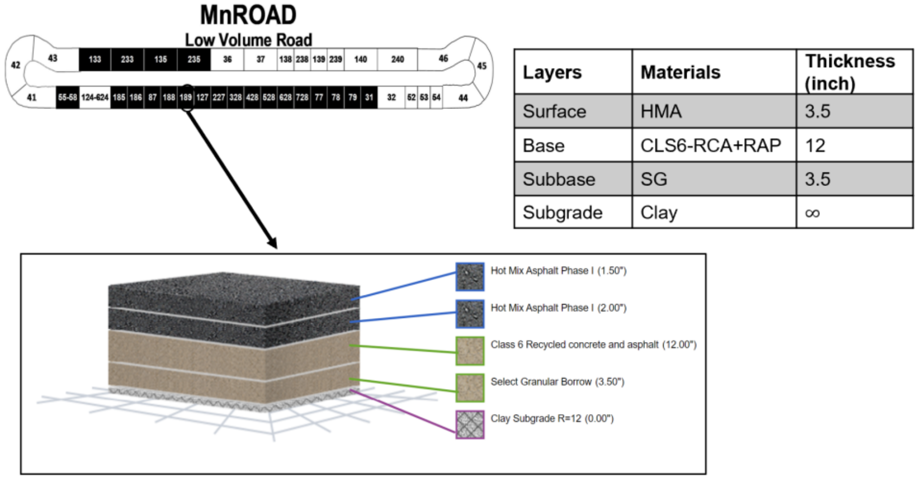

Layers	Materials	Thickness (inch)
Surface	HMA	3.5
Base	CLS6-RCA+RAP	12
Subbase	SG	3.5
Subgrade	Clay	∞

Figure 18. Layer thickness and material information for MnROAD low volume road Cell 189 (MnROAD-LTPP InfoPave system)

Table 9. Arrangement of moisture sensors in Cell 189 and their locations in pavement layers (Cetin et al., 2021)

	EW – Decagon Moisture Sensor			
Sensors:	S101	S102	S103	S104
Depths (in)	5	14	17	20.5
Materials	RCA+RAP	RCA+RAP	SG	Clay
Layer	Base	Base	Subbase	Subgrade
Offset (ft)	-4.7	-4.7	-4.7	-4.7

Note: RCA – Recycled concrete aggregate, RAP-Recycled asphalt pavement, SG- Select granular

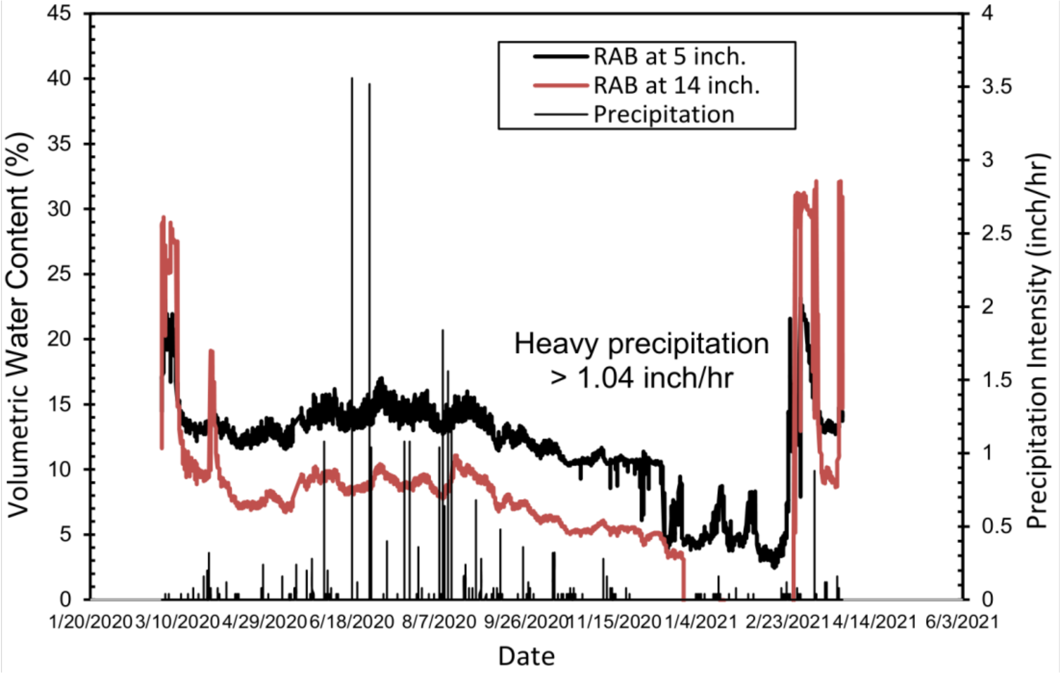

Figure 19. Volumetric moisture content trend of Cell 189 in 2020 for Recycled aggregate base along with precipitation data (collected from TAP member)

2.4 Summary

In summary, the historical precipitation events in the region where the MnROAD facility is located confirm the increasing precipitation trends of the 21st century during the month of heavy precipitation in Minnesota. Since the objective of this study was to check the relationship between heavy precipitation events and the change in the moisture level of pavement foundation layers, a total of 5 test cells were selected based on the availability of moisture data. The Cells of both MnROAD low volume and MnROAD mainline exhibited no consistent trend of volumetric content with a sudden dramatic change of moisture level that might not be attributed to the precipitation trend of the same year. However, after checking the pavement temperature at the exact Cell location, it could be concluded that the early peak volumetric moisture content is associated with the thawing event in that location. The EW-Decagon moisture sensor from other cells of MnROAD low volume road with conventional or recycled base aggregate layer also generated several missing data records that the research team could not use those cells' moisture data. For the MnROAD mainline road cells, while there was an expected change of moisture level due to heavy precipitation events observed for the base, subbase and subgrade layers, the volumetric moisture content of the base layer exhibited variable trends depending on year, cells, and material types. In some cases, EW-Decagon moisture sensor recorded a volumetric moisture content above the maximum possible volumetric water content (as an example, clay loam could hold moisture up to 40% of its total volume). This unexpected high volumetric moisture content could be due to the EW-Decagon moisture sensors' incapability to correctly record data for the comparatively largesized base aggregate or to the faulty calibration equations for the base layers used to convert raw data into volumetric moisture content. Note that while the ISU research team had access to sensor data mostly from 2008 to 2015, it focused on analyzing sensor information between the years 2009 to 2012 since the sensor information between the years 2013 to 2015 had more than 50% missing data points and it was not possible to estimate trends in those years. The ISU research team recently received high-quality moisture data of the base layer from TAP members. These data were collected at Cell 127, Cell 188, and Cell 189 from the MnROAD low-volume road and cured for a period extending from January 2020 to June 2021. Analyzing data from those cells resulted on a consistent trend of base-layer moisture change . In other words, early peak volumetric moisture in March could result from thawing events and in summer heavy precipitation resulted in the peak volumetric moisture content in the base layer. Considering the availability of appropriate data to the ISU research team, Cell 127, Cell 188, and Cell 189 from the MnROAD low-volume road were considered for the next steps of this study.

Chapter 3: Soil Thermal and Hydraulic Properties

3.1 Introduction

M_R is a key input parameter used in pavement design to quantify stiffness of pavement foundations, and moisture-content variation in base aggregate and subgrade soil can significantly affect the M_R value and layer stiffness (Abdollahi & Vahedifard, 2022). The volumetric moisture content of soil depends on both the hydraulic and thermal properties of soil, including hydraulic conductivity, water-retention characteristics, water diffusivity, thermal conductivity, volumetric heat capacity, and thermal diffusivity. Along with moisture change, temperature can also alter microstructural, and engineering properties of unsaturated soil such as volume change, stiffness, and shear strength (Goodman and Vahedifard 2019; Francois and Laloui 2008), so hydraulic and thermal properties play a vital role during moisture movement and vapor flow and are crucial for estimating heavy precipitation effects on pavement-foundation stiffness. For example, soil with higher hydraulic and thermal conductivity will experience greater variation in seasonal moisture content and subsurface temperature (Mahedi et al., 2020). Since hydraulic conductivity depends both on the suction and moisture content of the soil, assessment of soil water characteristics is crucial in determining hydraulic conductivity of soil as a function of moisture content, and there is also a bilinear relationship between thermal conductivity and soil water retention characteristics that exhibits a breaking point at the air entry level (Kim et al. 2015).

This chapter focuses primarily on the cells from the MnROAD low volume road, which was specially built to conduct a comprehensive study on recycled aggregate base and large stone subbase materials. The MnDOT-funded project titled “Determining Pavement Design Criteria for Recycled Aggregate Base and Large Stone Subbase” conducted a comprehensive laboratory and field study of base aggregate and subgrade soil of MnROAD low volume road (Cetin et al. 2021). This study included gradation, proctor and gyratory compaction, specific gravity, absorption, hydraulic conductivity, the soil-water characteristic curve, and water repellency/contact angle. The laboratory test results required for quantifying heavy-precipitation effects on pavement foundations are summarized in this report. These results are used to model moisture response to precipitation and subsurface temperature changes. The responses of the developed model are used to predict the M_R of soil and aggregate at the corresponding moisture content from the extended version of the MEPDG equation (Zapata et al., 2007). This chapter Identifies the available material properties required for developing a prediction model for base-layer saturation.

3.2 Available Material Properties

Since this research is focused on using Cell 127, Cell 188, and 189 to develop a model for the prediction of moisture and corresponding stiffness of pavement foundation, the available material properties from the recently completed National Road Research Alliance (NRRA)-funded study were utilized to develop and validate the prediction models (Cetin et al. 2021). Most of the necessary material properties available from a previous research study are documented in the section.

3.2.1 Cell 127, Cell 188, and Cell 189

The structure of Cell127, shown in **Figure 20,** is comprised of a 3.5-inch HMA layer, a 6-inch Class 6 base aggregate, and an 18-inch large stone subbase (LSSB) atop the clay subgrade. Three EW-Decagon moisture sensors were embedded in this cell at different depths: one in the base layer and two in the subgrade layer. A total of 12 thermocouples embedded at varying pavement depths collect seasonal temperature variation. **Figure 21** shows the layer structure of Cell 188: a 3.5-inch HMA layer, a 12-inch limestone aggregate layer, a 3.5-inch select granular subbase, and clay subgrade soils. Cell 188 contains four moisture sensors and twelve thermocouples embedded at different depths. Cell 127 and Cell 188 were constructed with conventional class 6 base aggregate, while the base layer of Cell 189 was built with recycled aggregate comprised of recycled asphalt concrete and recycled asphalt pavement. The structural components, along with locations of the thermocouples and moisture sensor, are shown in **Figure 22**.

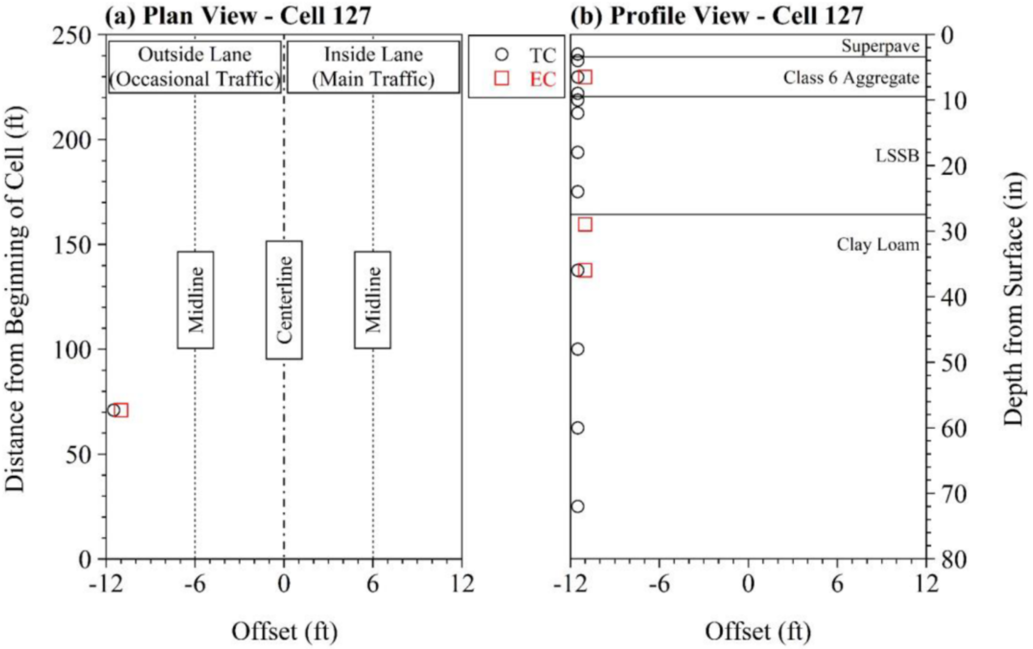

Figure 20. Plan view and layered structure of Cell 127, including the location of the thermocouple and moisture probe (Cetin et al. 2021)

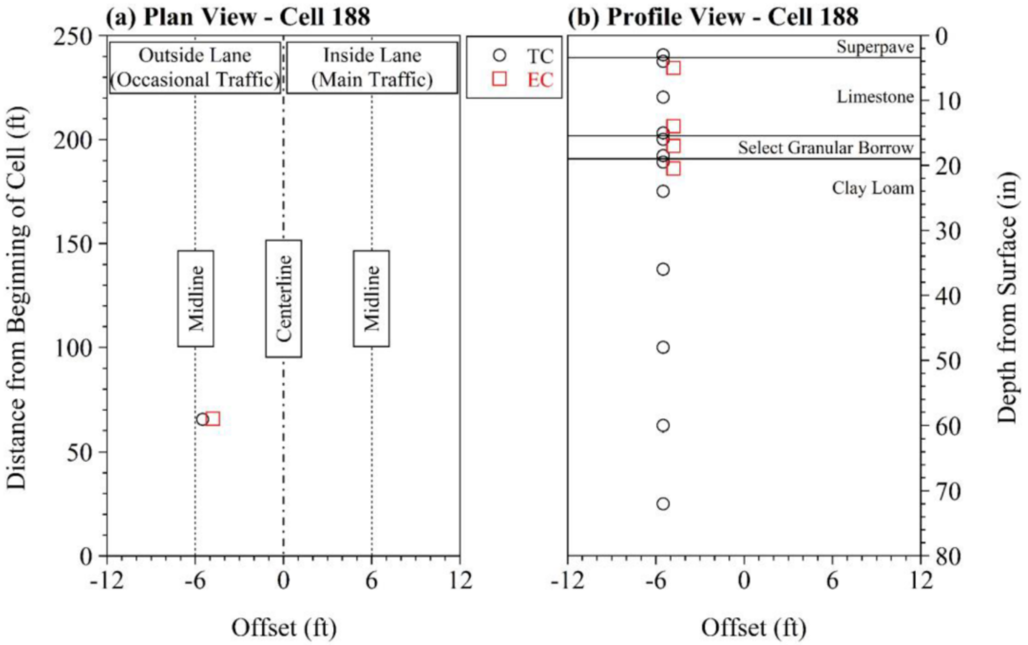

Figure 21. Plan view and layered structure of Cell 188, including the location of the thermocouple and moisture probe (Cetin et al. 2021)

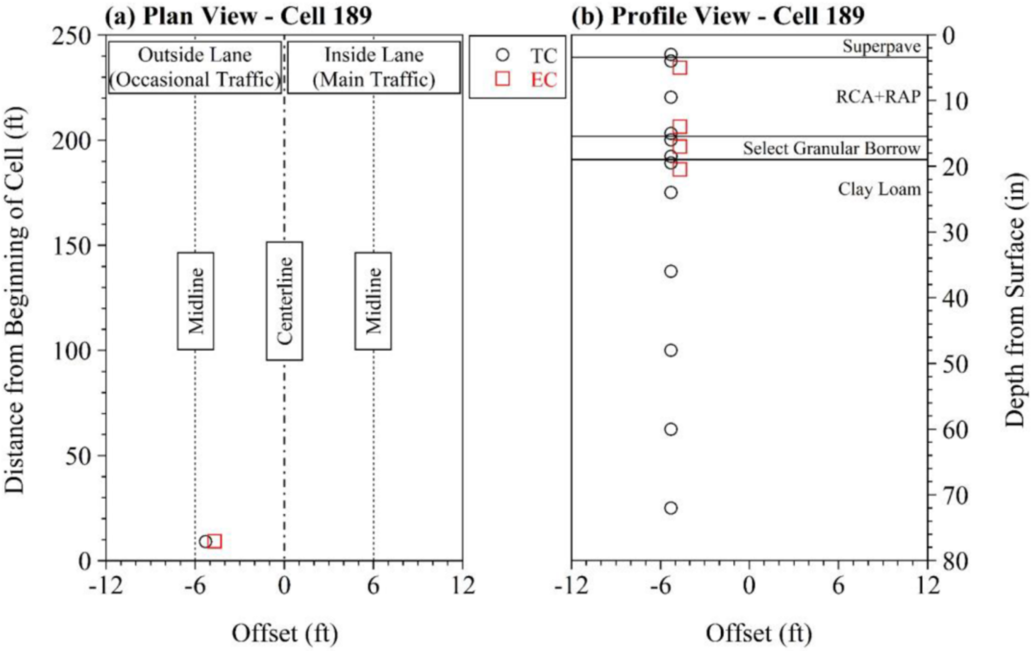

Figure 22. Plan view and layered structure of Cell 189, including the location of the thermocouple and moisture probe (Cetin et al. 2021)

3.2.2 Index Properties of Soil and Aggregates

This section summarizes the index properties of soil and aggregates of Cell 127, Cell 188, and Cell189, including particle-size distribution, Atterberg limits, Proctor compaction, specific gravity, and binder content; Cetin et al. (2021) determined these index properties at a Michigan State University laboratory. The particle size distribution of both soil and aggregate was determined by following the ASTM C136, ASTM D6913, and ASTM D7928 standard specifications. The liquid limit and plasticity index of materials were measured in accordance with ASTM D4318 specification, after which they were classified according to the Unified Soil Classification System (USCS) and the American Association of State Highway and Transportation Officials (AASHTO) soil classification system. **Table 10** shows the index properties of base aggregates and subgrade soils, along with the classification of materials. Class 6 Aggregate, limestone and RCA+RAP, LSSB, Select Granular Borrow, and clay loam were, according to USCS, respectively classified as SP-SM (poorly-graded sand with silt and gravel), GM (silty gravel with sand), SP-SM (poorly-graded sand with silt and gravel), GP (poorly graded gravel), SM (silty sand with gravel) and CL (sandy lean clay). Moisture-density relationships of materials were determined by following ASTM D1557, with Method C used for Class 6 Aggregate, limestone, and RCA+RAP, and Method A followed for clay loam subgrade soil. It was not possible to measure the moisture-density relationship for the LSSB material because of the large particle size. The maximum dry density (MDD) and optimum moisture content (OMC) of materials were determined from the moisture density relationships. The MDD and OMC values of the materials are listed in **Table 11.**

Table 10. List of index properties and soil classification (Cetin et al. 2021)

Materials	LL	PI	Gravel (%)	Sand (%)	Fines (%)	C_u	C_c	Classification	
								USCS	AASHTO
Class 6 Aggregate	27.4	NP	35.1	58.6	6.3	23.82	0.60	SP-SM	A-1-a
Limestone	17.9	NP	52.3	32.6	15.1	211.3	1.91	GM	A-1-b
RCA+RAP	27.4	NP	41.0	50.4	8.6	49.41	0.98	SP-SM	A-1-a
LSSB	NA	NP	99.6	0.3	0.1	1.84	1.08	GP	A-1-a
Select Granular Borrow	18.9	NP	31.1	56.5	12.4	30.30	1.10	SM	A-1-b
Clay Loam	36.3	12.4	3.1	37.2	59.7	NA	NA	CL	A-6

* LL – liquid limit, PI – plasticity index, C_u – coefficient of uniformity, C_c – coefficient of curvature

Cetin et al. (2021) calculated material's specific gravity and absorption per ASTM C127 and ASTM C128. The specific gravity includes over-dry specific gravity, saturated surface dry specific gravity, and apparent specific gravity for all materials except clay loam; ASTM D854 was followed to measure the apparent specific gravity of clay loam. Cetin et al. (2021) was unable to determine absorption for clay loam because ASTM D854 provides no standard procedure for measuring the absorption of clay loam. **Table 11** shows the results of the specific gravity and absorption tests.

Table 11. Results of proctor compaction and specific gravity of materials (Cetin et al. 2021)

Materials	OD-G_s	SSD-G_s	Apparent G_s	Absorption (%)	Proctor Compaction	
					MDD (lb/ft3)	OMC (%)
Class 6 Aggregate	2.35	2.44	2.58	3.86	128.5	8.3
Limestone	2.66	2.71	2.79	1.72	143.2	6.3
RCA+RAP	2.28	2.38	2.52	4.34	125.8	10.0
LSSB	2.60	2.61	2.63	0.36	NA	NA
Select Granular Borrow	2.62	2.66	2.72	1.53	140.3	5.3
Clay Loam	NA	NA	2.68	NA	124.9	10.0

* G_s – specific gravity, OD – oven dry, SSD – saturated surface dry, MDD – maximum dry density, and OMC – optimum moisture content

The asphalt binder content of Class 6 Aggregate, l, and RCA+RAP was determined by the ignition method and the quantitative extraction method listed in ASTM D6307 and AASHTO T308. Class 6 Aggregate and RCA+RAP exhibited higher asphalt binder content compared to limestone, 3.17% and 3.18%, according to the ignition method. The residual mortar content of Class 6 Aggregate, limestone, and RCA+RAP was measured based on a technique described by Abbas et al. (2007). A total of 6,000 gm of each material was collected to determine residual cement content, including 2,000 gm of particles retained on a 1-inch sieve, 2,000 gm of particles retained on a 3/4-inch sieve, 1,000 gm of particles retained on a 3/8-inch sieve, and 1,000 gm of particles retained on a No.4 sieve. The collected samples were oven-dried at 105°C for 24 hr. immersed in sodium sulfate solution for 24 hr, then subjected to five freeze-thaw cycles with freezing at -17°C for 16 hr. and thawing at 80°C for eight hr. Disintegrated mortar and aggregate were then washed over the No.4 sieve, and residual mortar content was estimated. The asphalt binder and residual mortar content values found for Class 6 Aggregate, limestone, and RCA+RAP are listed in **Table 12** (Cetin et al. 2021).

Table 12. Asphalt binder and residual cement mortar content of materials (Cetin et al. 2021)

Materials	% Asphalt Binder Content		% Residual Mortar Content
	Ignition Method	Quantitative Extraction Method	
Class 6 Aggregate	3.17	1.77	25.6
Limestone	1.61	0.35	1.3
RCA+RAP	3.18	1.58	20.1
LSSB	NA	NA	NA
Select Granular Borrow	NA	NA	NA
Clay Loam	NA	NA	NA

3.2.3 Hydraulic Properties of Soil and Aggregates

Knowledge of soil water characteristics describing the relationship between volumetric water content (VWC) and soil matric suction is vital in characterizing a soil's hydraulic properties. In Geotechnical engineering practice, the soil water characteristic curve (SWCC) acts as a bridge to the implementation of unsaturated soil mechanics. A typical SWCC consists of two curves: the wetting curve and the drying curve. The difference between matric suction on these curves is described as a hysteresis phenomenon that affects the unsaturated hydraulic properties of soil (Likos et al., 2013). Figure 23 illustrates typical soil wetting and drying curves. Since it's often difficult to measure a soil wetting curve, using the drying curve is often recommended for estimating the hydraulic behavior of soils (Nokkaew et al. 2012). Cetin et al. (2021) determined the drying SWCC for soil and aggregates shown in this section. To measure the volumetric moisture content at different suction values, hanging-column tests were conducted for Class 6 Aggregate, while pressure plate and activity meter tests were considered for limestone, RCA+RAP, and clay loam. The hanging-column tests applied a suction of up to about 6 psi, while pressure plates were used to apply much higher suction values, up to 220 psi, and the high suction values were applied to specimens to determine their residual moisture content. The SWCC curve was plotted by fitting the laboratory test data to the van Genuchten model (van Genuchten 1980). Equation (1) shows the van Genuchten model commonly used to define soil water potential and moisture content relationships.

$$\frac{\theta-\theta_r}{\theta_s-\theta_r} = \left[\frac{1}{1+(\alpha h)^n}\right]^m \qquad (1)$$

Where θ is the normalized volumetric water content, θ_r is the residual volumetric water content, θ_s is saturated volumetric water content, and m and n are model parameters. **Figure 24** shows the relationship between suction and volumetric moisture content for Class 6 Aggregate and the van Genuchten model-fitted SWCC. The SWCC values for limestone, RCA+RAP, and clay loam determined by activity meter and pressure plate tests are shown in **Figure 25**, **Figure 26,** and **Figure 27,** respectively.

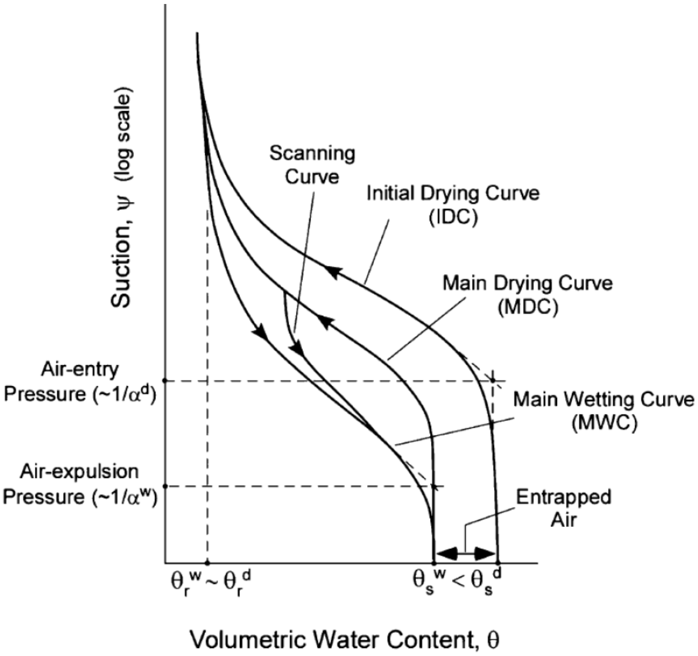

Figure 23. Illustration of typical soil water characteristics with drying, wetting curve and hysteretic behavior of soil (Likos et al. 2013)

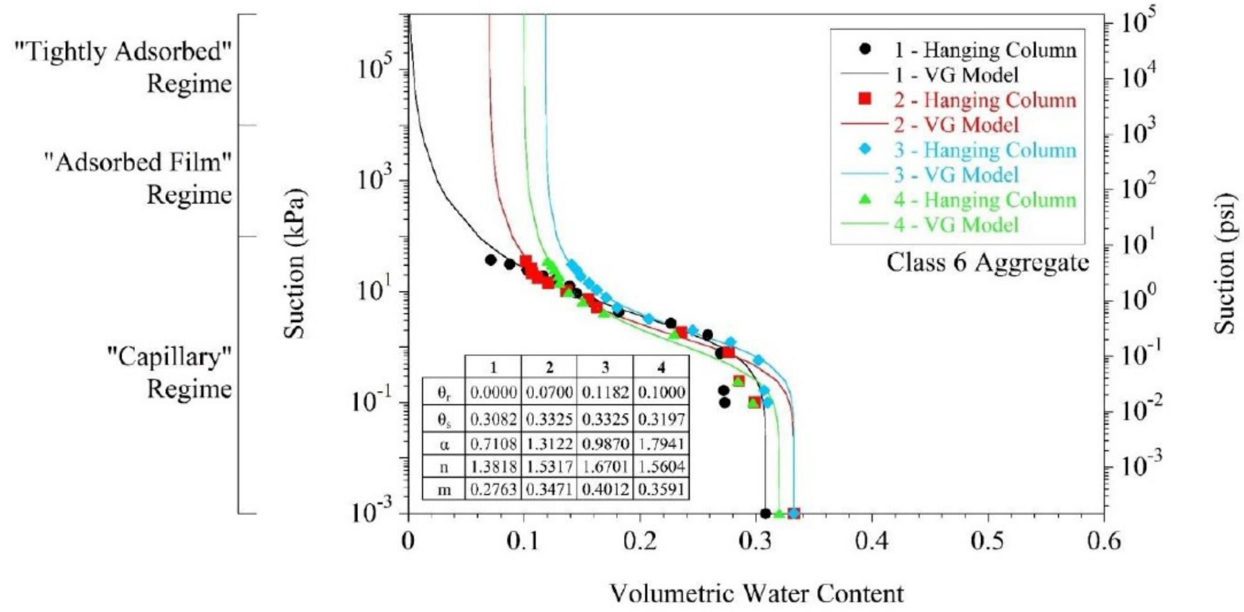

	1	2	3	4
θ_r	0.0000	0.0700	0.1182	0.1000
θ_s	0.3082	0.3325	0.3325	0.3197
α	0.7108	1.3122	0.9870	1.7941
n	1.3818	1.5317	1.6701	1.5604
m	0.2763	0.3471	0.4012	0.3591

Figure 24. Soil water characteristics curve for Class 6 aggregate at optimum compaction condition by hanging column test (Cetin et al. 2021)

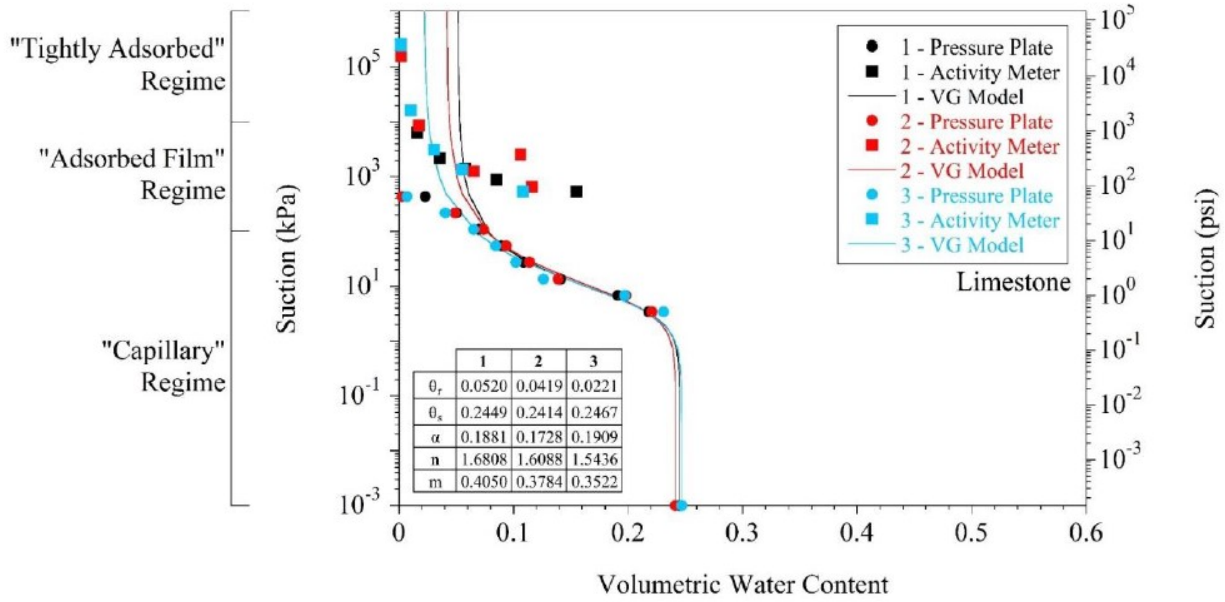

	1	2	3
θ_r	0.0520	0.0419	0.0221
θ_s	0.2449	0.2414	0.2467
α	0.1881	0.1728	0.1909
n	1.6808	1.6088	1.5436
m	0.4050	0.3784	0.3522

Figure 25. Soil water characteristics curve for limestone at optimum compaction condition by activity meter and pressure plate tests (Cetin et al. 2021)

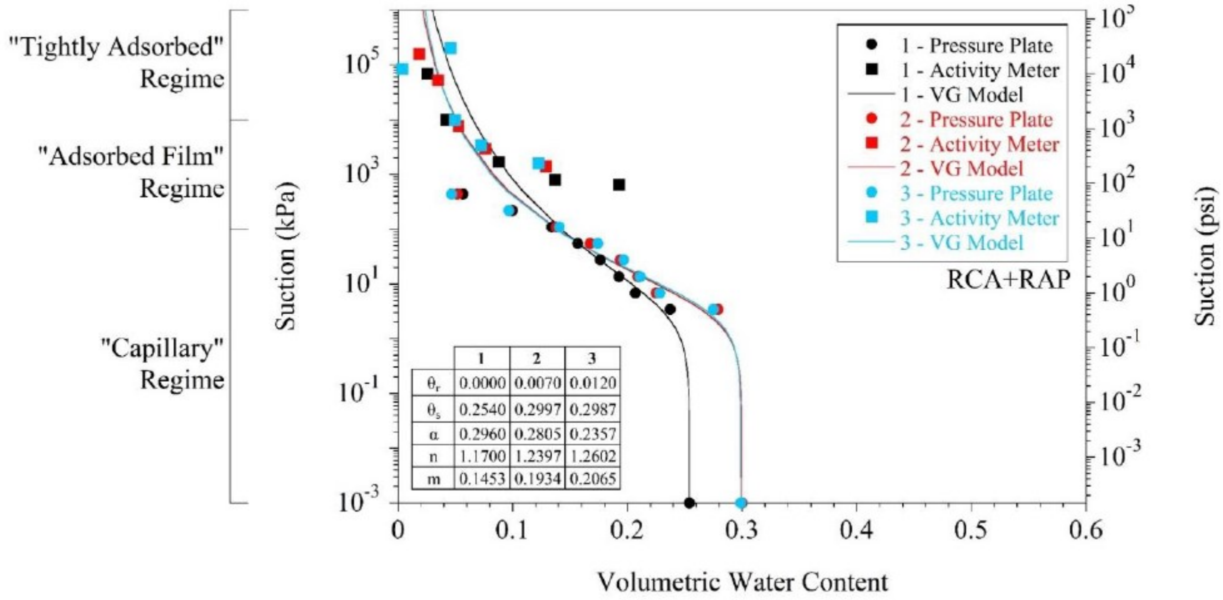

	1	2	3
θ_r	0.0000	0.0070	0.0120
θ_s	0.2540	0.2997	0.2987
α	0.2960	0.2805	0.2357
n	1.1700	1.2397	1.2602
m	0.1453	0.1934	0.2065

Figure 26. Soil water characteristics curve for RCA + RAP at optimum compaction condition by activity meter and pressure plate tests (Cetin et al. 2021)

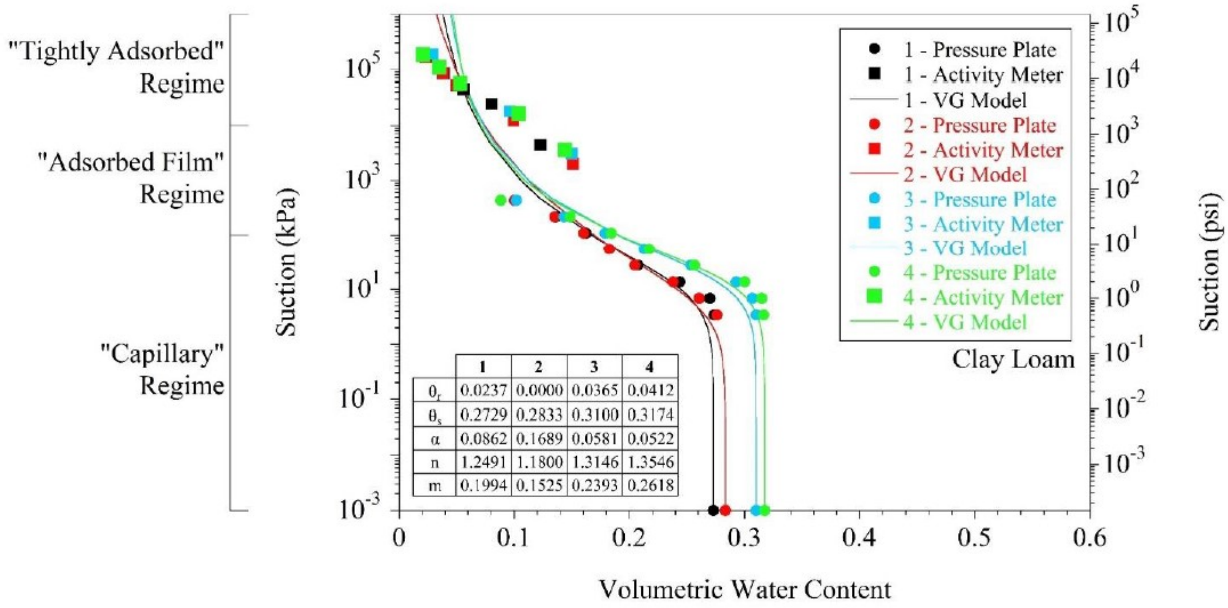

	1	2	3	4
θ_r	0.0237	0.0000	0.0365	0.0412
θ_s	0.2729	0.2833	0.3100	0.3174
α	0.0862	0.1689	0.0581	0.0522
n	1.2491	1.1800	1.3146	1.3546
m	0.1994	0.1525	0.2393	0.2618

Figure 27. Soil water characteristics curve for clay loam at optimum compaction condition by activity meter and pressure plate tests (Cetin et al. 2021)

Saturated volumetric water content, air-entry pressure, and van Genuchten Model Parameters for Class 6 Aggregate, limestone, RCA+RAP, and clay loam are listed in **Table 13**. The air-entry pressure is defined as the suction pressure at which air begins to penetrate the soil.

Table 13. Saturated volumetric water content, pressures at the air-entry level, and van Genuchten Model Parameters (Cetin et al. 2021)

Materials	Initial VWC	Air-entry Pressure		van Genuchten Model Parameters				
		kPa	psi	θ_r	θ_s	α	n	m
Class 6 Aggregate	0.323	0.30	0.04	0.070	0.333	1.312	1.532	0.347
Limestone	0.244	1.75	0.25	0.022	0.247	0.173	1.609	0.378
RCA+RAP	0.284	1.40	0.20	0.012	0.299	0.236	1.260	0.207
LSSB	NA	NA	NA	NA	NA	NA	NA	NA
Select Granular Borrow	NA	NA	NA	NA	NA	NA	NA	NA
Clay Loam	0.296	3.50	0.51	0.041	0.317	0.052	1.355	0.262

The saturated hydraulic conductivity of materials was determined by both constant-head and falling-head permeability tests (Cetin et al., 2021). ASTM D5084 method A was followed to measure saturated hydraulic conductivity using a constant head permeability test most suitable for coarse materials, while falling-head permeability tests were carried out on both coarse and fine materials in accordance with ASTM D5084 method C. The specimens were prepared at various degrees of saturation to estimate the effect of the degree of saturation on the saturated hydraulic conductivity of soils and aggregates. It was not possible to prepare specimens of LSSB and Select Granular Materials for measuring saturated hydraulic conductivity because of mold-size limitations. The saturated hydraulic conductivity (K_{sat}) was calculated by Darcy's law after collecting the volume of water passing through a test specimen over time. For the falling-head permeability tests, specimens were prepared at 100%, 95%, and 90% degrees of saturation. The results from both the constant-head and falling-head permeability tests are shown in

Table 14**.** As expected, K_{sat} decreased with a higher degree of compaction for both aggregates and soils, and hydraulic conductivity changed as a function of the soil's suction and moisture content. Mualem (1976) suggested Equation (2) for calculating moisture-dependent hydraulic conductivity at each soil layer.

$$K(\theta) = K_{sat} \left(\frac{\theta-\theta_r}{\theta_s-\theta_r}\right)^{1/2} \left[\int_0^{\frac{\theta-\theta_r}{\theta_s-\theta_r}} \frac{\delta z}{h(z)} \Big/ \int_0^1 \frac{\delta z}{h(z)}\right]^2 \tag{2}$$

where K_{sat} is the hydraulic conductive conductivity when soil is fully saturated, z is the depth of soil in cm, h is the matric suction, θ is the volumetric water content, θ_r is residual volumetric water content, and θ_s is the saturated volumetric water content.

Table 14. Saturated hydraulic conductivity of materials by both constant head and falling head permeability tests (Cetin et al. 2021)

Materials	Constant Head Permeability K_{sat} (in/sec)	Falling Head Permeability K_{sat} (in/sec)		
	$DC_{var.}$	DC_{100}	DC_{95}	DC_{90}
Class 6 Aggregate	2.07×10^{-3} - 9.41×10^{-3}	8.5×10^{-5}	2.0×10^{-4}	6.18×10^{-4}
Limestone	1.70×10^{-4} - 9.41×10^{-3}	3.17×10^{-5}	7.52×10^{-5}	1.29×10^{-4}
RCA+RAP	3.35×10^{-5} - 6.57×10^{-3}	4.50×10^{-4}	1.89×10^{-4}	4.90×10^{-4}
LSSB	NA	NA	NA	NA
Select Granular Borrow	NA	NA	NA	NA
Clay Loam	NA	5.39×10^{-8}	5.94×10^{-7}	2.70×10^{-6}

* DC_{100} – 100% degree of saturation, DC_{95} – 95% degree of saturation, DC_{90} – 90% degree of saturation, and $DC_{var.}$ – Variable degree of saturation

3.2.4 Thermal Properties of Soil and Aggregates

A soil's thermal properties, crucial to the vapor flow estimation in the soil layer, are affected by the volumetric moisture content of the soil (Mahedi et al. 2020). This study focused on measuring the three main thermal properties of soil: thermal conductivity (λ), volumetric heat capacity (C), and thermal diffusivity (α). Thermal conductivity (λ) of soil is defined as a soil's capability for conducting heat; it depends on the bulk density and moisture content of soil. Soil volumetric heat capacity (C) is defined as the amount of energy required to raise the temperature of a unit volume of soil by one degree. The ratio of thermal conductivity (λ) to soil volumetric heat capacity (C) is defined as the thermal diffusivity (α) of soil. Decagon KD2 Pro software was utilized in this study for laboratory measurement of thermal conductivity (λ), volumetric heat capacity (C), and thermal diffusivity (α) of soils. In addition to laboratory testing, temperature profiles collected from thermocouples at different soil-layer depths could be used for measuring the thermal diffusivity (α) of soil. Cetin et al. (2021) estimated the thermal diffusivity of soil from temperature-sensor-recorded data with the help of amplitude and phase equations; Equation (3) is the amplitude equation, and Equation (4) is the phase equation for estimating thermal diffusivity of soils.

$$\alpha = \frac{\omega}{2}\left[\frac{z_2 - z_1}{ln\left(\frac{A_1}{A_2}\right)}\right]^2 \tag{3}$$

$$\alpha = \frac{1}{2\omega}\left[\frac{z_2 - z_1}{\Delta t_{max}}\right]^2 \tag{4}$$

where radial frequency $\omega = \frac{2\pi}{p}$; p is the period, $z_1$and z_2 are the two depths where temperature data were recorded, $A_1$and A_2 are the measured amplitude/maximum temperature at depths $z_1$and z_2, and Δt_{max} is the time difference between these maximum temperatures. **Figure 28** shows the thermal diffusivity estimated from the phase equation for limestone in Cell 188. The thermal diffusivity for RCA+RAP and LSSB materials was calculated using the phase equation at a different periods of the year, as shown in **Figure 29** and **Figure 30**.

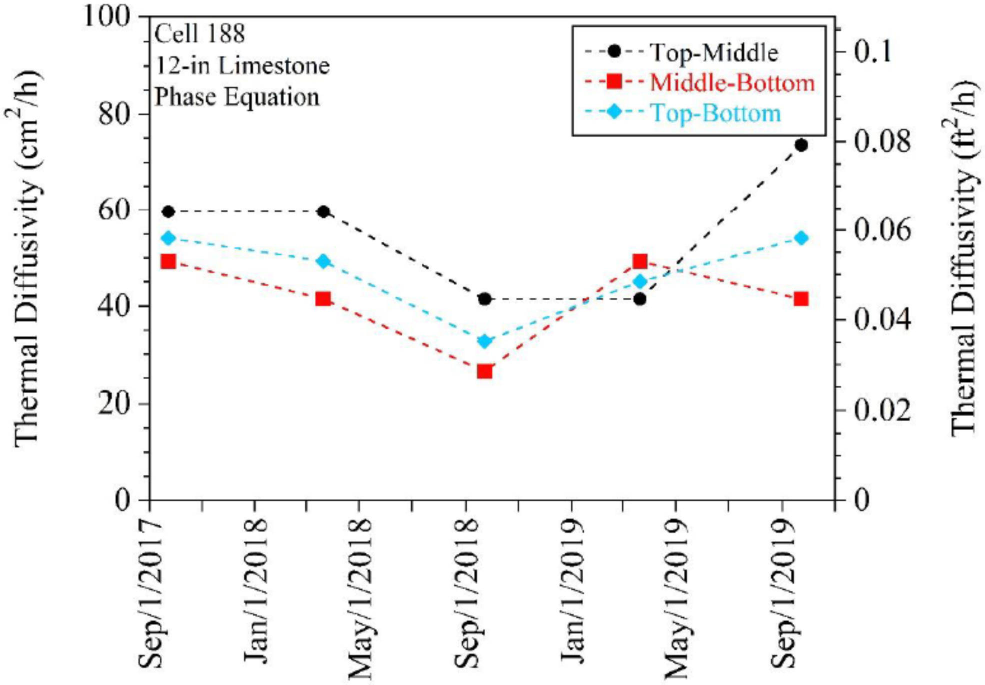

Figure 28. Thermal diffusivity of limestone in Cell188 estimated by phase equation (Cetin et al. 2021)

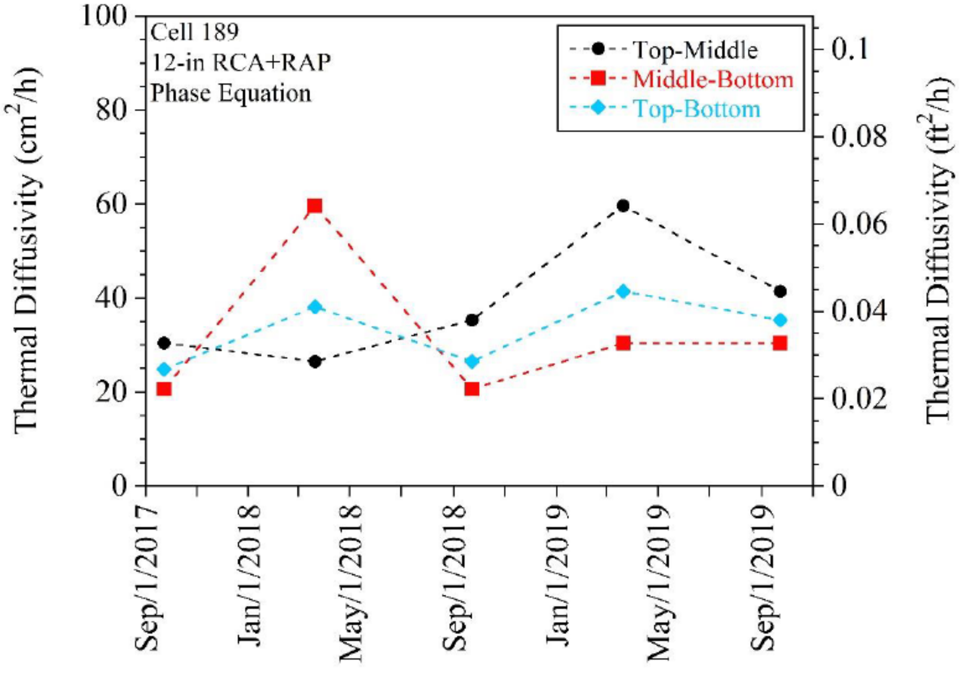

Figure 29. Thermal diffusivity of RCA + RAP in Cell189 estimated by phase equation (Cetin et al. 2021)

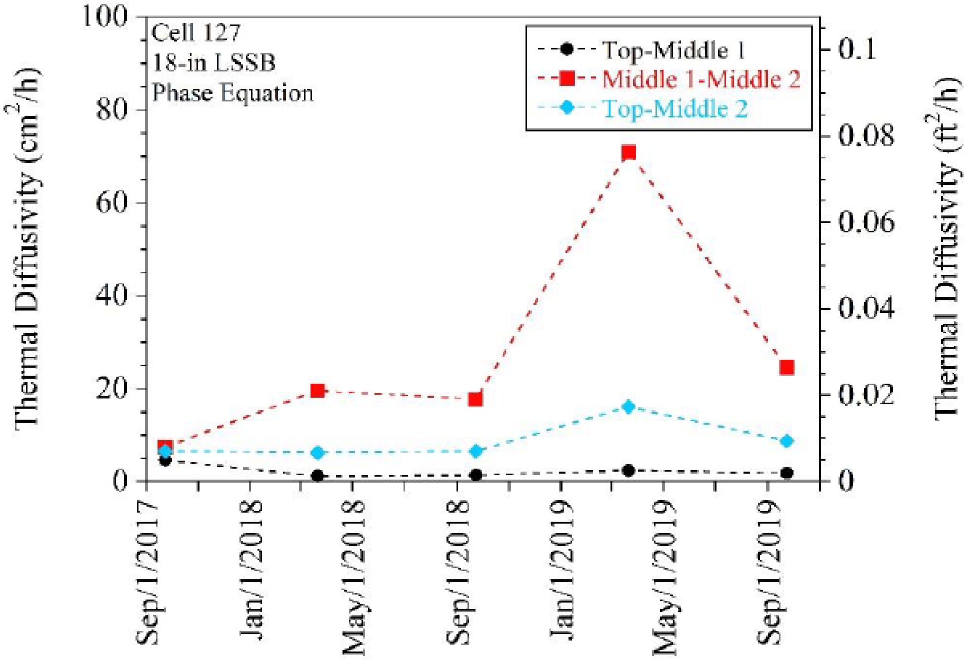

Figure 30. Thermal diffusivity of LSSB in Cell127 estimated by phase equation (Cetin et al. 2021)

3.3 Summary

Since most of the material properties of cells selected for this study are available in the report of a completed NRRA-funded project (Cetin et al. 2021), Technical Advisory Panel (TAP) agreed to collect available material information from the literature and MnROAD database and utilize those properties for developing moisture and heat-transfer models for the materials. Cell 127, Cell 188, and Cell 189 were comprised of different types of base aggregate, including both conventional and recycled base aggregate. This chapter summarizes index properties, hydraulic and thermal properties of base aggregate and clay loam subgrade soils. To help explain the hydraulic and thermal behavior, index properties of materials, such as particle size distribution, unit weight, moisture content, and specific gravity, are listed in this report. The saturated hydraulic-conductivity and soil-water characteristic curves for Class 6 Aggregate, limestone, RCA+RAP, and clay loam are documented in this report to provide necessary input for coupled-flow deformation analysis. The hydraulic properties of the material were utilized to determine the water flux of the layer and the moisture content resulting from heavy precipitation. Note that hydraulic properties for LSSB and Select Granular Borrow materials were not available in the previous study because of limitations of equipment needed to carry out permeability and soil water characteristics tests on a large-size aggregate specimen. Thermal diffusivity as the only thermal property of base aggregate was obtained from a MnDOT study (Cetin et al., 2021) in which field temperature data from thermocouples located at different depths within the layer were used to estimate thermal-diffusivity values of base aggregate.

Chapter 4: Plaxis 3D Hydraulic Modeling

4.1 Introduction

Heavy precipitation-related increased moisture content in pavement foundation layers could reduce the stiffness and strength of pavement foundations, resulting in surface deflection and cracking. The reduced stiffness of the pavement foundation could be quantified by determining reduction of the M_R of the corresponding layers. One of the most important variables that affect overall stiffness of pavement system is the M_R of the foundation layers. Several studies have been conducted to assess the effect of moisture content on the resilient properties of unbound materials subjected to repeated traffic loading (Zapata et al. 2007, Witczak et al. 2000, Drumm et al. 1997, Li and Selig 1994), and the robust modulus corresponding to the layer saturation level was predicted using the MEPDG equation (Zapata et al., 2007). Equation (5) is the MEPDG equation for predicting the degree of saturation-dependent M_R values.

$$log\frac{M_R}{M_{R-OPT}} = a + \frac{b-a}{1+\exp[\ln\left(-\frac{b}{a}\right)+K_m(S-S_{OPT})]} \tag{5}$$

where S_{OPT} is the degree of saturation at optimal moisture content, M_R is the resilient modulus at a given degree of saturation, $M_{R\text{-}OPT}$ is the resilient modulus at optimum moisture content, a is the minimum of log ($M_R/M_{R\text{-}OPT}$), b is the maximum of log-log ($M_R/M_{R\text{-}OPT}$), and k_m is a regression parameter.

A two-step modeling approach was adopted in this study to account for changes in subsurface moisture due to heavy rain and to analyze the vulnerability of pavement foundations to such moisture change. The first step was predicting change in moisture due to heavy rainfall, followed by the second step predicting the corresponding M_R from Equation (5).

The partial differential equation shown in Equation (6) describes one-dimensional vertical water movement that depends on water potential (Richards 1931). But, it does not have any analytical solution.

$$\frac{\partial\theta}{\partial t} = \frac{\partial}{\partial z}\left[k(\theta)\left(\frac{\partial h}{\partial z} - 1\right)\right] \tag{6}$$

where θ is the volumetric water content (m^3/m^3), K(θ) is the hydraulic conductivity of pavement materials (m/day), z is the depth (m), and h is the water potential in m, also a function of volumetric moisture content (via the soil water characteristic curve, SWCC).

Hydraulic conductivity also changes as a function of moisture content, leading to a convoluted relationship between moisture content, water potential, and hydraulic conductivity. In developing a numerical solution, van Genuchten (1980) developed the relationship between water potential and moisture change shown in Equation (7) which led to the development of the numerical solution for a one-dimensional vertical water movement equation shown in Equation (6):

$$S(\emptyset_p) = S_r + \ (S_s - S_r)\left[1 + (g_a/\emptyset_p)^{g_n}\right]^{g_c} \tag{7}$$

where $S(\emptyset_p)$ is saturation corresponding to matric suction $\emptyset_p$, S_r is residual saturation related to remaining water content even at high suction, and S_s is saturation when the pore is filled with water. Model parameters g_c, g_a and g_n are obtained by fitting soil/water characteristic curves.

Mualem (1976) suggested using the relationship shown in Equation (8) to find the moisture-dependent hydraulic conductivity of porous media.

$$K_{rel}(S) = (S_e)^{g_l}\left[1 - (1 - \ S_e^{\frac{g_n}{g_{n-1}}})^{\frac{g_{n-1}}{g_n}}\right]^2 \tag{8}$$

where $K_{rel}(S)$ is the hydraulic conductivity corresponding to saturation level, g_l is an empirical parameter, and S_e is the effective saturation defined as $S_e = \frac{S - S_r}{S_s - S_r}$.

Precipitation intensity and duration were considered as boundary conditions in the modeling steps, while *in-situ* moisture contents defined the initial boundary condition. The estimated moisture content and saturation in the foundation layer were then used in Equation (5) to assess the corresponding stiffness of the foundation materials. This chapter describes PLAXIS 3D model development used to simulate the moisture flux due to heavy rainfall at the base layer of Cell 127, Cell 188, and Cell 189.

PLAXIS 3D is a finite-element analysis tool with the capability to consider the hydraulic behavior of unsaturated/saturated soils or any other porous media. The hydraulic model in the undrained analysis scheme of PLAXIS 3D uses the van Genuchten (1980) model that provides a relationship between saturation and suction (i.e., negative pore pressure). Equation (7) depicts the van Genuchten relationship. PLAXIS 3D uses the Mualem (1976) relationship shown in Equation (8) to define the relative permeability of soil depending on the saturation. The water flux simulation in pavement layers was conducted using PLAXIS 3D coupled flow-deformation analysis and unsaturated soil mechanics. PLAXIS 3D software utilizes Biot's theory shown in Equation (9) that includes both the continuity and equilibrium equation of the water-soil structure for simulating coupled behavior of soil (Biot 1941). The formulation is based on Bishop's effective stress and Darcy's law for fluid flow.

$$\sigma = \ \sigma' + m(\varkappa P_w + (1 - \varkappa)P_a \tag{9}$$

where σ is total stress, σ' is effective stress, P_w is pore water pressure, P_a is pore air pressure, $\varkappa$ is an effective stress parameter called matric suction coefficients and varies from 0 to 1 covering the range from dry to fully saturated conditions, and m is a vector containing unity terms for normal stress component.

4.2 Cell 188

The structure of Cell 188 is comprised of a 3.5 in Hot Mix Asphalt (HMA) layer, a 12 in limestone base aggregate, a 3.5-inch select granular (SG) subbase, and clay subgrade soils. This structure was created in PLAXIS 3D with model dimensions of 32 ft width and 16 ft length. The model for Cell 188 showing each layer dimension and the location of the groundwater table is shown in **Figure 31**.

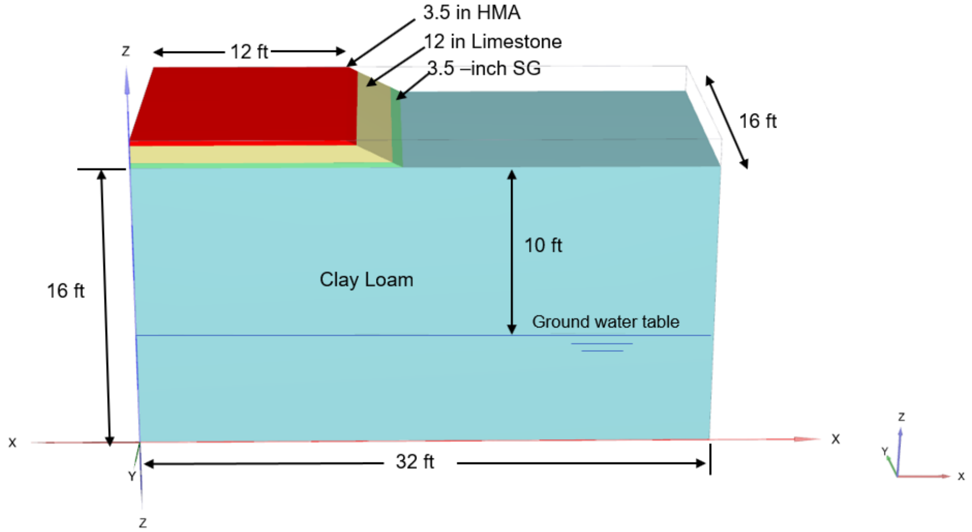

Figure 31. PLAXIS 3D model with the dimensions of each layer for the Cell 188 structure

The key material properties for PLAXIS 3D hydraulic modeling dealing with unsaturated soil behavior are parameters related to soil/water characteristic curves and saturated hydraulic conductivity of the materials, along with other material properties that include soil index and engineering properties. Cetin et al. (2021) conducted an extensive laboratory investigation on the base, subbase, and subgrade materials collected from Cell 188 that included index properties, hydraulic properties (including soil water characteristic curve (SWCC)) and engineering properties. In this study, these material properties were also considered for PLAXIS 3D modeling, although the soil water characteristics and hydraulic conductivity for asphalt concrete were not available from that earlier study. A study from New Mexico University, where Pease (2010) conducted a hydraulics conductivity test on asphalt concrete collected from the MnROAD facility, was consulted for reference properties for asphalt concrete. Van Genuchten parameters for the asphalt concrete were also collected from that study at New Mexico University (Pease 2010). The input material properties for the PLAXIS 3D model of the Cell 188 structure are listed in Table 15. Note that the van Genuchten parameter for select granular materials was finalized based on the output results of PLAXIS 3D models. These parameters were changed and finalized after comparing PLAXIS 3D-generated saturation data with saturation data collected from sensors installed at Cell 188. After trial and error, the van Genuchten model parameters for select granular material shown in Table 15 were finalized for this study.

Table 15. List of material properties for Cell 188 (Cetin et al. 2021 and Pease 2010)

Parameter	Symbol	Asphalt Concrete	Limestone Aggregate	Select Granular	Clay Loam	Unit
General						
Soil model		Linear elastic	Linear elastic	Linear elastic	Linear elastic	
Unsaturated unit weight	γ_{unsat}	145	127	120	115	lb/ft^3
Saturated unit weight	γ_{sat}	152	145	135	125	lb/ft^3
Initial void	e_{init}	0.07	0.25	0.40	0.32	
Mechanical						
Stiffness	E'_{ref}	200	29.0	21.8	10.0	ksi
Poisson's ratio	ϑ	0.3	0.35	0.35	0.35	
Groundwater						
van Genuchten model parameters	S_{res}	0.01	0.089	0.028	0.13	
	S_{sat}	1.0	1.0	1.0	1.0	
	g_n	8.320	3.50	1.93	2.8	
	g_a	1.677	2.64	4.52	3.82	
	g_l	0.15	-0.25	-0.36	1.2	
Hydraulic conductivity	K_x	0.002	0.919	4.10	0.26	in/hr
	K_y	0.002	0.919	4.10	0.26	in/hr
	K_z	0.002	0.919	4.10	0.26	in/hr

The rainfall scenario for May 2020 was created in PLAXIS for the simulation with a saturation value of 25% was assumed as an initial boundary condition in the finite-element analysis. During rainfall simulation in PLAXIS 3D, no ponding water scenario was considered; it was assumed that extra water after infiltration would be runoff from the asphalt concrete surface. In PLAXIS 3D, rainfall-induced infiltration was created by considering a time-dependent precipitation scheme. PLAXIS 3D has capability for creating time-dependent rainfall scenarios based on rainfall information from the MnROAD facility. **Figure 32 (a**) shows the rainfall information that was collected from onsite weather station at the MnROAD facility in 2020, and **Figure 32 (b**) shows the rainfall scenario created in PLAXIS 3D which represents rainfall at the MnROAD facility in May 2020. The saturation of the pavement layers due to the rainfall scenario created in PLAXIS 3D is shown in **Figure 32 (c)**, with the computed saturation at 5 in and 14 in of the base layer computed in **Figure 32 (d)**. These two depths were considered for performing model calibration by comparing the saturation data obtained from two Decagon moisture sensors installed at the same depths in Cell 188 at the limestone aggregate base layer to obtain the volumetric moisture content. The MnDOT staff developed material-specific calibration equations for converting dielectric constant values obtained from Decagon's moisture sensor to volumetric moisture content (Cetin et al. 2021). The saturation of limestone aggregate was computed by taking the ratio of volumetric water content to the void present in limestone aggregate estimated from the SWCC curve of the limestone aggregate (Cetin et al. 2021). The maximum saturation obtained from the field sensor at depth 14 in the base layer was 49.6%, while PLAXIS 3D simulation produces a maximum saturation of 49.7% at the same depth. At a depth of 5 in, the simulated saturation was 40%, while the sensor-measured maximum saturation was 31% in May 2020. **Figure 32 (e)** shows the variation of saturation measured from sensor and rainfall data at the same location in May 2020.

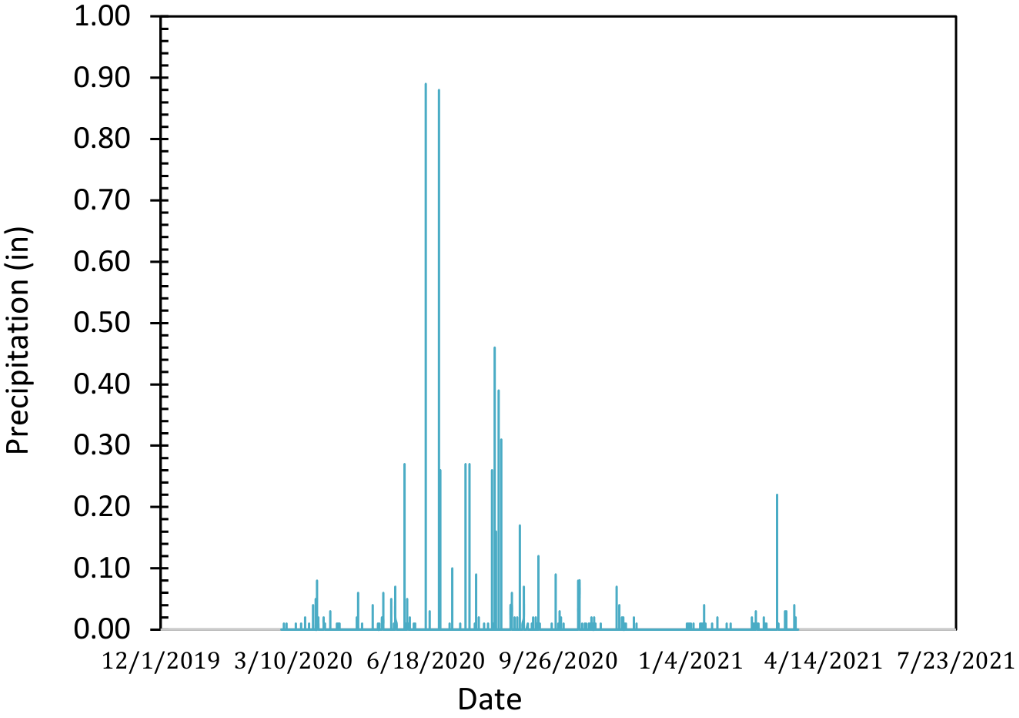

(a)

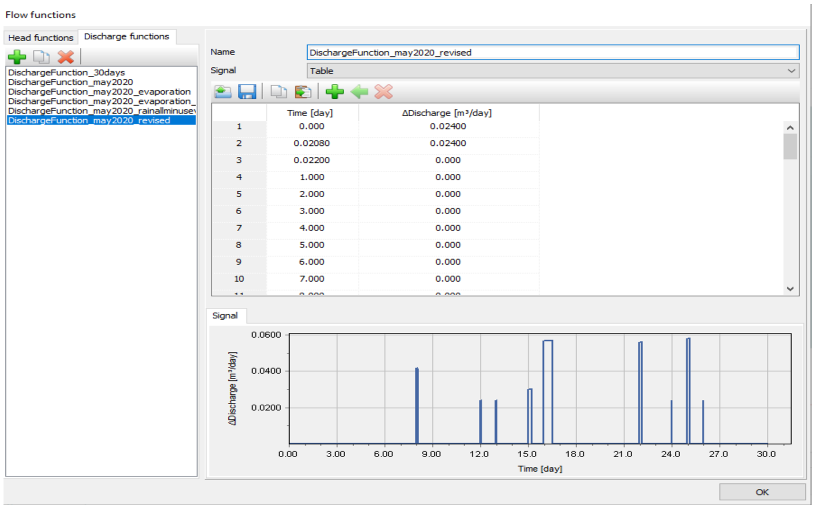

DischargeFunction_30days
DischargeFunction_may2020
DischargeFunction_may2020_evaporation
DischargeFunction_may2020_evaporation_
DischargeFunction_may2020_rainallminuse
DischargeFunction_may2020_revised

Name: DischargeFunction_may2020_revised
Signal: Table

	Time [day]	ΔDischarge [m³/day]
1	0.000	0.02400
2	0.02080	0.02400
3	0.02200	0.000
4	1.000	0.000
5	2.000	0.000
6	3.000	0.000
7	4.000	0.000
8	5.000	0.000
9	6.000	0.000
10	7.000	0.000

(b)

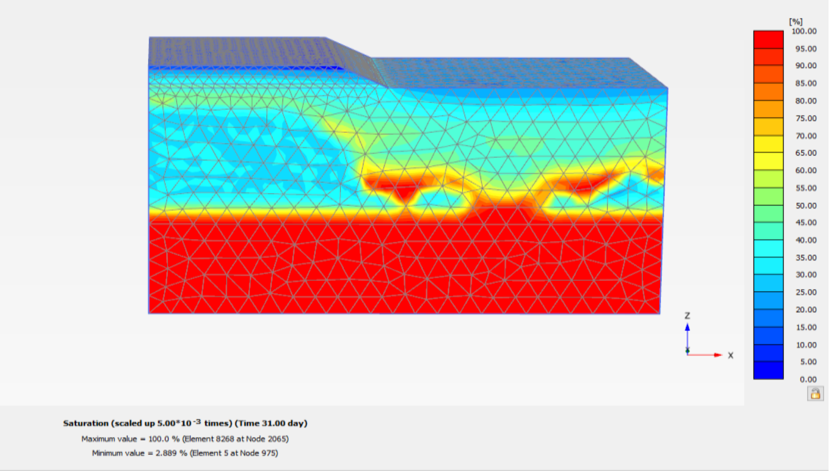

Saturation (scaled up $5.00*10^{-3}$ times) (Time 31.00 day)

Maximum value = 100.0 % (Element 8268 at Node 2065)

Minimum value = 2.889 % (Element 5 at Node 975)

(c)

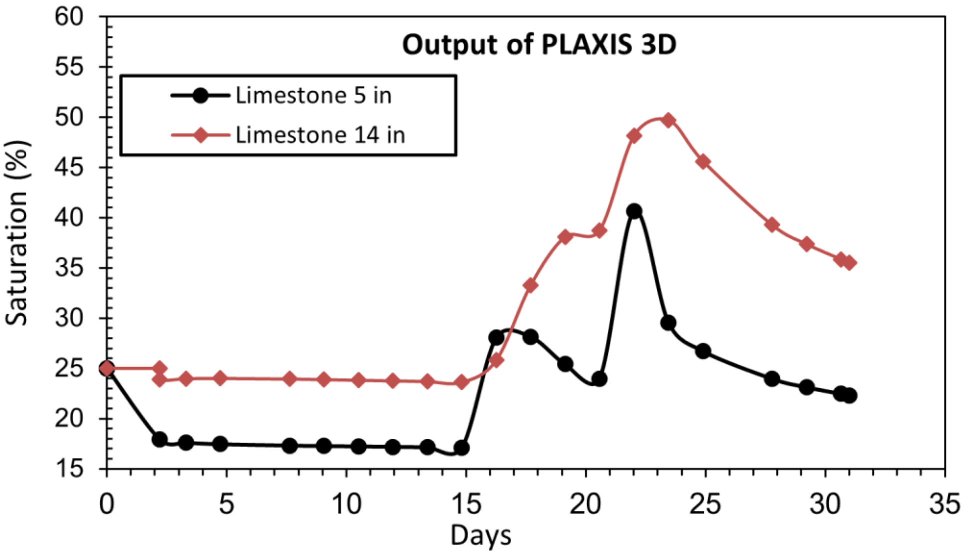

(d)

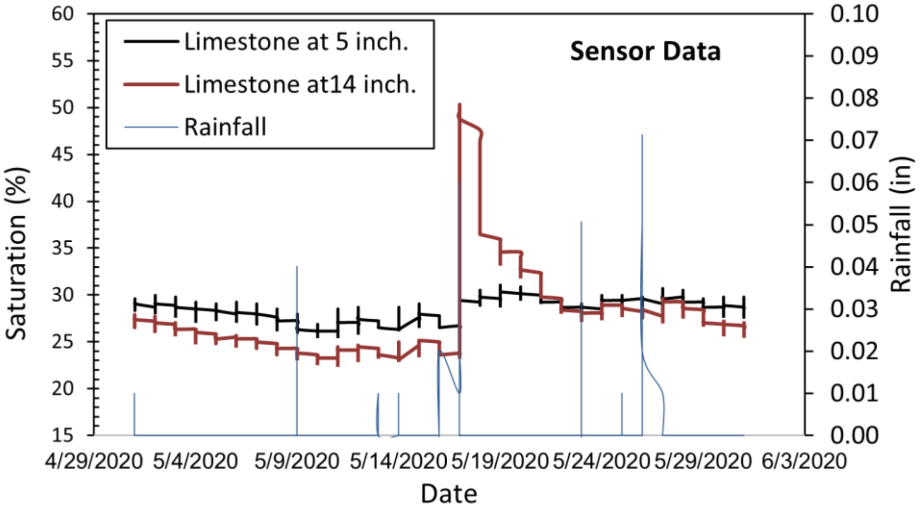

(e)

Figure 32. Saturation of limestone aggregate (a) rainfall at MnROAD facility (b) time dependent rainfall scenario in PLAXIS 3D (c) PLAXIS 3D simulation after 31 days (d) variation of saturation from PLAXIS 3D (e) rainfall and saturation data from field sensors

4.3 Cell 189

MnROAD Cell 189 structure has a 3.5 in select granular subbase, a 12 in a recycled aggregate base layer, a 3.5 in HMA layer, and clay subgrade soil. The base layer of Cell 189 was constructed using recycled concrete aggregate (RCA) and recycled asphalt pavement (RAP) aggregate. A 3D model was created in PLAXIS 3D using the material properties of Cell 189 to conduct finite-element analysis (**Figure 33)** .

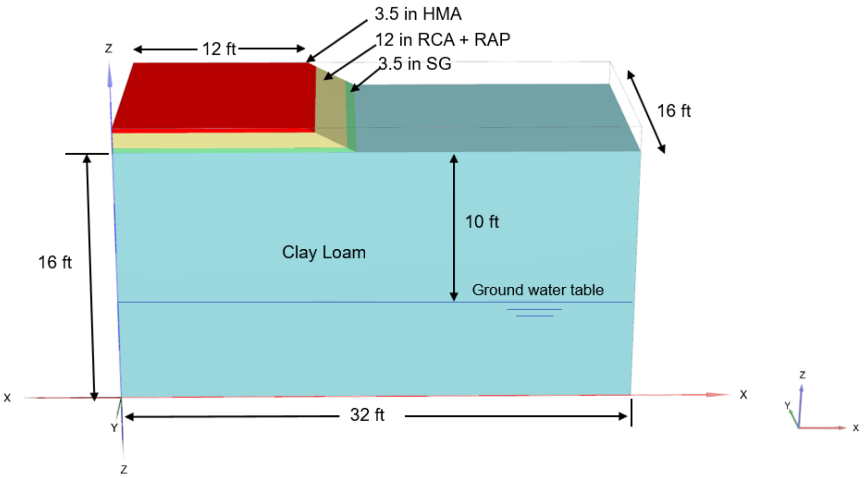

Figure 33. PLAXIS 3D model with the dimension of each layer for the Cell 189 structure

Since Cell 188 and Cell 189 were constructed with the same material except for the base layer, material properties similar to those of Cell 188 for asphalt concrete, select granular, and clay loam were used in PLAXIS 3D for rainfall simulation. The properties of the recycled base layer made of RCA+RAP were gathered from the study by Cetin et al. (2021). The list of material properties for PLAXIS 3D simulation of Cell 189 is shown in **Table 16**.

The variation in saturation for a finite-element model of Cell 189 after a 31-day rainfall simulation is shown in **Figure 34 (a)**. Like Cell188, the rainfall scenario for May 2020 was created in PLAXIS 3D, simulated the change in saturation over a 31-day interval, and recorded the saturation at two depths of the base layer. An initial saturation of 27% was considered the initial boundary condition for the simulation of moisture fluxes in the pavement layers. Saturation variation obtained from the finite-element model at two depths of the base layer is shown in **Figure 34 (b)**, and the saturation values at the same depths collected from two field sensors are shown in **Figure 34 (c)**. At a depth of 5 in, the top of the RCA+RAP base layer, a maximum saturation of 55.4% was obtained from PLAXIS 3D simulation, while the field sensor recorded a saturation value of 51.8%. At the bottom RCA+RAP base layer, the PLAXIS 3D simulation yielded a maximum saturation of 39.6% compared to the field sensor recorded saturation value of 33%.

Table 16. List of material properties for Cell 189 (Cetin et al. 2021 and Pease 2010)

Parameter	Symbol	Asphalt Concrete	RCA + RAP	Select Granular	Clay Loam	Unit
General						
Soil model		Linear elastic	Linear elastic	Linear elastic	Linear elastic	
Unsaturated unit weight	γ_{unsat}	145	130	120	115	lb/ft^3
Saturated unit weight	γ_{sat}	152	146	135	125	lb/ft^3
Initial void	e_{init}	0.07	0.30	0.40	0.32	
Mechanical						
Stiffness	E'_{ref}	200	28	21.8	10.0	ksi
Poisson's ratio	ϑ	0.3	0.35	0.35	0.35	
Groundwater						
van Genuchten model parameters	S_{res}	0.01	0.15	0.028	0.13	
	S_{sat}	1.0	1.0	1.0	1.0	
	g_n	8.320	4.50	1.93	2.8	
	g_a	1.677	2.80	4.52	3.82	
	g_l	0.15	-0.15	-0.36	1.2	
Hydraulic conductivity	K_x	0.002	0.738	4.10	0.26	in/hr
	K_y	0.002	0.738	4.10	0.26	in/hr
	K_z	0.002	0.738	4.10	0.26	in/hr

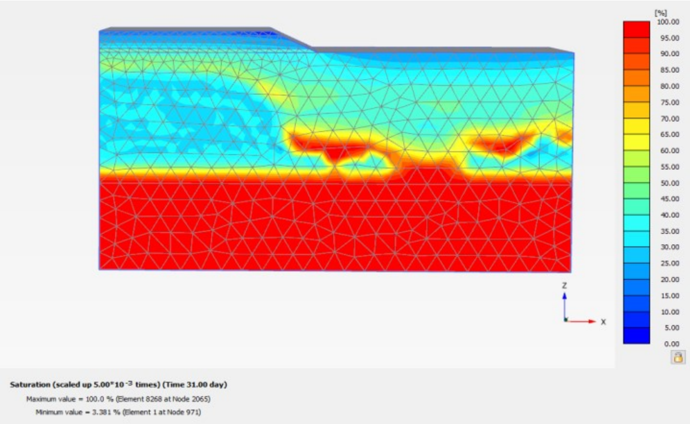

(a)

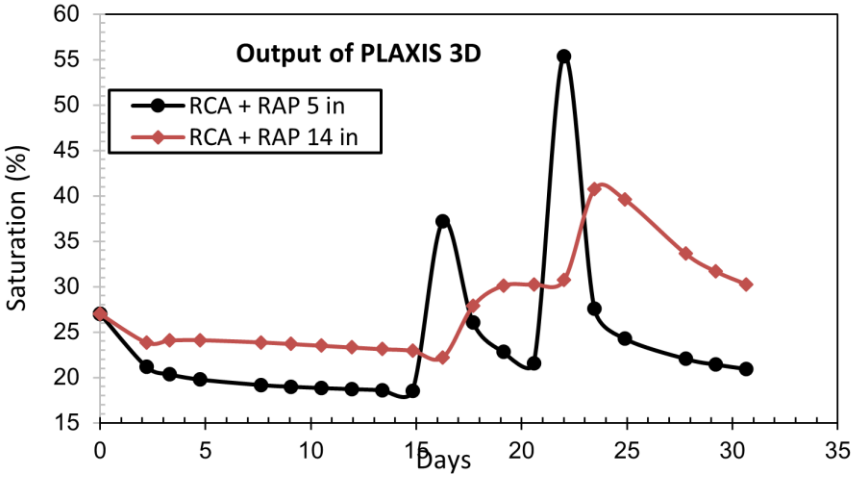

(b)

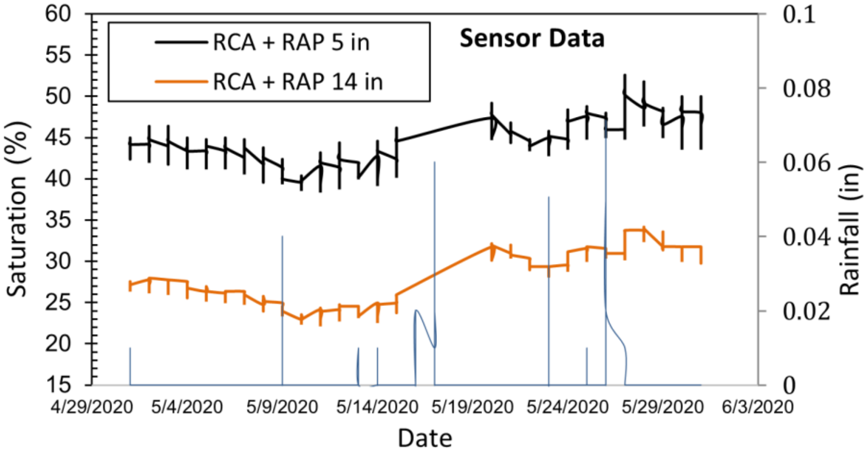

(c)

Figure 34. Saturation of RCA + RAP aggregate (a) PLAXIS 3D simulation after 31 days (b) variation of saturation from PLAXIS 3D (a) rainfall and saturation data from field sensors

4.4 Cell 127

The Cell 127 structure was created in PLAXIS 3D using the same HMA, base, and subbase layer thickness. A 12 ft wide HMA layer was used to simulate one traffic lane of Cell 127 in the MnROAD facility. The PLAXIS 3D model was comprised of a 3.5 in HMA layer, a 6 in Class 6 Aggregate base layer, and an 18 in large stone subbase (LSSB) layer. **Figure 35** shows the PLAXIS 3D model for Cell 127 created for moisture flux simulation.

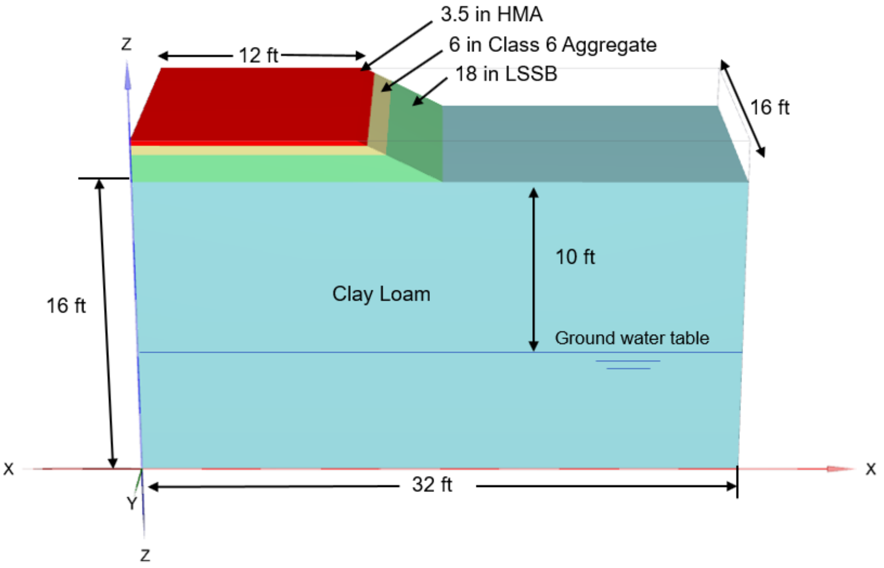

Figure 35. PLAXIS 3D model for the Cell 127 structure with dimensions of each layer

While the properties of asphalt concrete and clay loam for the PLAXIS 3D model of Cell 127 were similar to those of Cell 188 and Cell 189, the Class 6 aggregate properties were selected from the study conducted by Cetin et al. (2021). Values for the van Genuchten parameter and the saturated hydraulic conductivity for large stone subbase materials were assumed and finalized based on the output results of PLAXIS 3D models. These parameters were changed and finalized after comparing PLAXIS 3D-generated saturation data with the saturation data collected from sensors installed at Cell 127. **Table 17** lists the material properties of asphalt concrete, Class 6 aggregate, large stone subbase (LSSB,) and clay loam used for moisture flux simulation in PLAXIS 3D.

Table 17. List of material properties for Cell 127 (Cetin et al. 2021 and Pease 2010)

Parameter	Symbol	Asphalt Concrete	Class 6 Aggregate	LSSB	Clay Loam	Unit
General						
Soil model		Linear elastic	Linear elastic	Linear elastic	Linear elastic	
Unsaturated unit weight	γ_{unsat}	145	128	125	115	lb/ft³
Saturated unit weight	γ_{sat}	152	143	138	125	lb/ft³
Initial void	e_{init}	0.07	0.38	0.45	0.32	
Mechanical						
Stiffness	E'_{ref}	200	28	25.5	10.0	ksi
Poisson's ratio	ϑ	0.3	0.35	0.35	0.35	
Groundwater						
van Genuchten model parameters	S_{res}	0.01	0.20	0.07	0.13	
	S_{sat}	1.0	1.0	1.0	1.0	
	g_n	8.320	3.75	2.68	2.8	
	g_a	1.677	2.88	14.5	3.82	
	g_l	0.15	1.20	-2.33	1.2	
Hydraulic conductivity	K_x	0.002	7.39	32.8	0.26	in/hr
	K_y	0.002	7.39	32.8	0.26	in/hr
	K_z	0.002	7.39	32.8	0.26	in/hr

A similar approach to that used for Cell 188 and Cell 189, and considering the rainfall scenario in May 2020, was adopted for the rainfall simulation in PLAXI 3D. **Figure 36(a)** shows the saturation of different layers of Cell 127 due to rainfall in May 2020, while **Figure 36(b)** shows the variation of saturation obtained from PLAXIS 3D simulation at 6.5 in depths of the Class 6 aggregate layer; the saturation values at the same depth collected from field sensors and rainfall in May 2020 are shown in **Figure 6(c).** A maximum saturation of 44.4% at a depth of 6.5 in was obtained from PLAXIS 3D simulation, compared to the field-sensor-recorded saturation value of 48.6%.

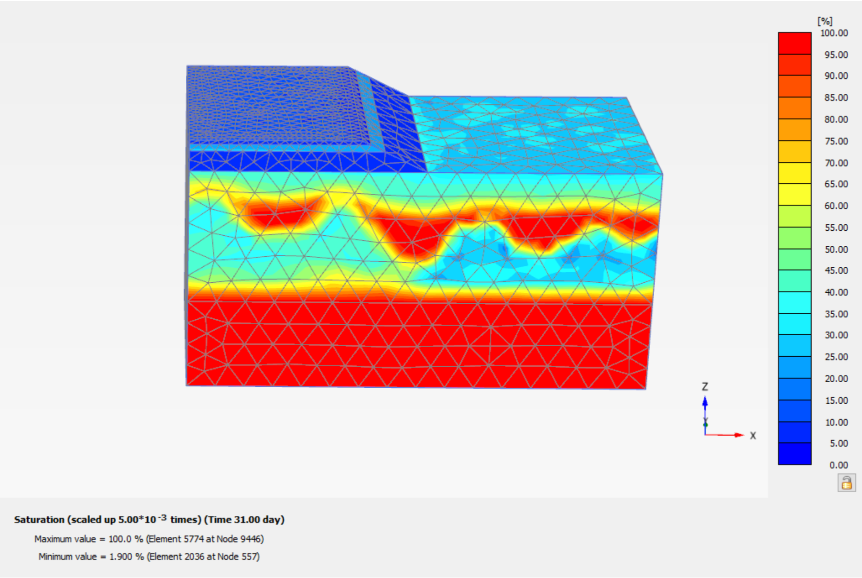

Saturation (scaled up 5.00*10^{-3} times) (Time 31.00 day)

Maximum value = 100.0 % (Element 5774 at Node 9446)

Minimum value = 1.900 % (Element 2036 at Node 557)

(a)

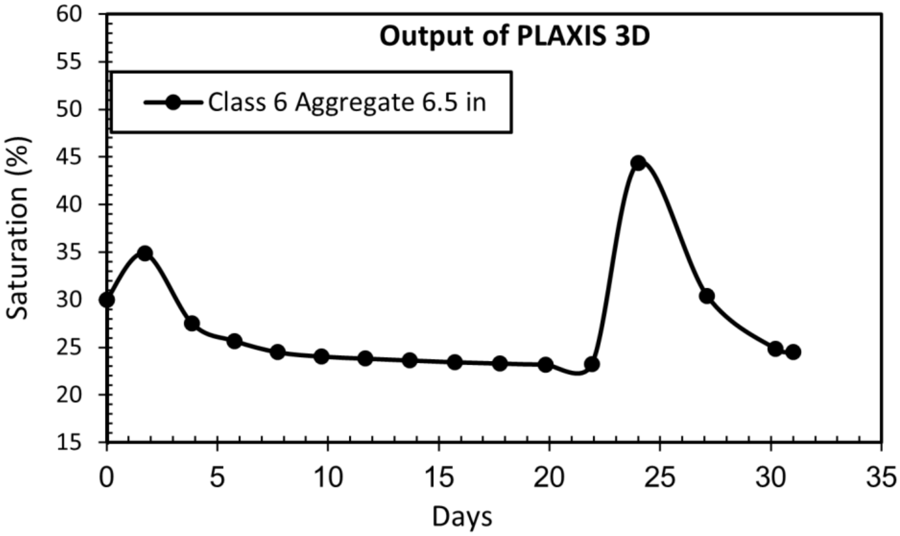

(b)

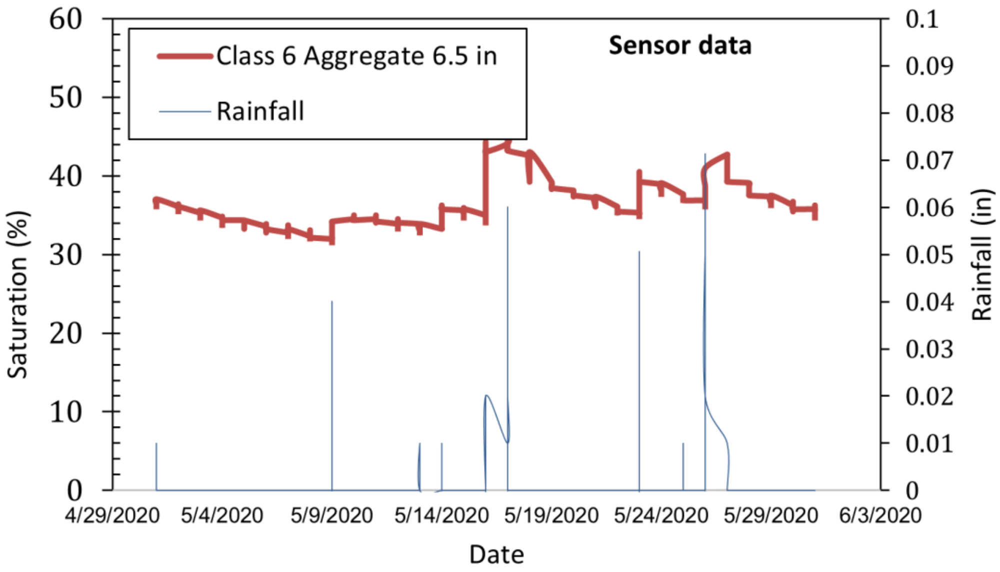

(c)

Figure 36. Saturation of Class 6 aggregate (a) PLAXIS 3D simulation after 31 days (b) variation of saturation from PLAXIS 3D (a) rainfall and saturation data from field sensors

4.5 Summary

This chapter described the creation of a finite-element model that could simulate moisture flux due to heavy rainfall, with cells 188, 189, and 127 selected as the reference pavement structures for developing such a finite-element model in PLAXIS 3D. A rainfall scenario in May 2020 at the MnROAD location was created in PLAXIS 3D to simulate the moisture flux in the pavement foundation layers. Since Cell 188, Cell 189, and Cell 127 have Decagon moisture sensors installed in the base layer to collect volumetric moisture content data, saturation values at the same depth from PLAXIS 3D model were extracted after rainfall simulation to validate the model. While most of the material properties for PLAXIS 3D modeling were selected from previous studies conducted by Cetin et al. (2021), values for van Genuchten parameters and saturated hydraulic conductivity for asphalt concrete, large stone subbase, and select granular subbase were unavailable from previous studies. A trial PLAXIS 3D model with assumed material properties was first created, and those properties were finalized after many trial simulations. Field sensor estimated saturation values were selected as a reference to select the best possible van Genuchten parameters and saturated hydraulic conductivity. Since rainfall simulation in PLAXIS is highly sensitive to van Genuchten parameters and hydraulic conductivity of the materials, using accurate material properties led to the best results. While hydraulic properties for large stone subbase, select granular subbase, and asphalt concrete were assumed in the PLAXIS 3D analysis, it is recommended that actual hydraulic properties be used to better estimate moisture flux due to heavy rainfall.

Chapter 5: Developing A Saturation Prediction Model And GIS Map of the MNROAD Facility

5.1 Introduction

Material properties of a certain number of cells in MnDOT were used in PLAXIS 3D for assessing the impact of moisture movement on the pavement system. PLAXIS 3D models were used for the simulation of the moisture movement due to assumed different rainfall scenario. However, there is a need of development of saturation prediction models for specific cells of MnDOT facility as well as universal models for other cells not studied in this research. In this chapter, four models were developed for different cells to estimate saturation of pavement base layer which were subsequently used in MEPDG equation to calculate corresponding M_R.

Esri's GIS software ArcGIS Pro was utilized in this study to generate a preliminary vulnerability map by using developed saturation and M_R prediction model. This map can serve as invaluable tools for engineers, and the general public, enhancing both preparedness and response to heavy precipitation events. By understanding how varying aggregates behave under heavy rainfall events, engineers and planners can proactively plan maintenance and construction activities, ultimately enhancing the resilience and longevity of Minnesota's road infrastructure. The objectives of this chapter are (a) developing mechanistic-based prediction models incorporating different statewide aggregate types and (b) creating a preliminary GIS-based pavement foundation vulnerability map for a selected number of MnROAD cells representing Minnesota's typical pavement systems.

5.2 Developing Saturation Prediction Model

Different aggregate properties were used to create a comprehensive database of base-layer saturation, and these properties were incorporated into the pavement models created in PLAXIS 3D. This database of base-layer saturation values served as a foundation for developing prediction models that used rainfall intensity, duration, and hydraulic properties of aggregates to forecast the degree of saturation in the base aggregate layer.

5.2.1 Available Statewide Aggregate Information

Oh et al. (2021) conducted an extensive study investigating the drainage quality of base aggregates commonly used in Minnesota. A collection of coarse-grained samples was obtained from stakeholders of the National Road Research Alliance (NRRA) to encompass a variety of materials utilized or considered for use in transportation infrastructure system construction. The materials consisted of 17 distinct samples, including poorly graded sand (SP), silty sand (SM), well-graded sand (SW), poorly-graded gravel (GP), silty gravel (GM), and well-graded gravel (GW). Material selection was a collaborative effort among NRRA representatives and the MnDOT, the Missouri Department of Transportation (MoDOT), and the Wisconsin Department of Transportation (WisDOT), and the study included only aggregates used in Minnesota during base-layer construction. Cetin et al. (2021) also conducted an extensive laboratory and field investigation that monitored the performance of base aggregates from the MnROAD facility managed by the MnDOT, comprised more than 50 distinct test cells constructed with various base, subbase, and surface course materials. **Table 18** lists commonly used aggregates in pavement base-layer constructions in Minnesota.

Table 18. List of base aggregates and their classification (Cetin et al. 2021 and Oh et al. 2021)

Material ID	Name	USCS Classification
#1	Limestone	GM
#2	RCA+RAP	SP-SM
#3	MN Class 6	SP-SM
#4	MN Class 5	SW-SM
#5	Bryan Redrock Class 5, MnDOT Pit 70006	GM
#6	Bryan Redrock Ball Diamond material, MnDOT Pit 70006	SM
#7	MN Class 5Q	GW

5.2.2 Representative Pavement Models

Four cells from MnROAD low-volume road were considered in this study to generate a representative pavement model in PLAXIS 3D. In Chapter 4, three pavement models were created in PLAXIS 3D to represent Cell 188, Cell 189, and Cell 127 of the MnROAD facility; these cells represented the limestone, RCA+RAP, and MN Class 6 aggregate, respectively. Model-generated saturation data was compared to field moisture sensor data for model validation. In this Chapter, Cell 188 at MnROAD low-volume road represented pavement structure for MN Class 5, Bryan Redrock Class 5, and Bryan Redrock Ball Diamond aggregates. Cell 328 from a MnROAD low-volume road represented MN Class 5Q aggregates. **Table 19** lists representative cells are considered for generating PLAXIS 3D models for each material type. and **Figure 31** provides the dimensions of each pavement layer created in the PLAXIS 3D model. Seeking to gain insight into how different base aggregates respond to rainfall, rainfall simulations were conducted to observe and capture the response of these different base aggregates to rainfall events. Such insight is expected to provide valuable information for pavement design and maintenance considerations.

Table 19. Lists of materials and their representative Cells for PLAXIS 3D models

Material ID	Name	Representative Cells and PLAXIS 3D models
#1	Limestone	Cell 188
#2	RCA+RAP	Cell 189
#3	MN Class 6	Cell 127
#4	MN Class 5	Cell 188
#5	Bryan Redrock Class 5, MnDOT Pit 70006	Cell 188
#6	Bryan Redrock Ball Diamond material, MnDOT Pit 70006	Cell 188
#7	MN Class 5Q	Cell 328

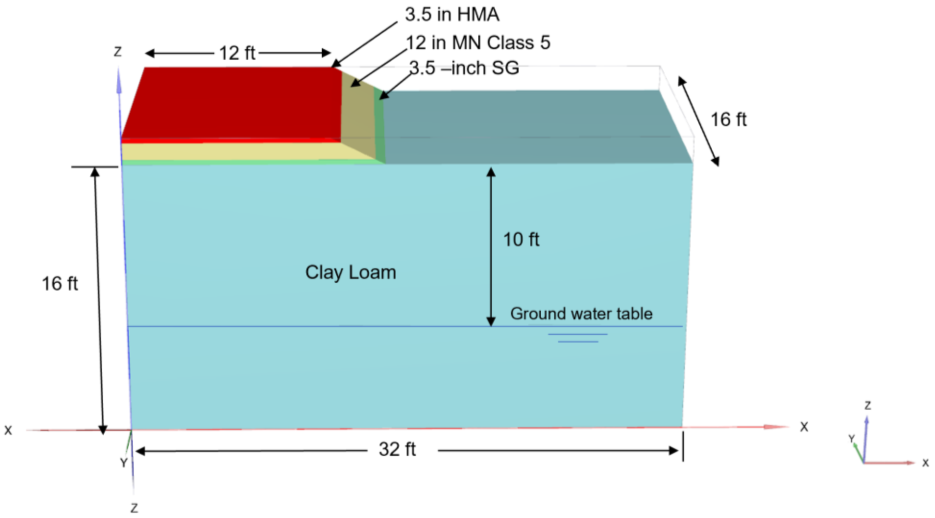

Figure 37. A representative PLAXIS 3D model with the dimensions of each layer for MN Class 5, Bryan Redrock Class 5, and Bryan Redrock Ball Diamond aggregates

The key material properties for PLAXIS 3D hydraulic modeling dealing with unsaturated-soil behavior were parameters related to soil/water characteristic curves and saturated hydraulic conductivity of the materials. The input material properties for the representative PLAXIS 3D model are listed in

Table 20. The configuration of Cell 328 was established within PLAXIS 3D with identical thicknesses for the HMA, base, and subbase layers. A 12 ft wide HMA layer was utilized to replicate a single traffic lane within Cell 328 at the MnROAD facility. Within the PLAXIS 3D model, the structural composition included a 3.5-inch HMA layer, a 6-inch MN Class 5Q Aggregate base layer, and a 9-inch layer of large stone subbase (LSSB). **Figure 38** illustrates the Cell 328 structure in PLAXIS 3D for moisture flux simulation.

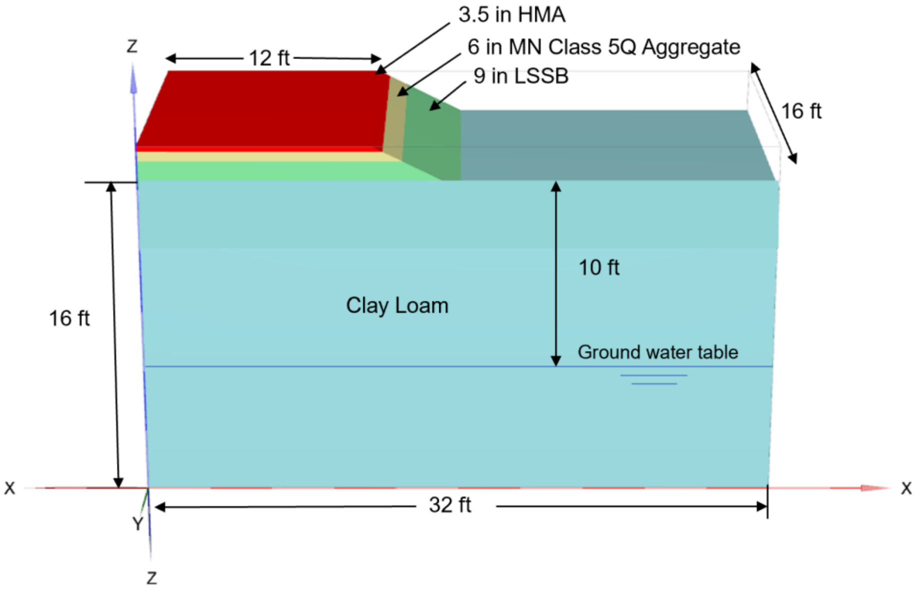

Figure 38. A representative PLAXIS 3D model with the dimensions of each layer for MN Class 5Q aggregates

Table 20. List of material properties for representative pavement model (Cetin et al. 2021 and Pease 2010)

Parameter	Symbol	Asphalt Concrete	MN Class 5	Select Granular	Clay Loam	Unit
General						
Soil model		Linear elastic	Linear elastic	Linear elastic	Linear elastic	
Unsaturated unit weight	γ_{unsat}	145	128	120	115	lb/ft^3
Saturated unit weight	γ_{sat}	152	146	135	125	lb/ft^3
Initial void	e_{init}	0.07	0.25	0.40	0.32	
Mechanical						
Stiffness	E'_{ref}	200	29.0	21.8	10.0	ksi
Poisson's ratio	ϑ	0.3	0.35	0.35	0.35	
Groundwater						
van Genuchten model parameters	S_{res}	0.01	0.12	0.028	0.13	
	S_{sat}	1.0	1.0	1.0	1.0	
	g_n	8.320	3.16	1.93	2.8	
	g_a	1.677	1.46	4.52	3.82	
	g_l	0.5	0.50	-0.36	1.2	
Hydraulic conductivity	K_x	0.002	4.25	4.10	0.26	in/hr
	K_y	0.002	4.25	4.10	0.26	in/hr
	K_z	0.002	4.25	4.10	0.26	in/hr

The properties of asphalt concrete and clay loam for the PLAXIS 3D model of Cell 328 were similar to those of Cell 127, while the properties of MN Class 5Q aggregate were obtained from the study conducted by Oh et al. (2021). **Table 21** lists the material properties of asphalt concrete, MN Class 5Q aggregate, large stone subbase (LSSB,) and clay loam used for moisture flux simulation in PLAXIS 3D.

Table 21. List of material properties for Cell 328 (Cetin et al. 2021 and Pease 2010)

Parameter	Symbol	Asphalt Concrete	MN Class 5Q Aggregate	LSSB	Clay Loam	Unit
General						
Soil model		Linear elastic	Linear elastic	Linear elastic	Linear elastic	
Unsaturated unit weight	γ_{unsat}	145	127	125	115	lb/ft^3
Saturated unit weight	γ_{sat}	152	142	138	125	lb/ft^3
Initial void	e_{init}	0.07	0.38	0.45	0.32	
Mechanical						
Stiffness	E'_{ref}	200	29	25.5	10.0	ksi
Poisson's ratio	ϑ	0.3	0.35	0.35	0.35	
Groundwater						
van Genuchten model parameters	S_{res}	0.01	0.10	0.07	0.13	
	S_{sat}	1.0	1.0	1.0	1.0	
	g_n	8.320	1.38	2.68	2.8	
	g_a	1.677	3.62	14.5	3.82	
	g_l	0.15	0.50	-2.33	1.2	
Hydraulic conductivity	K_x	0.002	7.39	32.8	0.26	in/hr
	K_y	0.002	7.39	32.8	0.26	in/hr
	K_z	0.002	7.39	32.8	0.26	in/hr

5.2.3 Saturation of Pavement Base Layer

Multiple rainfall scenarios were simulated and the resulting moisture fluxes within the base aggregate layers were computed using PLAXIS 3D. In this simulation, the lower and upper limits of rainfall intensity were set at 1 in/hr and 8 in/hr, with a maximum rainfall duration of 12 hours considered. These rainfall intensity and duration values were chosen based on the previous 25 years of historical rainfall data at the MnROAD facility. The simulation was run for one day to check the change in saturation inside the pavement layer as time passed. The saturation condition of Cell 188 after 4 hrs of rainfall with an intensity of 5 in/hr is presented in Figure 39(a), while Figure 39(b) shows the variation in saturation in Cell 188 at different rainfall intensities of 4 hr duration. Note that saturation of 25% was considered as an initial boundary condition for Cell 188. Figure 39(c) and Figure 39(d) illustrate the variation of saturation in Cell 189 and Cell 127 due to different rainfall intensities. The initial boundary conditions for the saturation in Cell 189 and Cell 127, 27% and 30%, respectively, were selected based on the field sensor data.

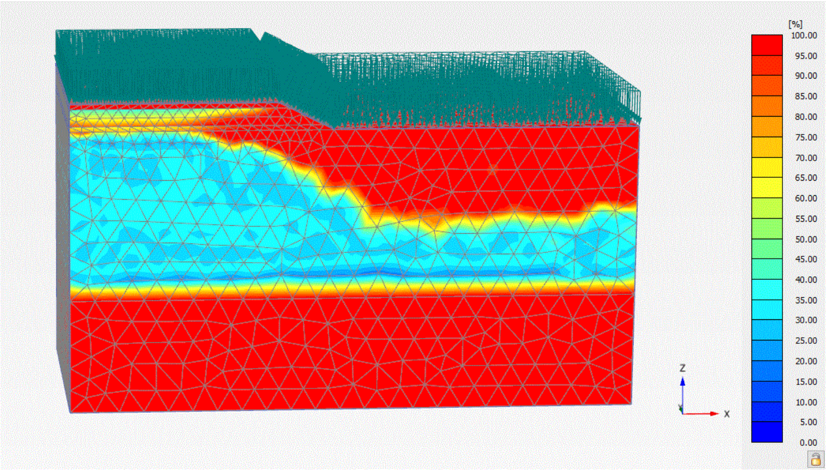

(a)

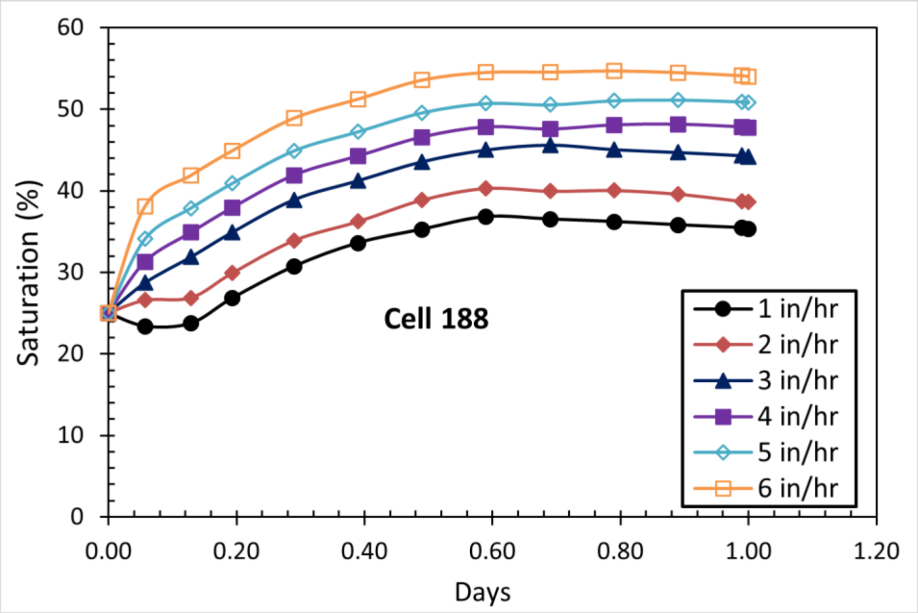
60
50
40
30
20
10
0
Saturation (%)
0.00
0.20
0.40
0.60
0.80
1.00
1.20
Days
Cell 188
1 in/hr
2 in/hr
3 in/hr
4 in/hr
5 in/hr
6 in/hr

(b)

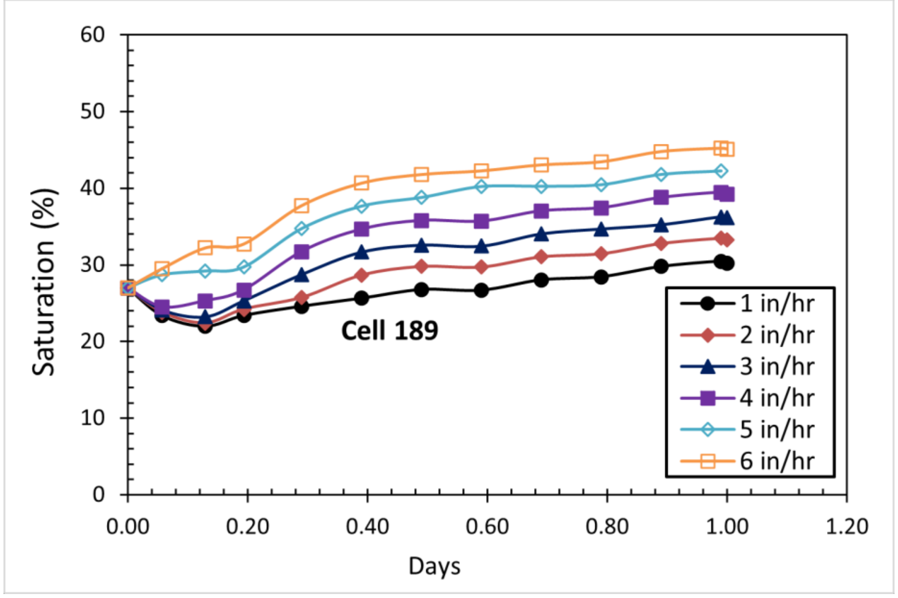
60
50
40
30
20
10
0
Saturation (%)
0.00
0.20
0.40
0.60
0.80
1.00
1.20
Days
Cell 189
1 in/hr
2 in/hr
3 in/hr
4 in/hr
5 in/hr
6 in/hr

(c)

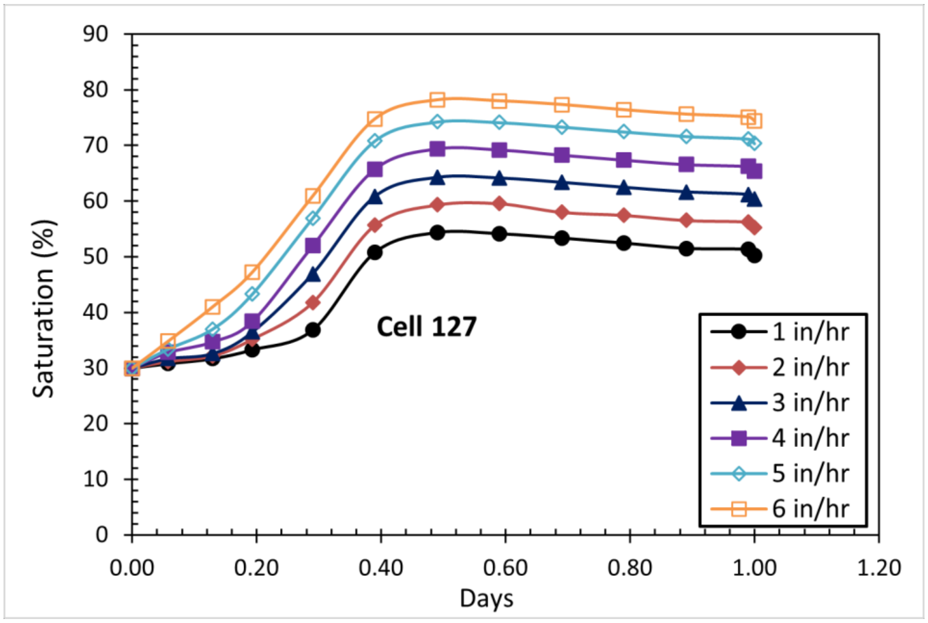

(d)

Figure 39. Variation of saturation in (a) pavement structure of Cell 188, (b) middle of limestone aggregate base layer of Cell 188, (c) RCA + RAP aggregate layer of Cell 189, and (d) Class 6 aggregate layer of Cell 127 due to rainfall intensity ranging from 1 in/hr to 6 in/hr and duration of 4 hrs

After calculating saturation values within the middle of the base layer, a prediction model was developed for forecasting saturation levels based on rainfall intensity, duration, and hydraulic conductivity. The linear regression model shown in Equation (9) exhibits an R-squared value of 0.84 and an RMSE value of 2.87 (**Figure 40**).

$$Saturation\ (\%) = 21.63 + 3.60 \times RI + 2.83 \times RD - 0.34 \times HC \tag{9}$$

where *RI* is rainfall intensity in in/hr, *RD* is rainfall duration in hr, and *HC* is saturated hydraulic conductivity in in/hr. An equality plot between predicted saturation and the PLAXIS 3D model simulated saturation is shown in **Figure 40**.

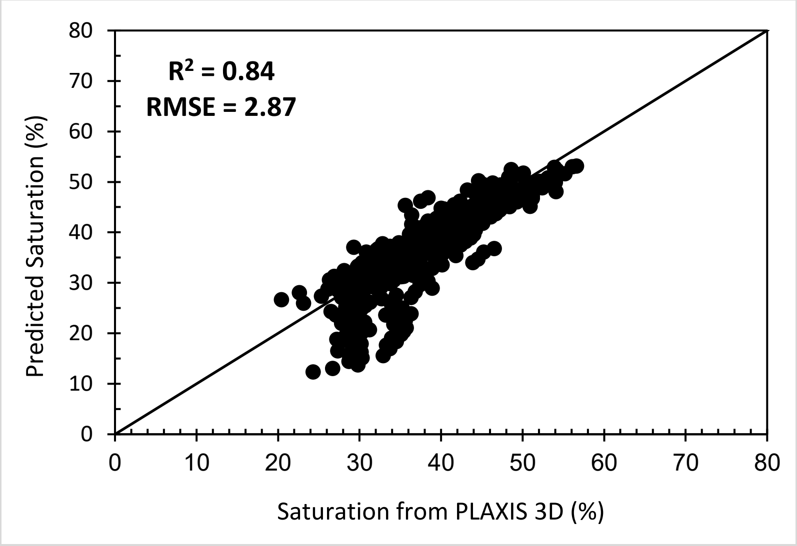

Figure 40. Equality plot between predicted saturation and simulated saturation from PLAXIS 3D

After the saturation of base aggregates had been predicted, Equation (5) was used to calculate the M_R of aggregates corresponding to each of the saturation values. For fine-grained soils, parameter values a = 0.5934, b = 0.4, and k_m = 6.1324 are recommended; for coarse-grained soils, parameter values a =-0.3123, b = 0.3, and k_m = 6.8157 are recommended (Zapata et al. 2007, Witczak et al. 2000).

Variation in M_R for limestone aggregate with the change of saturation due to heavy rainfall is shown in **Figure 41**. The saturation corresponding to optimum moisture content was 26% for limestone aggregate, and the M_R at optimum moisture content was assumed to be 29,000 psi. A prediction model was developed for LImestone aggregate to estimate the change in M_R due to heavy rainfall with a certain intensity and duration. Equation (10) shows the M_R prediction model for limestone aggregate; it has an R-squared value of 0.96 and an RMSE value of 481.34.

$$M_R\ (Limestone\ Aggregate) = 29{,}599.8 - 1{,}076.8\ \times RI - 1{,}310.4 \times RD \qquad (10)$$

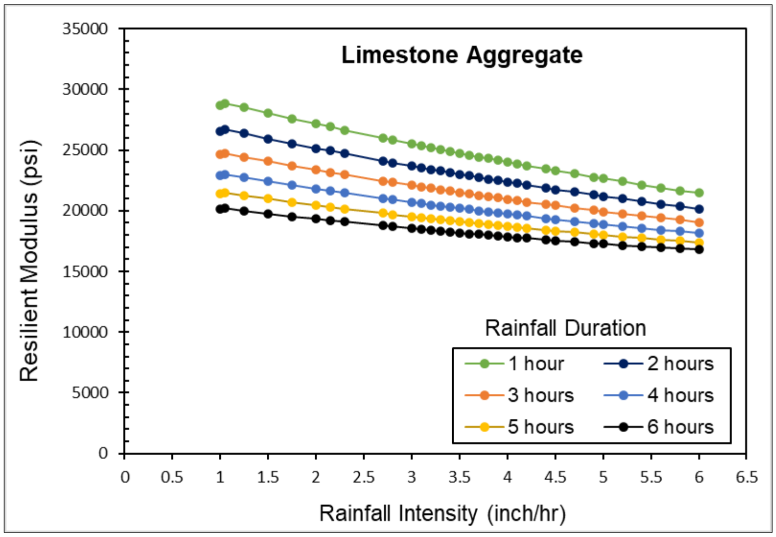

Figure 41. Variation of resilient modulus of limestone aggregate with heavy rainfall

Variation of the M_R for RCA+RAP with change of saturation due to heavy rainfall is shown in **Figure 42**. The saturation corresponding to optimum moisture content was 30% for RCA+RAP, and the M_R at optimum moisture content was assumed to be 29,000 psi. The prediction model shown in Equation (11) was developed for Class 6 aggregate to provide an estimation of the change in M_R due to heavy rainfall with certain intensity and duration. This model provides good prediction accuracy; its R-squared value was 0.96 and RMSE value was 480.23.

$$M_R\ (Class\ 6\ Aggregate) = 30{,}059.7 - 1{,}105.2\ \times RI - 1{,}345.8 \times RD \tag{11}$$

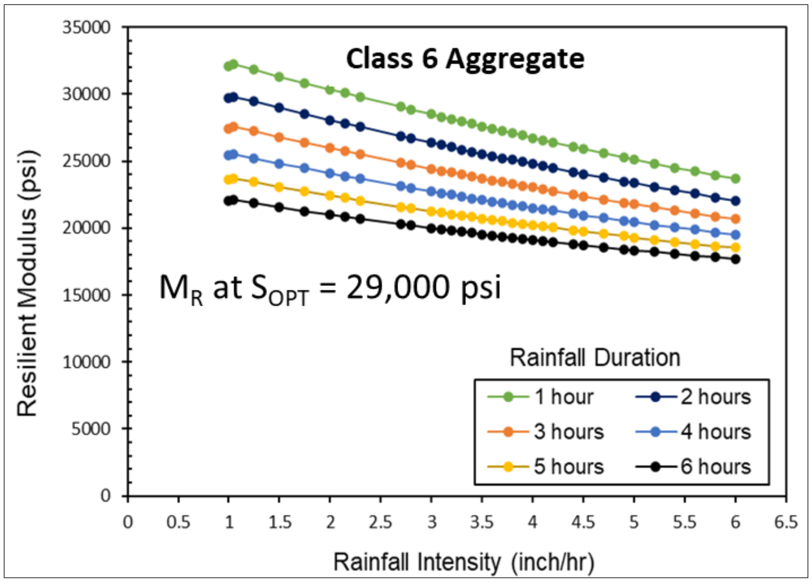

Figure 42. Variation of resilient modulus of Class 6 aggregate with heavy rainfall

Figure 43 shows M_R variation for RCA+RAP Aggregate with the saturation change due to heavy rainfall. The saturation corresponding to optimum moisture content was 25% for RCA+RAP aggregate, and the resilient modulus at optimum moisture content was assumed to be 28,000 psi. Equation (12) shows a prediction model for RCA+RAP aggregate that provides an estimation of the change in M_R due to heavy rainfall with a certain intensity and duration. An R-squared value of 0.94 and an RMSE value of 183.46 reflect the good prediction accuracy of the linear regression model. **Figure 43** depicts the lesser influence of heavy rainfall on M_R values of RCA+RAP aggregate, which can be attributed to the higher hydraulic conductivity of the LSSB layer that helps heavy rainfall-induced moisture fluxes to be drained quickly, facilitating faster drainage of class 6 aggregate without a significant increase in moisture flux due to heavy rainfall.

$$M_R\ (RCA + RAP) = 18{,}723 - 340.4\ \times RI - 407.9 \times RD \qquad (12)$$

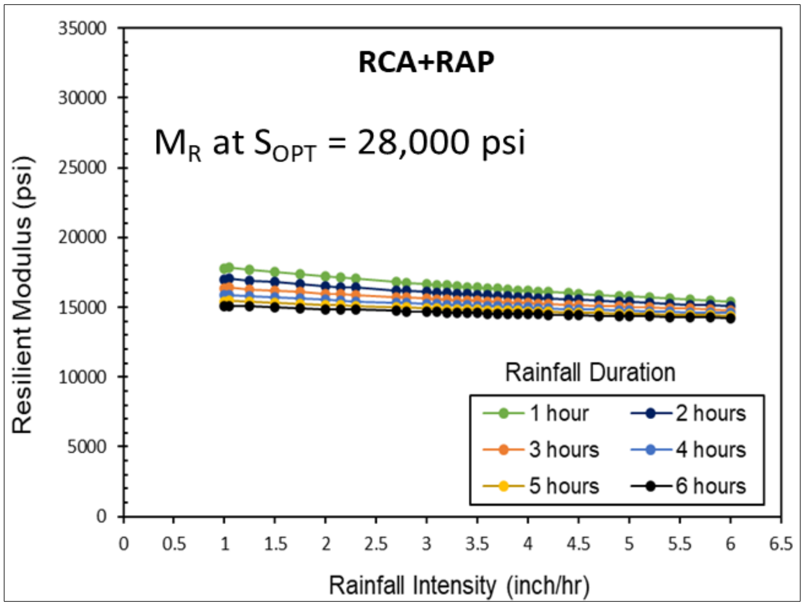

Figure 43. Variation of resilient modulus of Class 6 aggregate with heavy rainfall

5.3 Developing A Vulnerability Map For MNROAD

The preliminary vulnerability map was automatically generated by a Python script using data manipulation libraries that included Numpy, Pandas, and Geo-pandas. Several spatial data sets relevant to pavement foundations were used as fixed inputs that included hydraulic conductivity (*HC*) of aggregates and saturation at optimum moisture content (S_{OPT}). Weather data of MnROAD collected at 15-minute intervals were provided in Microsoft Excel format by a technical advisory panel (TAP) member. The Python script collected necessary values, i.e., user inputs from a CSV file and weather information from the Microsoft Excel file. The input CSV file contained the following information –

Location – latitude and longitude of the location of the pavement.

Cell number or Identifier – cell number for MnROAD facility cells. The saturation calculation equations were different for Cell 127, 188, 189 and 328, and based on cell number the saturation calculation function was executed.

Date –date of rainfall duration and intensity.

S_{OPT} –Saturation value at optimum moisture content.

$M_{R\text{-}OPT}$ –M_R value at optimum moisture content.

Hydrlic _conduc – Hydraulic conductivity.

The script used the date from the CSV file to extract weather information, followed by calculating the saturation value. M_R values were calculated using specific equations for each cell. Finally, an Esri shapefile was created based on location information and M_R values. The complete workflow is depicted in **Figure 44**.

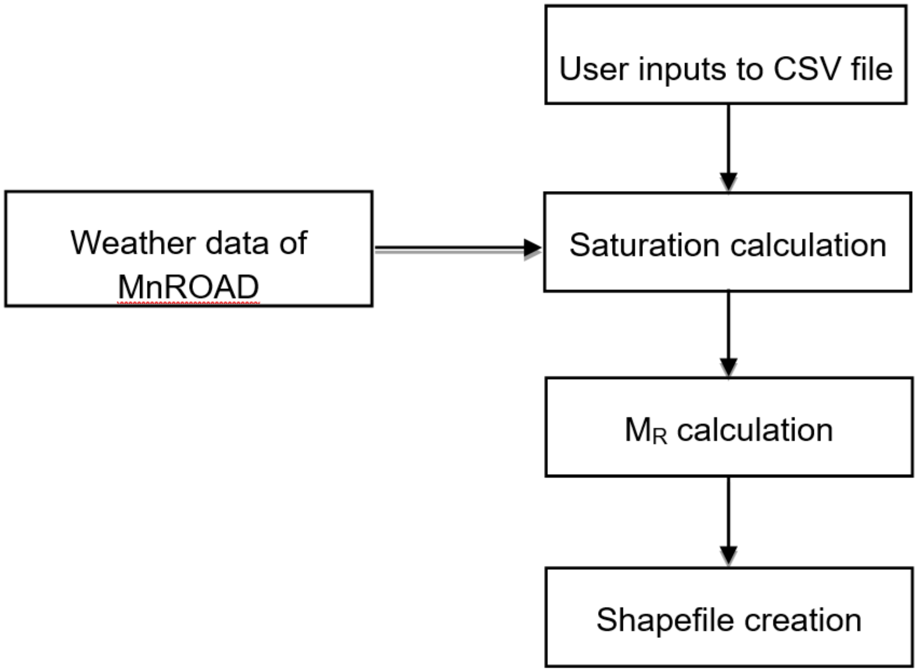

Figure 44. Flowchart for pavement foundation vulnerability assessment

5.3.1 User input

Before running the script, the user must provide location information, cell number, date of the rainfall event, S_{OPT}, $M_{R\text{-}OPT}$, and hydraulic conductivity from the CSV file. A sample of such user input is provided in **Table 22**.

Table 22. Sample input values for the vulnerability map

Latitude	Longitude	Cell No.	Date	S_{OPT}	$M_{R\text{-}OPT}$	Hydraulic conductivity
				%	psi	in/hr
45.263752	-93.71294	127	12-Aug-20	0.2515	30,000	7.39
45.264146	-93.713659	188	12-Aug-20	0.2625	28,000	0.919
45.264544	-93.714397	189	12-Aug-20	0.3448	25,000	0.739
45.262932	-93.711427	328	12-Aug-20	0.30	25,000	0.738

5.3.2 Saturation Calculation

The script read the user inputs and extracted only the rainfall duration and intensity from the weather data; the rainfall intensity was calculated by dividing the total rainfall amount by the total rainfall duration. Equations (13), (14) and (15) were utilized for calculating saturation at the middle of the base layer for Cell 188, Cell 189, and Cell 127, respectively, with models for the individual cells developed and calibrated based on field moisture sensor data from Task 3. They predict saturation due to heavy rainfall. Saturation for Cell 328 was estimated using Equation (9) along with corresponding hydraulic conductivity values of MN Class 5Q aggregate. Note that Cell 328 was considered in this study as a non-calibrated cell. Rainfall intensity and duration were extracted from weather data, while hydraulic conductivity was a user input value.

$$Saturation\ (\%)\ (Cell\ 188) = 22.31 + 2.70 \times RI + 3.31 \times RD \qquad (13)$$

$$Saturation\ (\%)\ (Cell\ 189) = 20.65 + 3.61 \times RI + 3.15 \times RD \qquad (14)$$

$$Saturation\ (\%)\ (Cell\ 127) = 18.97 + 3.27 \times RI + 2.71 \times RD \qquad (15)$$

5.3.3 Resilient Modulus Calculation

The M_R of the aggregates was calculated for each saturation value using the MEPDG formula shown in Equation (5). In this equation, saturation (*s*) was obtained from the prediction models, and parameter values *a* = -0.3123, *b* = 0.3, and k_m = 6.8157 are recommended for coarse-grained soils (Zapata et al.

2007, Witczak et al. 2000). **Table 23** lists the extracted rainfall information from the weather station and calculated saturation and M_R values.

Table 23. Calculated MR and saturation values based on the example input values and extracted rainfall information

Cell No	Date	Rainfall Intensity	Rainfall Duration	Saturation	M_R
		in/hr	hr	%	psi
127	12-Aug-20	4.5	0.34	31.01	25,893.3
188	12-Aug-20	4.5	0.34	36.5	21,887.7
189	12-Aug-20	4.5	0.34	34.58	24,743.0
328	12-Aug-20	4.5	0.34	34.02	22,527.5

5.3.4 Shapefile Generation

At each earlier step, rainfall duration, rainfall intensity, saturation, and calculated M_R value were saved into a Geo-pandas dataframe, and a shapefile that can be imported to any geographic information system or remote sensing software (such as QGIS, ArcGIS, ERDAS IMAGINE) is generated in Esri format using the information from that dataframe. An example map is provided in **Figure 45**. The complete Python codes are listed in appendix A.

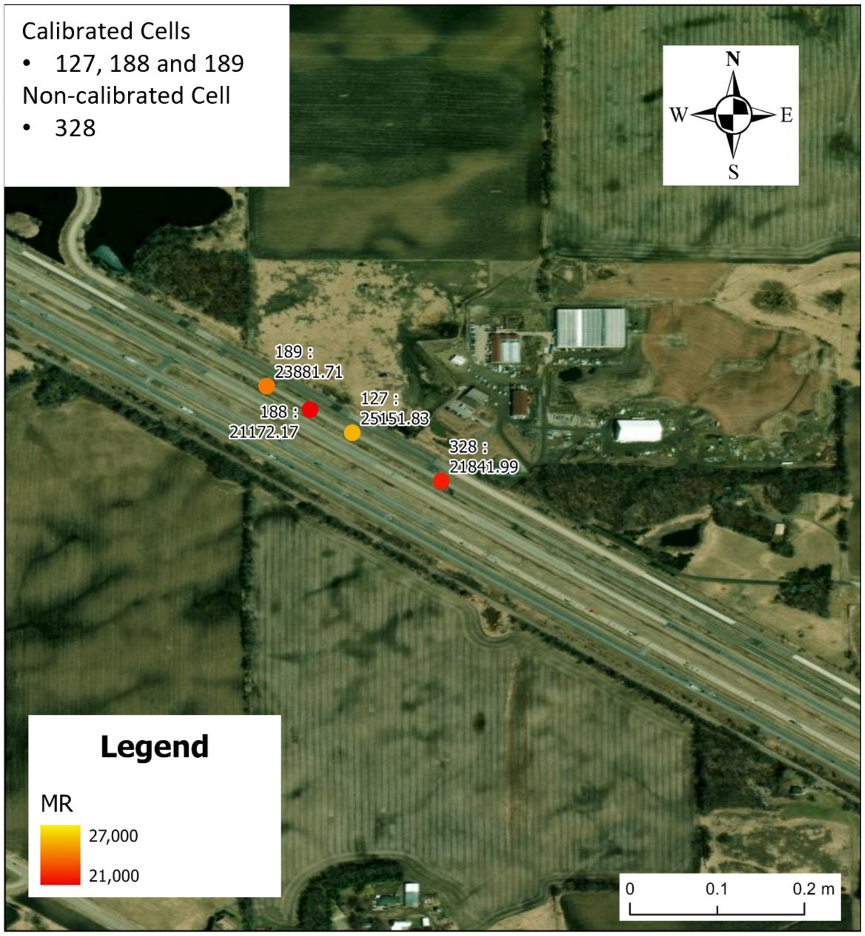

Figure 45. ArcGIS generated a vulnerability map for MnROAD low volume road

5.4 Summary

After finding all material properties, several rainfall scenarios with different intensities and durations were created in PLAXIS 3D, with moisture flux in pavement layers simulated for 24 hours. From the simulations, the saturation of the base layer was estimated for each of the rainfall scenarios. The upper limit for rainfall intensity was 6 in/hr, and the upper limit for duration was 6 hrs. The initial saturation before rainfall was selected from the field sensor data as the initial boundary condition for the PLAXIS 3D simulation. During rainfall simulation in PLAXIS 3D, no ponding water scenario was considered; it was assumed that extra water after infiltration would be runoff from the asphalt concrete surface within 24 hrs. A multiple linear regression model was then developed to predict saturation at the base layer based on rainfall intensity and duration. Regression models to predict base layer stiffness based on hydraulic conductivity, rainfall intensity, and duration for three distinct aggregate types were developed by incorporating different statewide types of aggregate used in Minnesota's pavement systems. These refined models were then used to create a preliminary GIS-based pavement foundation vulnerability map for a selected site, offering insights into the resilience of Minnesota's pavement systems. The study utilized Esri's ArcGIS Pro, a leading GIS software tool, and Python programming for automation and scripting. The developed script takes weather data from a Microsoft Excel file and user inputs from a CSV file, with user input includes location, cell number or identifier, date, pavement material saturation value at optimum moisture content (S_{OPT}), M_R value at the optimum moisture content ($M_{R\text{-}OPT}$), and hydraulic conductivity. This information was used to calculate saturation, then followed by an M_R calculation. Finally, a shapefile was generated, and all input information, including saturation and M_R value, were saved into the shapefile. The GIS map development process involved four major steps: data collection, data processing, modeling, and output mapping. Data from MnDOT weather stations were collected from TAP members, processed into a tabular format using Python data analysis libraries, and integrated into ArcGIS Pro to create dynamic maps to visualize changes in pavement foundation soil's M_R values due to moisture variations caused by heavy precipitation.

Chapter 6: Recommendation For Asset Management Practices

Addressing climate change and its potential impact on heavy precipitation events is a critical concern for infrastructure agencies such as the MnDOT, and proactive measures are necessary to enhance resilience and ensure the safety and functionality of the transportation network. The findings of this study can serve as the initial step toward addressing the challenges posed by heavy rainfall, including recommendations for mitigation measures and minimizing road network maintenance costs. In this study, an innovative GIS mapping system framework for vulnerability assessment and visualization of the risk of using a road network immediately after heavy rainfall was developed using MnROAD low-volume road cells as case study. The preliminary GIS map demonstrates the feasibility of developing a statewide vulnerability map in future studies. This map could rank management areas based on risk levels, offering valuable insights for professionals such as district, county, and city engineers, planners, project managers, and maintenance staff. The following is a list of recommendations for MnDOT district engineers and asset managers:

- Invest in advanced weather-monitoring and forecasting systems to provide real-time data on heavy precipitation events and share them for public use. The script developed in this study requires some additional work to access publicly accessible real-time accurate data and periodically upload the vulnerability map on a freely available web-based server.
- Assess specific climate-change impact on the region, including projections for increased heavy precipitation events.
- Quantify the potential risks and consequences of heavy precipitation events on infrastructure and transportation operations using a GIS model.
- Develop and implement early-warning systems to alert motorists and maintenance teams about potential hazards and road closures.
- Prioritize maintenance activities of vulnerable road networks to improve resilience, especially in heavy rainfall areas.
- Update infrastructure design standards and guidelines to account for changing precipitation patterns, ensuring that newer projects are more resilient to heavier rainfall.
- Provide training and capacity-building programs for MnDOT staff and contractors on climate-resilience best practices.

Chapter 7: Summary and Conclusions

This research focused on studying the impact of heavy precipitation events on moisture levels in pavement foundation layers at the MnROAD facility. Historical precipitation data confirmed increasing trends in heavy precipitation in Minnesota in the 21st century. The study initially selected five (5) test cells based on the availability of moisture data and analyzed the relationship between heavy precipitation and pavement foundation moisture. Cells in the MnROAD low-volume and mainline roads exhibited no consistent trend in volumetric content, but early peak moisture was associated with thawing events. Issues with data records from EW-Decagon moisture sensors were noted. The report discussed unexpectedly high moisture content in some cases, potentially attributed to sensor limitations or calibration errors.

The ISU research team analyzed data from only 2009 to 2012 due to missing data in later years. Additional high-quality moisture data provided by TAP members for Cells 127, 188, and 189 from the MnROAD low-volume road exhibited consistent trends in moisture change, with early peaks in March and summer peaks due to heavy precipitation. The third chapter summarized the index, hydraulic, and thermal properties of base aggregates and clay loam subgrade soils for Cells 127, 188, and 189. Material properties were used for hydraulic modeling in PLAXIS 3D. The report noted the absence of hydraulic properties for certain materials in the previous study.

The fourth chapter detailed the creation in PLAXIS 3D of a finite-element model to simulate moisture flux due to heavy rainfall. Rainfall scenarios were simulated, and material properties were finalized after trial simulations. A multiple linear regression model was developed to predict base-layer saturation based on rainfall intensity and duration. After finding saturation, the MEPDG equation for M_R estimation at different saturation levels was used to determine pavement foundation susceptibility. Finally, three regression models were developed to predict changes in M_R for limestone aggregate, RCA+RAP aggregate, and Class 6 aggregate due to heavy rainfall events. It was observed from the simulation that heavy rainfall events significantly reduced the M_R of the base layer. While RCA+RAP aggregate was estimated to be more susceptible under heavy rainfall events since the initial reduction in MR value was higher due to heavy rainfall, the predicted M_R values fell into a narrow range, showing less influence on M_R with increasing rainfall intensity and duration.

The study used GIS to create a preliminary pavement foundation vulnerability map for a selected site. Overall, the report investigated the complex relationship between heavy rainfall, moisture levels in pavement layers, and M_R values, using data from specific cells in the MnROAD facility for in-depth analysis and modeling.

Chapter 8: Future Work and Recommendations

Based on the limitations of the current study, the following are recommended areas for future study:

(i) Extend the study to include various pavement structures from different regions of Minnesota to capture a broader spectrum of environmental and climatic influences. This will contribute to the development of a statewide road network vulnerability map.

(ii) Consider diverse subgrade soils and subbase types to account for variations in material properties, providing a more comprehensive understanding of the impact of heavy precipitation on different pavement configurations.

(iii) Regularly integrate the latest weather station data into models and maps to ensure the accuracy and relevance of predictions. Given the dynamic nature of climate conditions, continuous data updates will enhance the reliability of the study's outcomes.

(iv) Continuously validate and calibrate mechanistic-based regression models with field data to enhance their accuracy in predicting pavement foundation stiffness under varying conditions. Regular updates will ensure the reliability of these models.

(v) Conduct comprehensive material testing, especially focusing on hydraulic properties for materials with limited data. Address the gaps in knowledge of hydraulic properties for certain materials identified in the previous study.

(vi) Validate assumed values for unknown material properties used on the finite-element model, ensuring that the model accurately represents real-world conditions.

(vii) Scale up GIS-based mapping efforts to cover a larger geographic area, providing a more detailed and comprehensive pavement foundation vulnerability map for the entire state of Minnesota.

(viii) Work collaboratively with transportation authorities to translate research findings into practical measures that enhance the resilience and longevity of Minnesota's pavement systems. Provide guidelines and best practices for infrastructure development and maintenance.

References

Abbas, A., Fathifazl, G., Isgor, O. B., Razaqpur, A. G., Fournier, B., & Foo, S. (2007). Proposed method for determining the residual mortar content of recycled concrete aggregates. *Journal of ASTM International, 5*(1), 1-12.

Abdollahi, M., & Vahedifard, F. (2022). Predicting resilient modulus of unsaturated subgrade soils considering effects of water content, temperature, and hydraulic hysteresis. *International Journal of Geomechanics, 22*(1), 04021259.

ASTM D 18. (2006). *Standard test method for permeability of granular soils (constant Head).* ASTM International, West Conshohocken, PA.

ASTM D 6836 (2016). *Standard test methods for determination of the soil water characteristic curve for desorption using a hanging column, pressure extractor, chilled mirror hygrometer, and/or centrifuge.* ASTM Int, West Conshohocken, PA.

Biot, M. A. (1941). General theory of three-dimensional consolidation. *Journal of Applied Physics, 12*(2), 155-164.

Cetin, B., Coban, H. S., Edil, T. B., Ceylan, H., Likos, W. J., Zheng, J., & Buss, A. (2021). *Determining pavement design criteria for recycled aggregate base and large stone subbase* (No. NRRA202103). Minnesota Department of Transportation, St. Paul, MN.

Drumm, E. C., Reeves, J. S., Madgett, M. R., & Trolinger, W. D. (1997). Subgrade resilient modulus correction for saturation effects. *Journal of Geotechnical and Geoenvironmental Engineering, 123*(7), 663-670.

FHWA. (2022). LTPP InfoPave – Home. Retrieved from https://infopave.fhwa.dot.gov

Francois, B., & Laloui, L. (2008). ACMEG-TS: A constitutive model for unsaturated soils under non-isothermal conditions. *Int. J. Numer. Anal. Methods Geomech, 32* (16), 1955–1988. https://doi.org/10.1002/nag.712

Jibon, M., & Mishra, D. (2021). Light weight deflectometer testing in proctor molds to establish resilient modulus properties of fine-grained soils. *Journal of Materials in Civil Engineering, 33*(2), 06020025.

Goodman, C. C., & Vahedifard, F. (2019). Micro-scale characterization of clay at elevated temperatures. *Géotech. Lett. 9*(3), 225–230. https://doi.org/10.1680/jgele.19.00026

Kim, D., Kim, G., & Baek, H. (2015). Relationship between thermal conductivity and soil-water characteristic curve of pure bentonite-based grout. *Int. J. Heat Mass Transf., 84*, 1049–1055. https://doi.org/10.1016/j.ijheatmasstransfer.2015.01.091

Li, D., & Selig, E. T. (1994). Resilient modulus for fine-grained subgrade soils. *Journal of Geotechnical Engineering, 12*0(6), 939-957.

Likos, W. J., Lu, N., & Godt, J. W. (2013). Hysteresis and uncertainty in soil water-retention curve parameters*. Journal of Geotechnical and Geoenvironmental Engineering, 140*(4), 04013050.

Mahedi, M., Satvati, S., Cetin, B., & Daniels, J. L. (2020). Chemically induced water repellency and the freeze-thaw durability of soils. *J. Cold Reg. Eng*. Retrieved from https://doi.org/10.1061/(ASCE)CR.1943-5495.0000223

Mishra, D., Jibon, M., Kassem, E., Bayomy, F. & Chowdhury, S. M. R. (2019). *Unbound materials characterization for pavement ME Implementation in Idaho* (No. FHWA-ID19-263). Idaho Department Transportation Department, Boise, ID.

MnDOT. (2013). *MnROAD – Moisture sensing documentation*. Retrieved from https://www.dot.state.mn.us/mnroad/files/moisture-sensing-at-mnroad-working-document.pdf

MnDOT. (2014). MnROAD weather stations [WWW Document]. Retrieved from https://www.dot.state.mn.us/mnroad/pdfs/MnROADWeather2014.pdf

MnDOT. (2022a). About MnROAD – MnROAD home. Retrieved from https://www.dot.state.mn.us/mnroad/

MnDOT. (2022b). Environmental sensors - MnROAD. Retrieved from https://www.dot.state.mn.us/mnroad/data/environmental-sensors.html

Mualem, Y. (1976). A new model for predicting the hydraulic conductivity of unsaturated porous media. *Water Resour. Res. 12*, 513–522.

National Cooperative Highway Research program (NCHRP). (2004). NCHRP 1-37A. *Design guide mechanistic-empirical design of new and rehabilitated pavement structures* (Appendix DD-1, Resilient modulus as function of soil moisture: Summary of predictive models. Retrieved from http://onlinepubs.trb.org/onlinepubs/archive/mepdg/guide.htm

Nokkaew, K., Tinjum, J. M., & Benson, C. H. (2012). Hydraulic properties of recycled asphalt pavement and recycled concrete aggregate. In *GeoCongress 2012: State of the art and practice in geotechnical engineering*, pp. 1476-1485.

Oh, H., Likos, W. J., & Edil, T. B. (2021). *Drainability of base aggregate and sand* (No. NRRA202107). Minnesota Department of Transportation, St. Paul, MN.

Pease, R. E. (2010). *Hydraulic properties of asphalt concrete.* The University of New Mexico, Albuquerque, NM.

Richards, L. A. (1931). Capillary conduction of liquids through porous mediums. *Cit. Phys. 1*, 318. https://doi.org/10.1063/1.1745010

U.S. Global Change Research Program. (2021). *Heavy precipitation.* Retrieved from https://www.globalchange.gov/browse/indicators/heavy-precipitation

van Genuchten, M. T. (1980). A closed-form equation for predicting the hydraulic conductivity of unsaturated soils. *Soil Science Society of America Journal, 44*(5), 892-898.

Witczak, M. W., Andrei, D., & Houston, W. N. (2000). *Resilient modulus as function of soil moisture – Summary of predictive models. Development of the 2002 guide for the development of new and rehabilitated pavement structures* (NCHRP 1-37 A, Inter Team Technical Report, Seasonal 1). Arizona State University, Tempe, Arizona.

Zapata, C. E., Andrei, D., Witczak, M. W., & Houston, W. N. (2007). Incorporation of environmental effects in pavement design. *Road Materials and Pavement Design, 8*(4), 667-693. https://doi.org/10.3166/rmpd.8.667-693

Appendix A: Analysis of Moisture Data

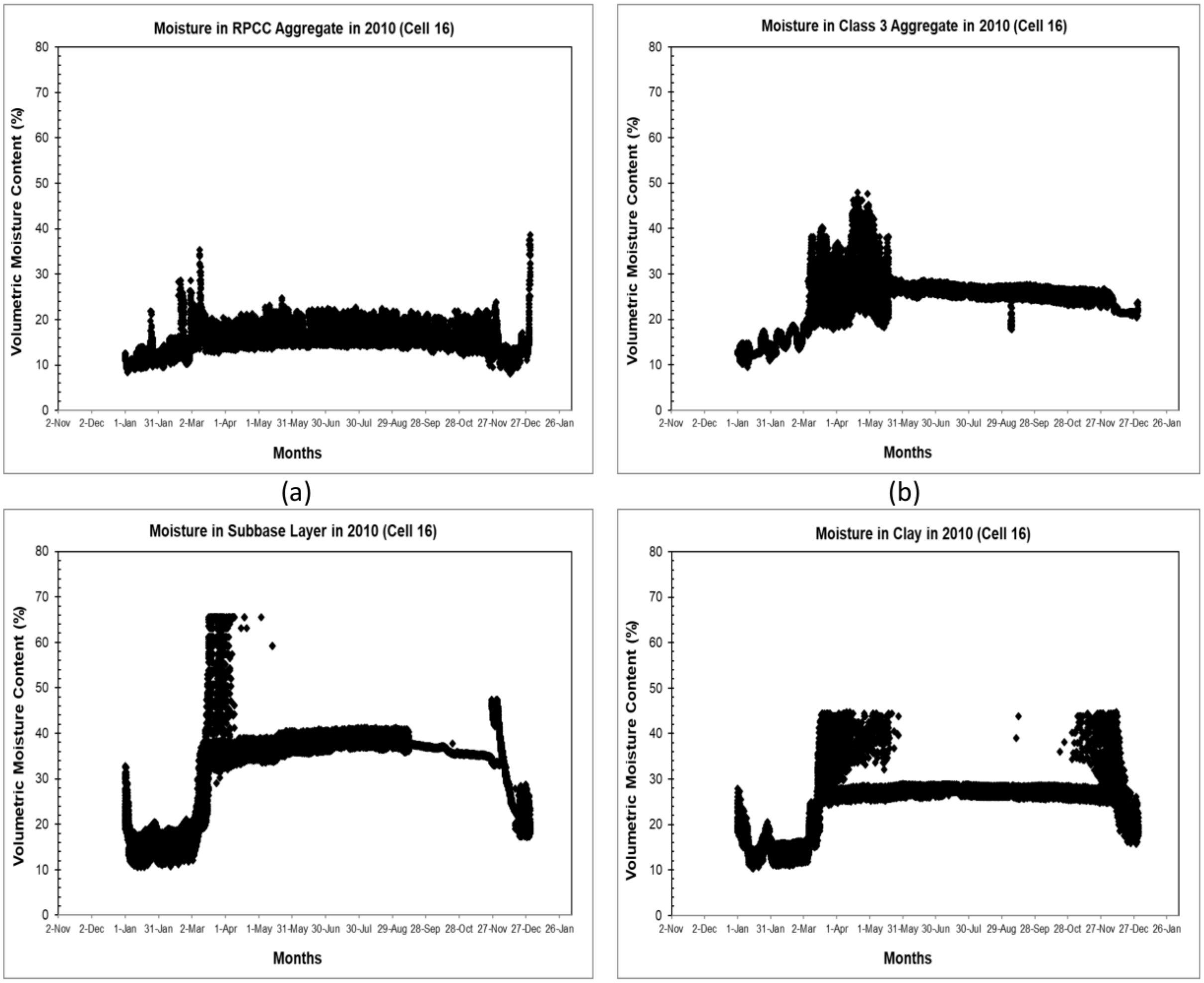

(a) (b)

(c) (d)

Figure A1. Volumetric moisture content trend of Cell 16 in 2010 for (a) RCA base (b) Class 3 aggregate base (c) SG subbase and (d) clay subgrade layer

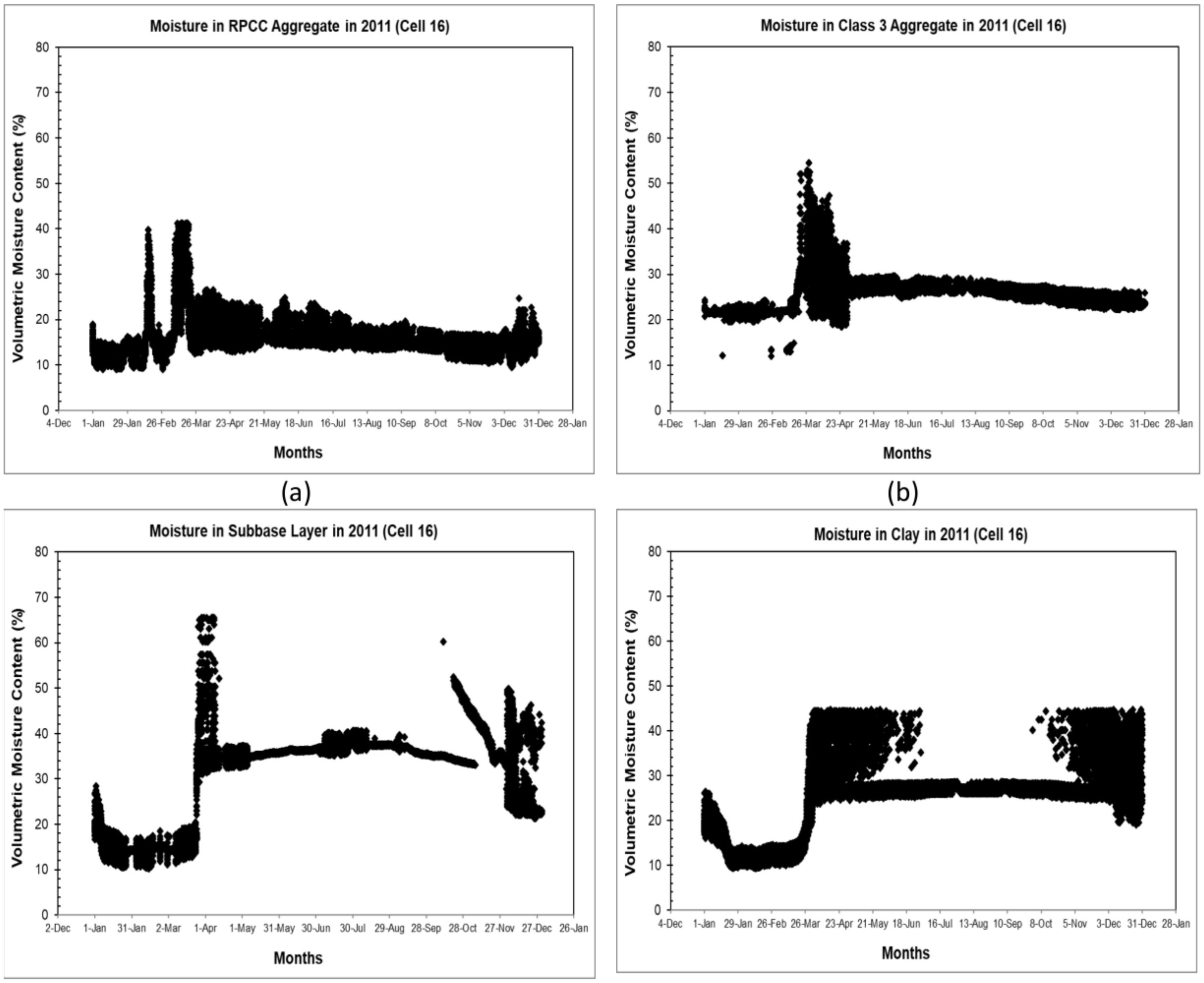

(a) (b)

(c) (d)

Figure A2. Volumetric moisture content trend of Cell 16 in 2011 for (a) RCA base (b) Class 3 aggregate base (c) SG subbase and (d) clay subgrade layer

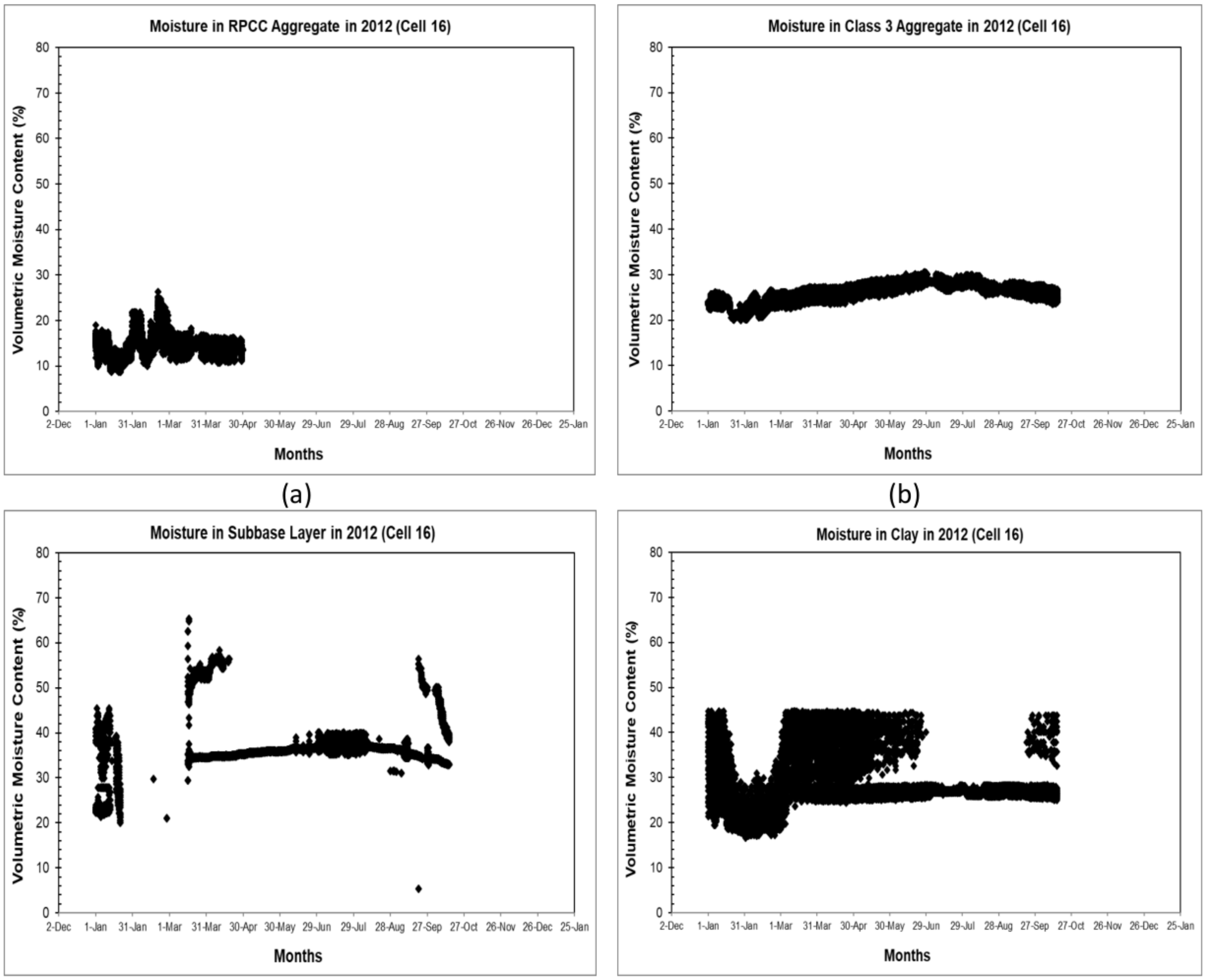

(a) (b)

(c) (d)

Figure A3. Volumetric moisture content trend of Cell 16 in 2012 for (a) RCA base (b) Class 3 aggregate base (c) SG subbase and (d) clay subgrade layer

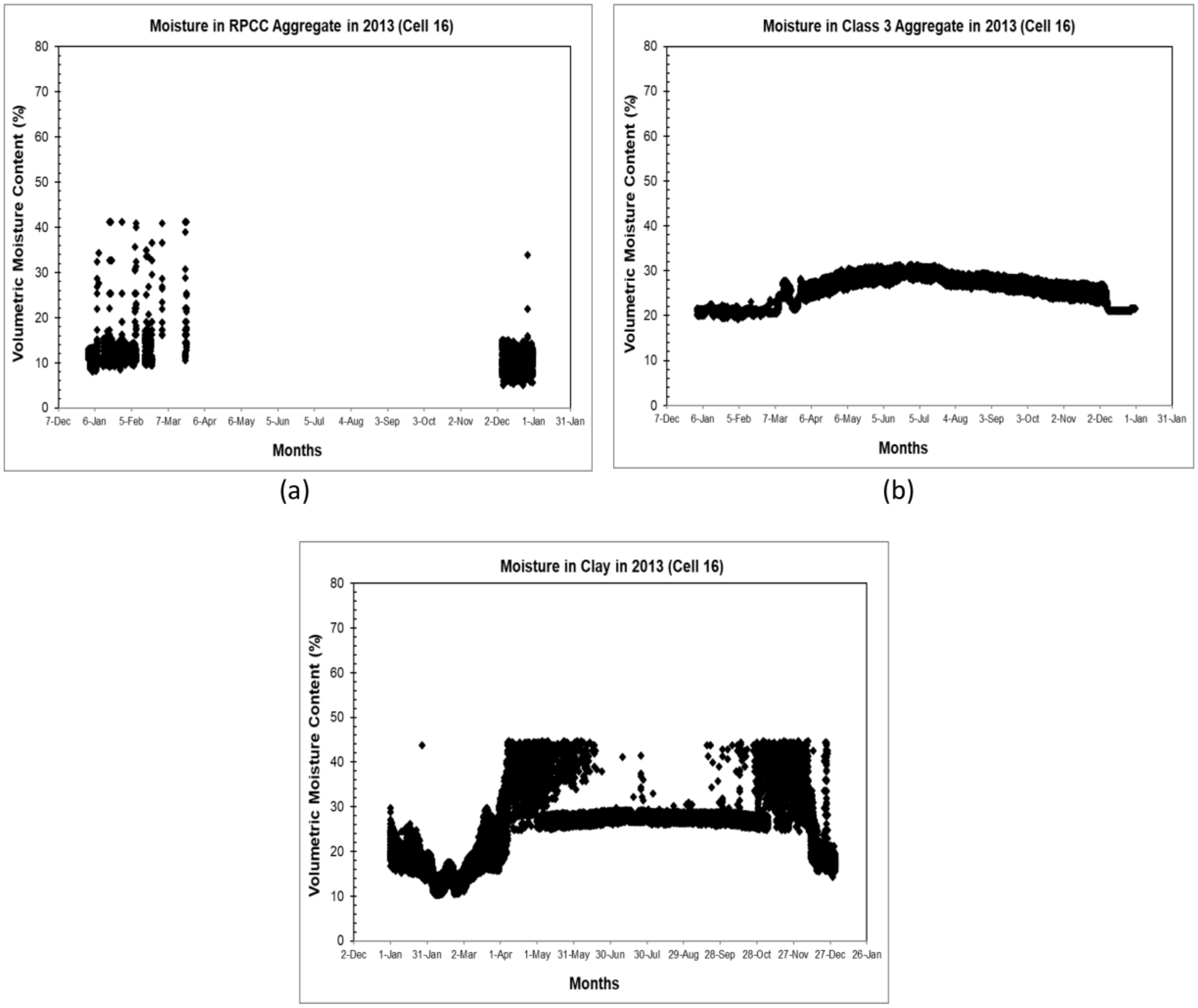

(a)

(b)

(c)

Figure A4. Volumetric moisture content trend of Cell 16 in 2013 for (a) RCA base (b) Class 3 aggregate base and (c) clay subgrade layer

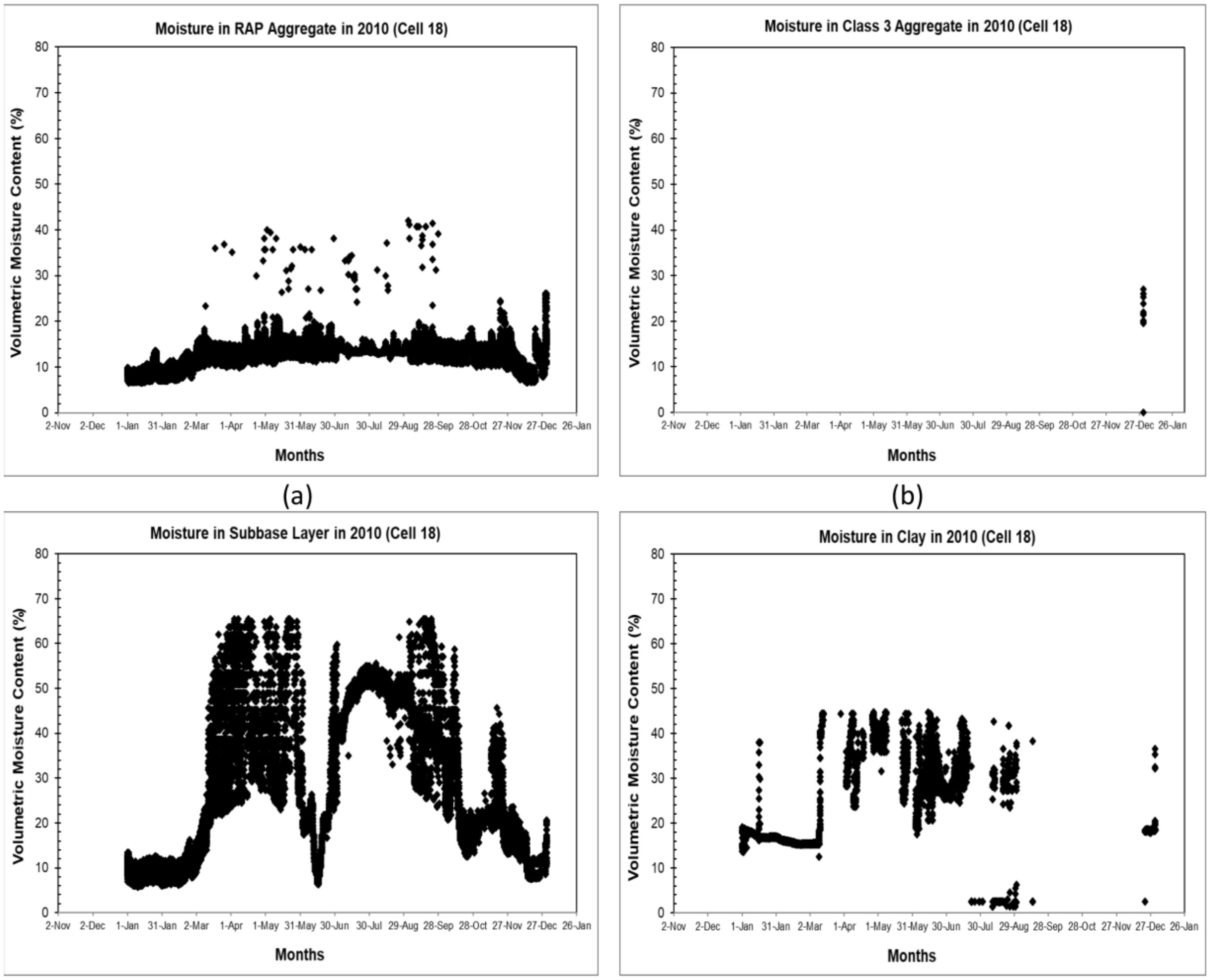

(a) (b)

(c) (d)

Figure A5. Volumetric moisture content trend of Cell 18 in 2010 for (a) RAP base (b) Class 3 aggregate base (c) SG subbase and (d) clay subgrade layer

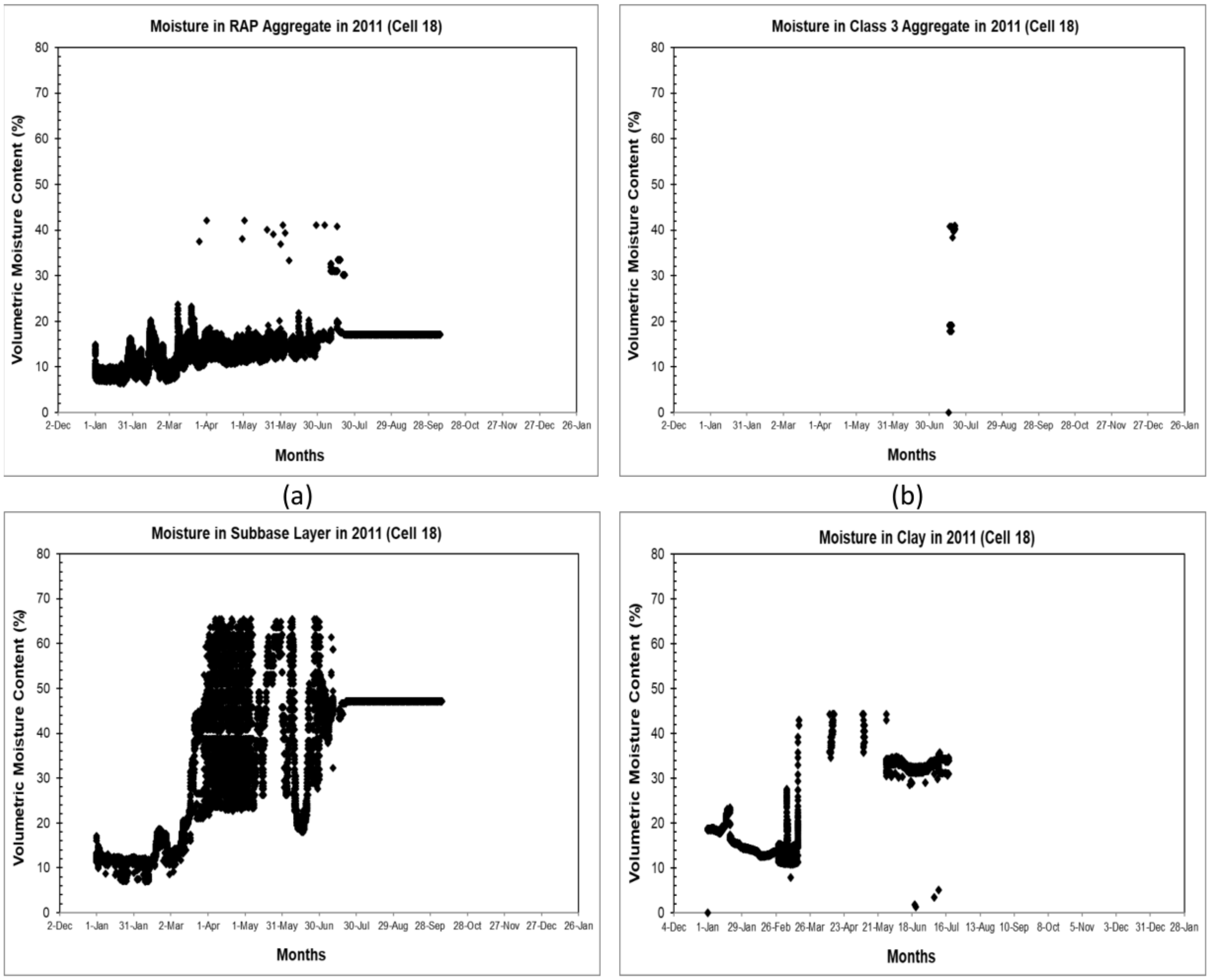

(a) (b)

(c) (d)

Figure A6. Volumetric moisture content trend of Cell 18 in 2011 for (a) RAP base (b) Class 3 aggregate base (c) SG subbase and (d) clay subgrade layer

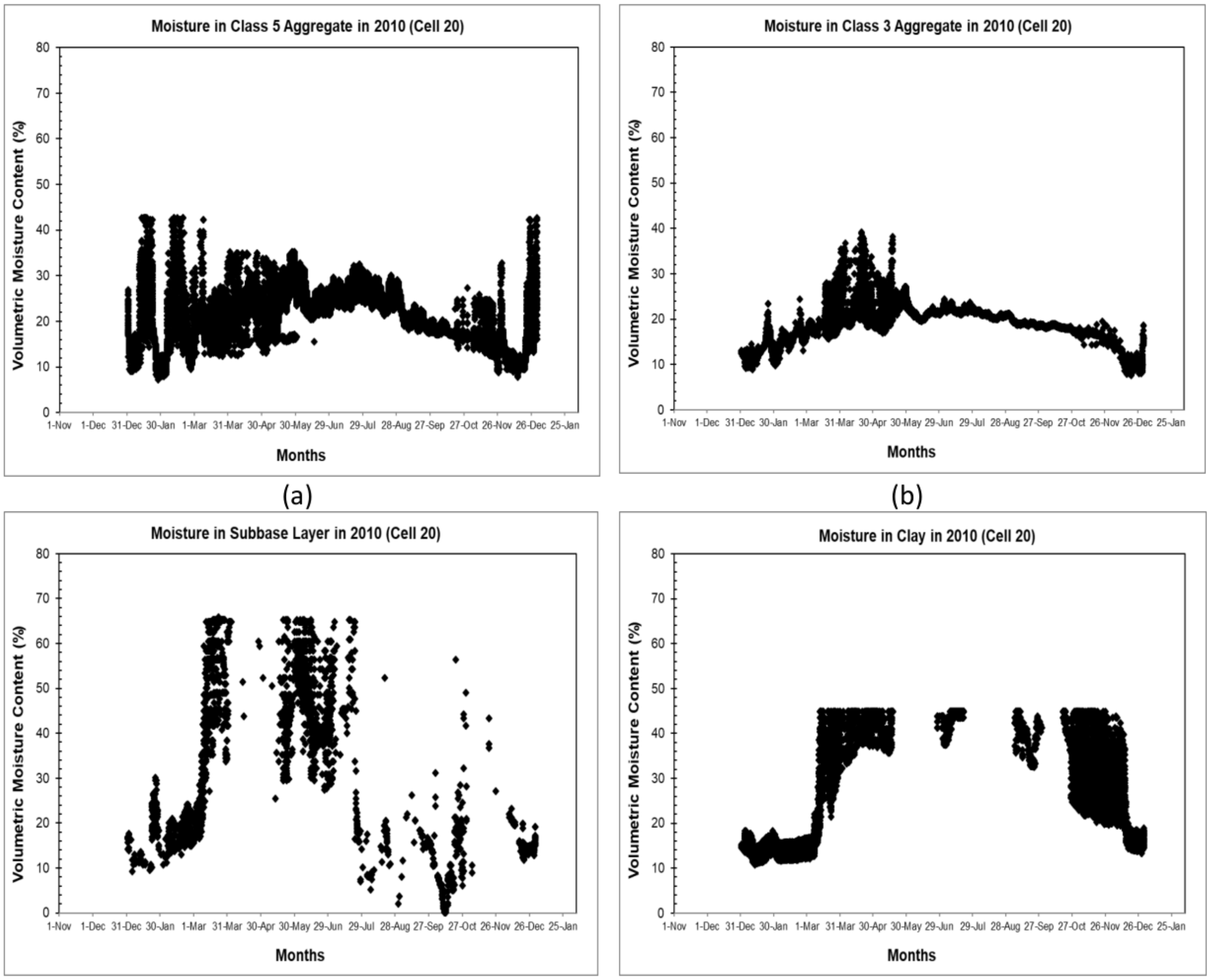

(a) (b)

(c) (d)

Figure A7. Volumetric moisture content trend of Cell 20 in 2010 for (a) Class 5 aggregate base (b) Class 3 aggregate base (c) SG subbase and (d) clay subgrade layer

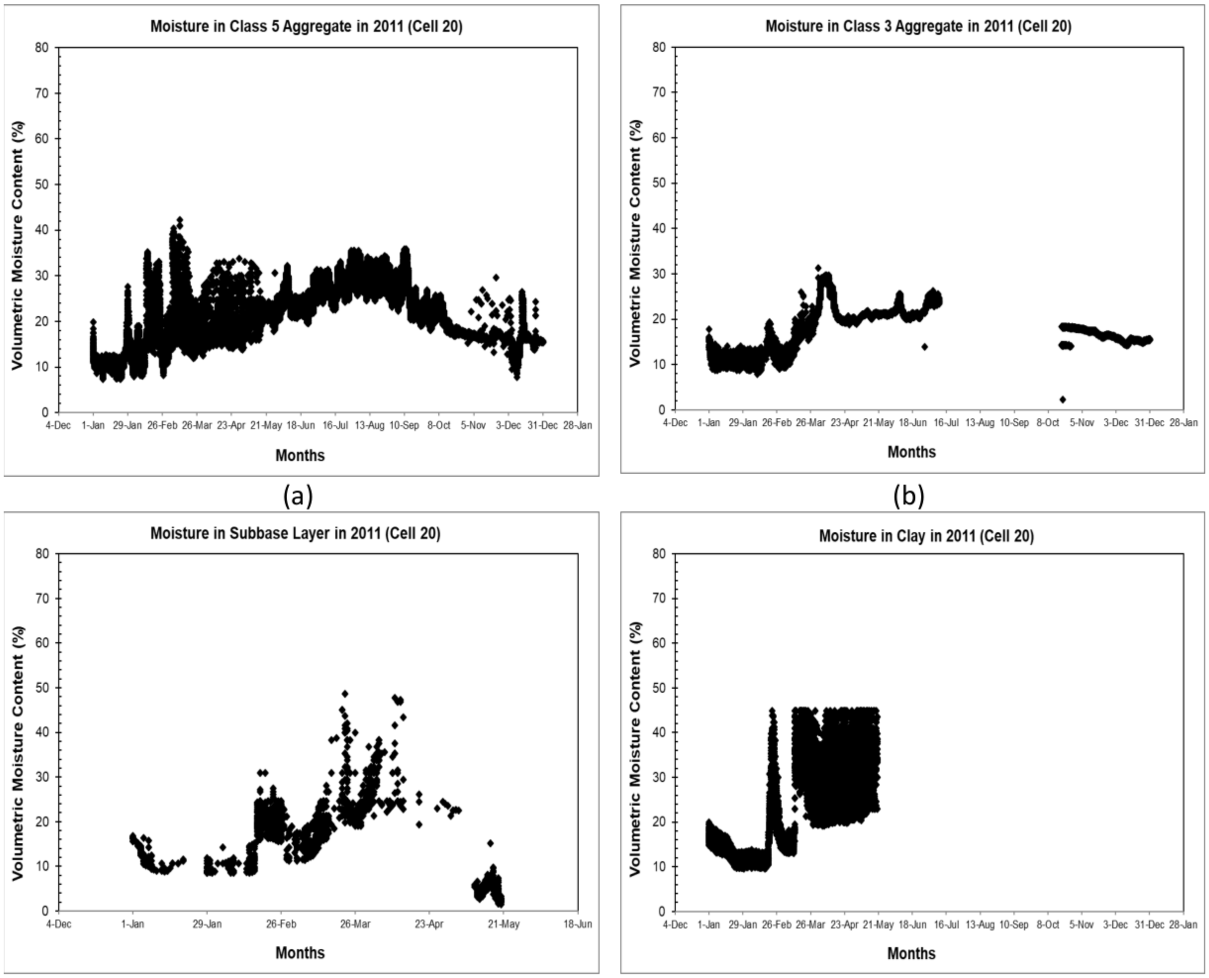

(a) (b)

(c) (d)

Figure A8. Volumetric moisture content trend of Cell 20 in 2011 for (a) Class 5 aggregate base (b) Class 3 aggregate base (c) SG subbase and (d) clay subgrade layer

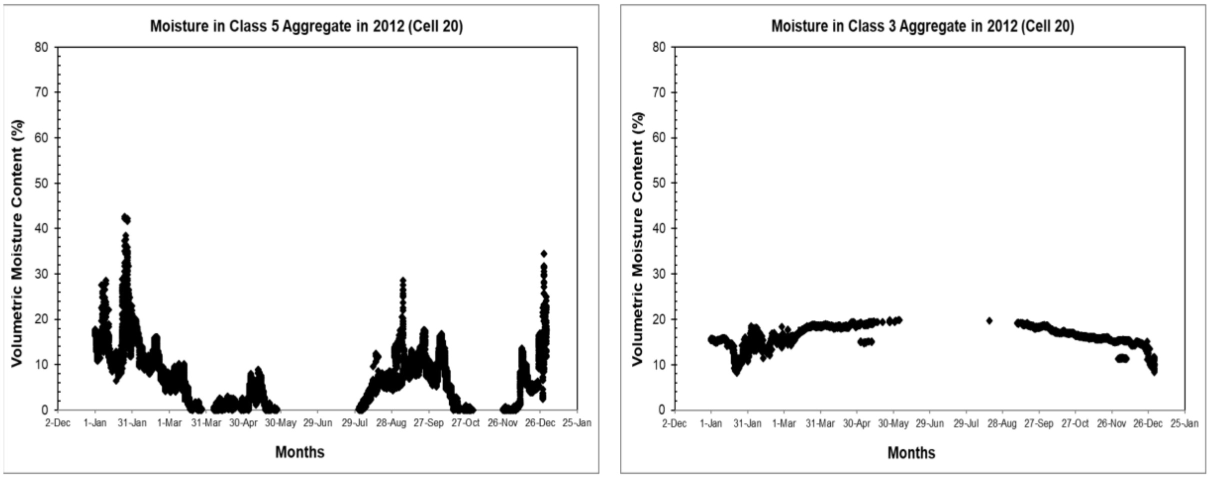

(a) (b)

Figure A9. Volumetric moisture content trend of Cell 20 in 2012 for (a) Class 5 aggregate base and (b) Class 3 aggregate base layer

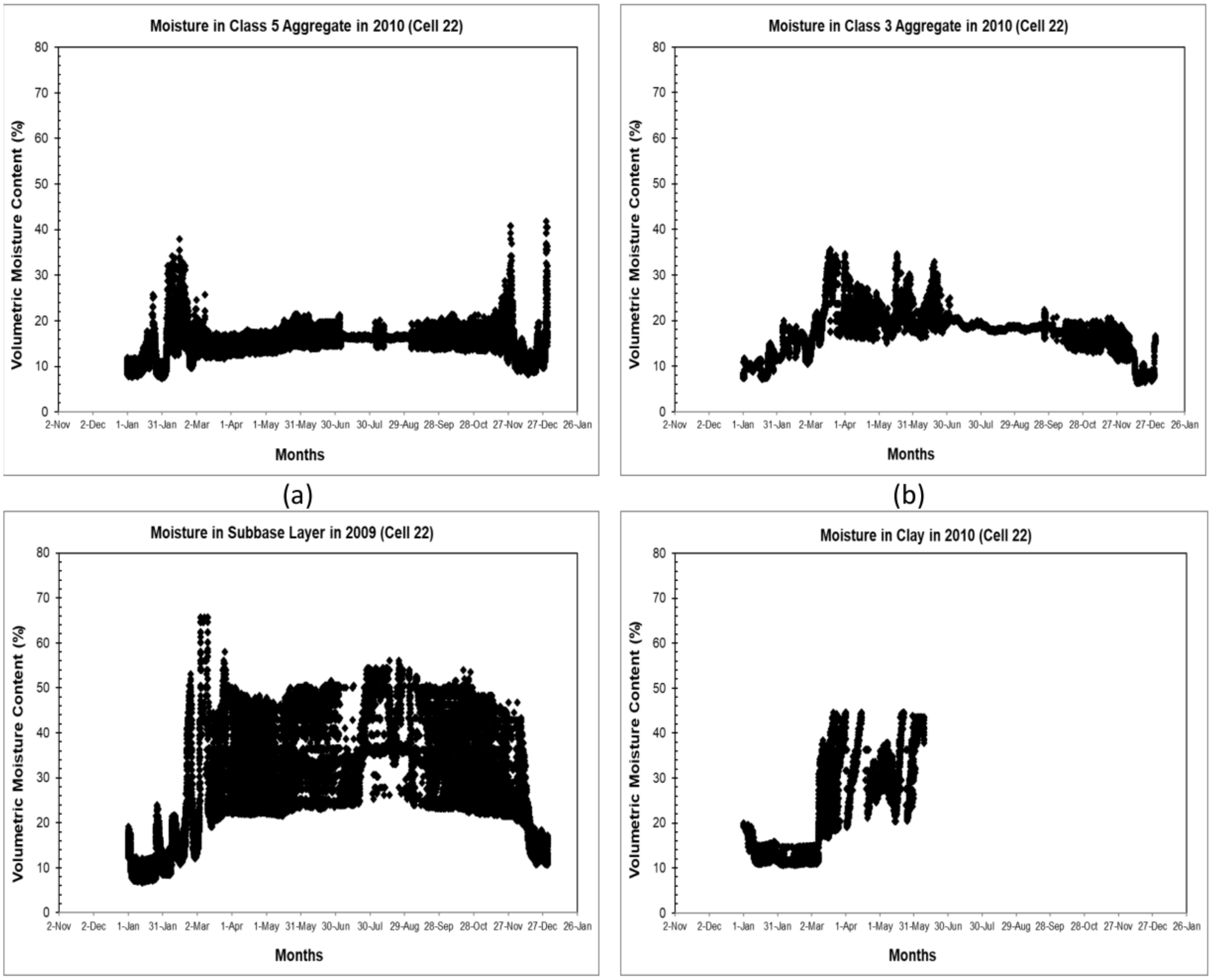

(a)

(b)

(c)

(d)

Figure A10. Volumetric moisture content trend of Cell 22 in 2010 for (a) Class 5 aggregate base (b) Class 3 aggregate base (c) SG subbase and (d) clay subgrade layer

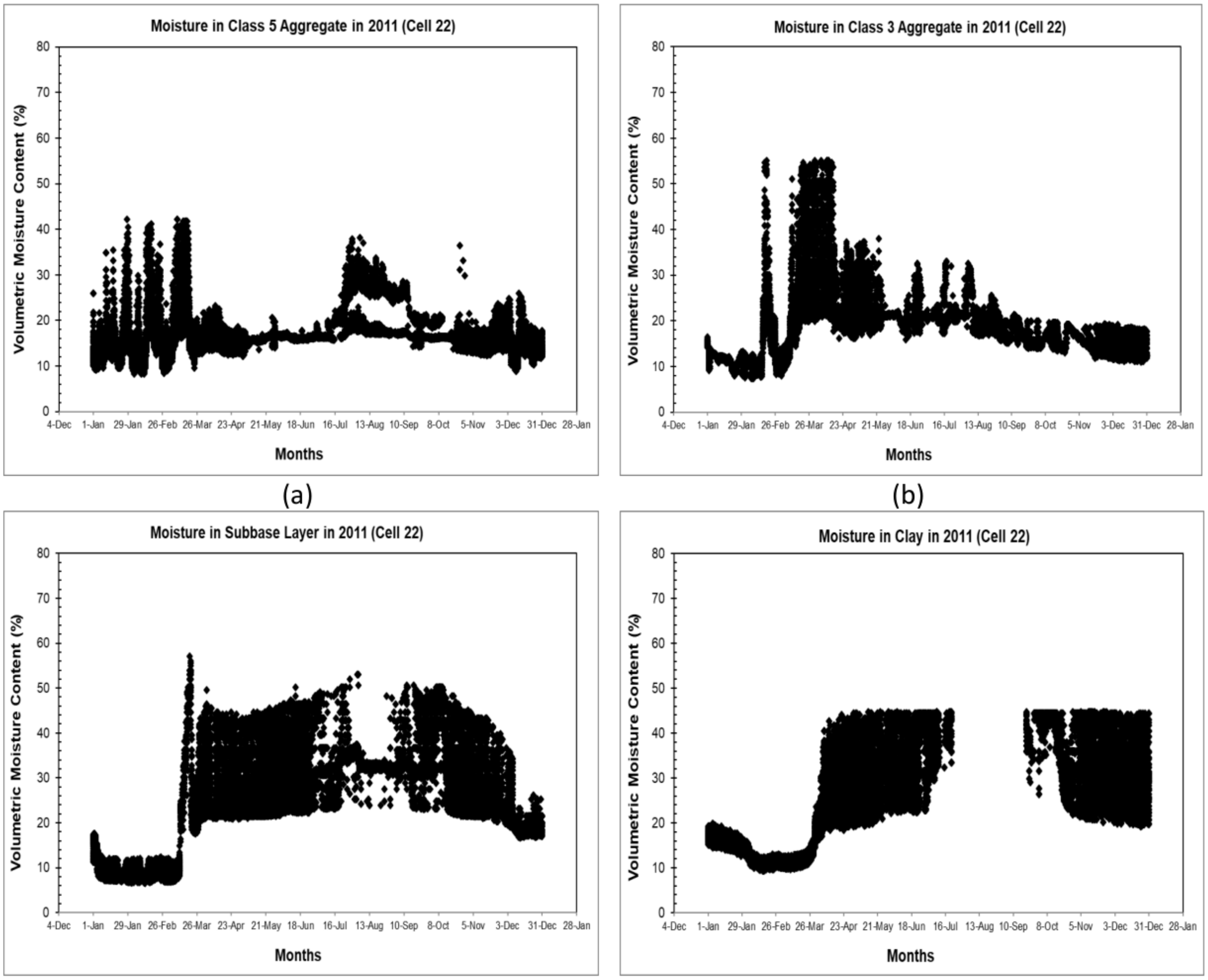

(a) (b)

(c) (d)

Figure A11. Volumetric moisture content trend of Cell 22 in 2011 for (a) Class 5 aggregate base (b) Class 3 aggregate base (c) SG subbase and (d) clay subgrade layer

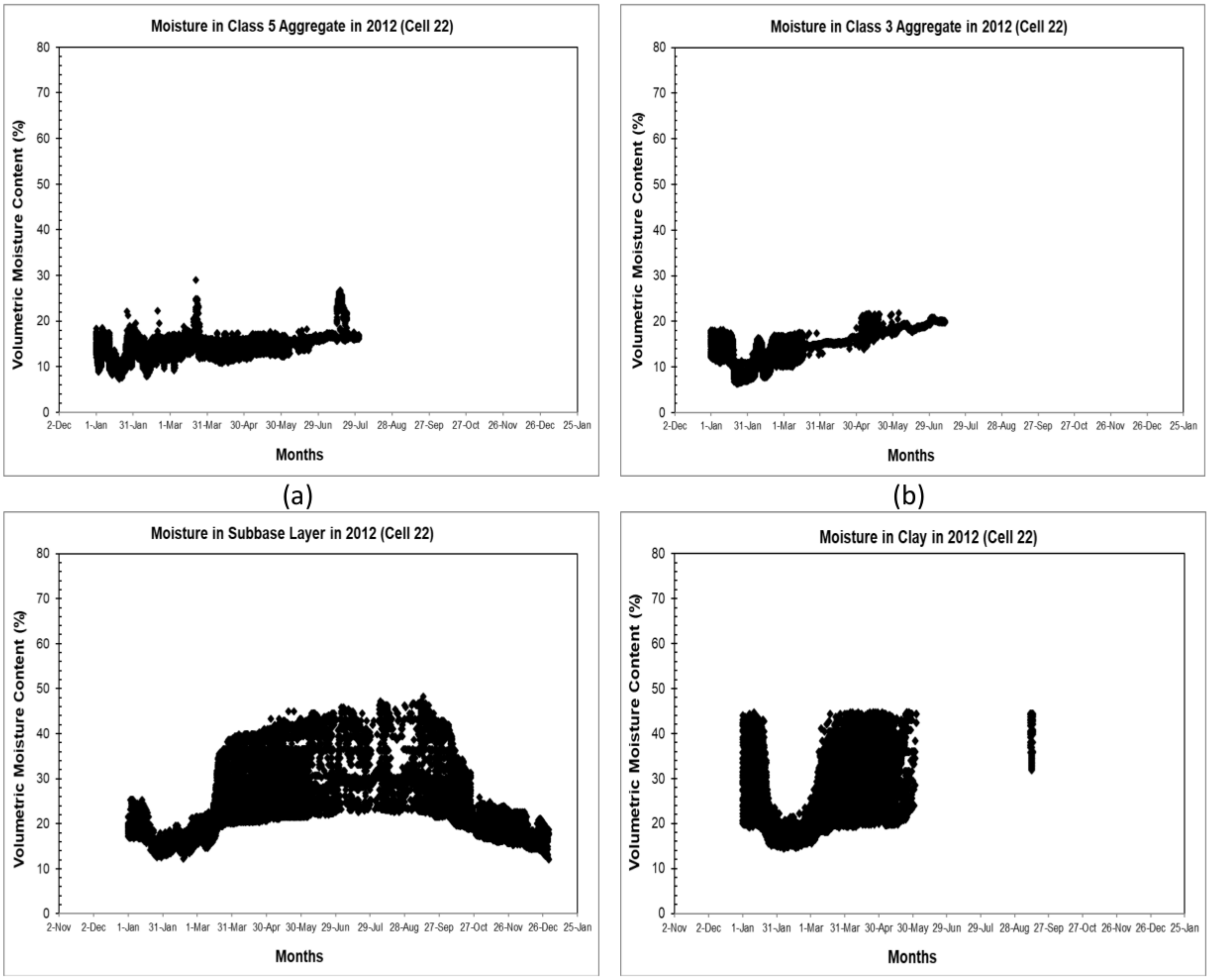

(a) (b)

(c) (d)

Figure A12. Volumetric moisture content trend of Cell 22 in 2012 for (a) Class 5 aggregate base (b) Class 3 aggregate base (c) SG subbase and (d) clay subgrade layer

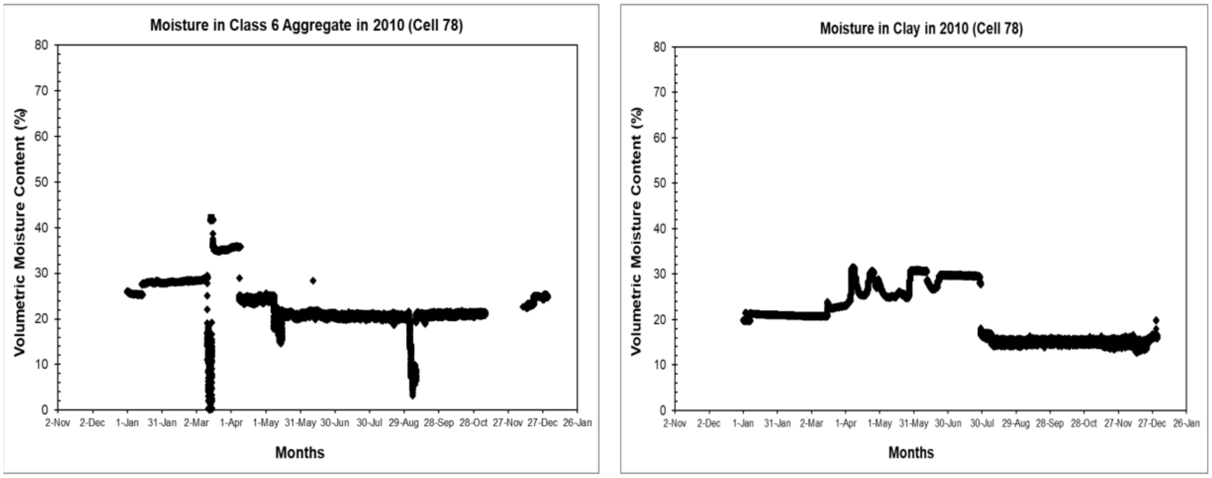

(a) (b)

Figure A13. Volumetric moisture content trend of Cell 78 in 2010 for (a) Class 6 aggregate base and (b) clay subgrade layer

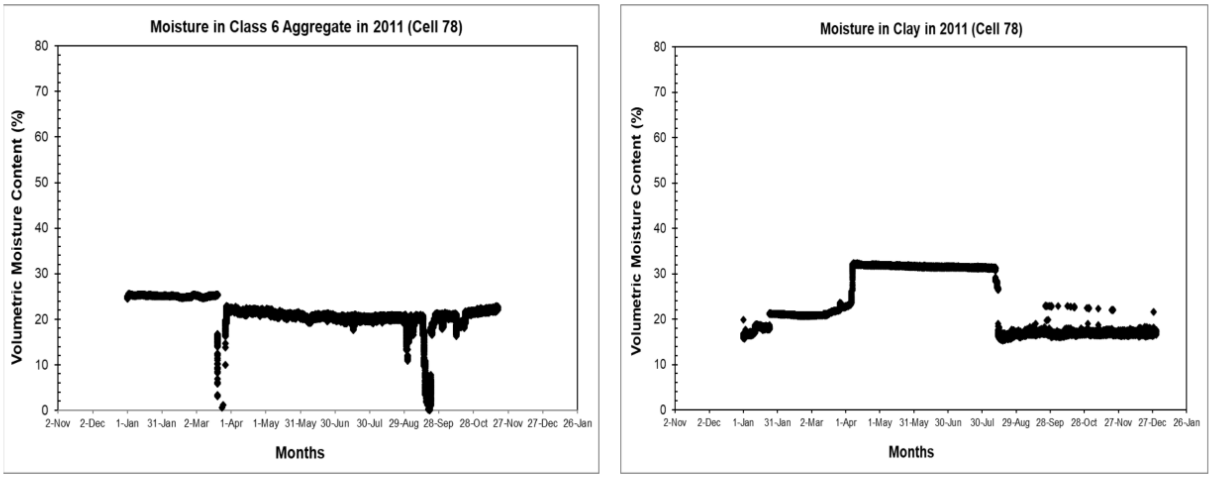

(a) (b)

Figure A14. Volumetric moisture content trend of Cell 78 in 2011 for (a) Class 6 aggregate base and (b) clay subgrade layer

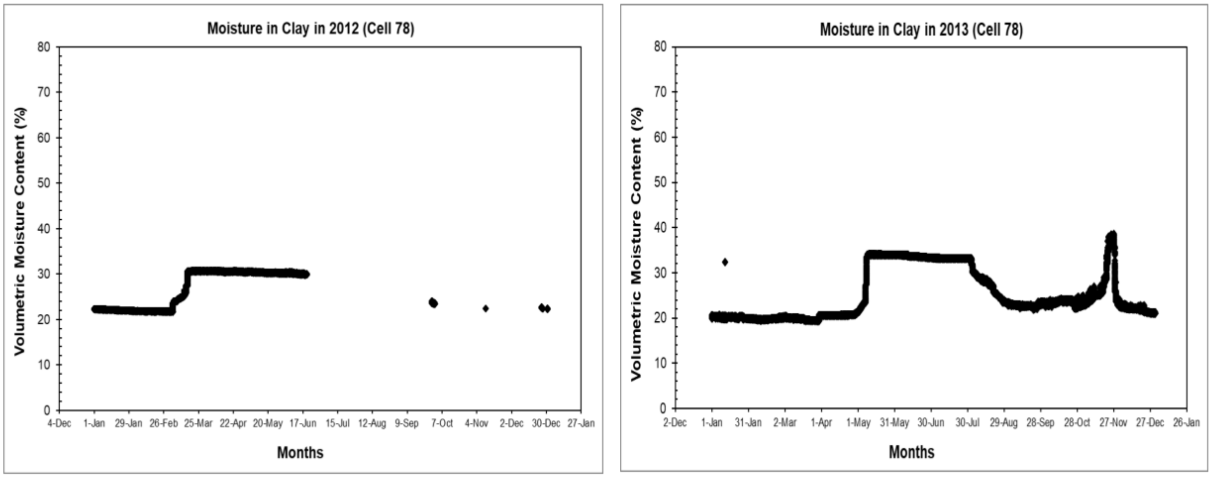

(a) (b)

Figure A15. Volumetric moisture content trend of Cell 78 in clay subgrade layer for (a) year 2012 and (b) year 2013

Appendix B: Python Script

```python
import pandas as pd
import math
import warnings
import shapely
import geopandas
from shapely.geometry import Point
import numpy

warnings.filterwarnings('ignore')

inputs = pd.read_csv("Inputs.csv")
inputs["Rain_Duration"] = numpy.nan
inputs["Rain_Intensity"] = numpy.nan
inputs["Saturation"] = numpy.nan
inputs["MR"] = numpy.nan

weather  = pd.read_excel("Weather_2020_MnROAD.xlsx")
inputs["date"] = pd.to_datetime(inputs["date"])

#fixed value
a = -0.3123
b = 0.3
km = 6.8157


def saturation_cal(cell_no, rain_int, rain_dur, hydrlic_conduc=None):
    if cell_no==188:
        saturation = 22.31+2.70*rain_int+3.31*rain_dur

    elif cell_no==189:
        saturation = 20.65+3.61*rain_int+3.15*rain_dur

    elif cell_no==127:
        saturation = 18.97+3.27*rain_int+2.71*rain_dur

    else:
        if isinstance(hydrlic_conduc, (int, float)):
            saturation = 21.63+3.60*rain_int+2.83*rain_dur-0.34*hydrlic_conduc
        else:
            raise Exception("Provide correct hydraulic conductivity value")
    return saturation/100


# calculation starts

for index, row in inputs.iterrows():
    cell_no = int(row["Cell No/identifier"])
    date = row["date"]
    SOPT = row["SOPT"]
    MROPT = row["MROPT"]
    hydrlic_conduc = row["hydrlic_conduc"]


    #weather information extracts here
    day_weather = weather.loc[weather["DAY"]  == date]

    # print (weather.loc[weather["DAY"] == inputs["date"][0]]) #see day weather
    rain_dur = (day_weather['PRECIP_100TH_INCH'] != 0).sum()/4

    if rain_dur == 0:
```

```
        rain_int = 0 # no rainfall, 0 intensity
    else:
        rain_int = day_weather['PRECIP_100TH_INCH'].sum()/rain_dur


    #saturation and MR calculation
    saturation = saturation_cal(cell_no, rain_int, rain_dur, hydrlic_conduc=hydrlic_conduc)

    right_side= a+(b-a)/(1+math.exp(math.log10(-b/a)+km*(saturation-SOPT)))
    MR = MROPT*math.pow(10, right_side)

    inputs["Saturation"][index] = round(saturation, 5)
    inputs["MR"][index] = round(MR, 2)
    inputs["Rain_Duration"][index] = rain_dur
    inputs["Rain_Intensity"][index] = rain_int

    #print (cell_no,rain_int, rain_dur,  saturation, right_side, round(MR, 2) )
print (inputs)


# shapefile creation
# combine lat and lon column to a shapely Point() object
inputs["date"] = inputs["date"].dt.strftime('%m-%d-%Y')
inputs['geometry'] = inputs.apply(lambda x: Point((float(x.Longitude), float(x.Latitude))), axis=1)
inputs_geo = geopandas.GeoDataFrame(inputs, geometry='geometry')
inputs.to_csv("output.csv")
inputs_geo.crs= "+proj=longlat +ellps=WGS84 +datum=WGS84 +no_defs"
inputs_geo.to_file('MyGeometries.shp', driver='Esri Shapefi
```